Numerical Analysis of Granular Jet Impacts

Tomohiko Sano

January, 22, 2013

Contents

Abstract

Non-equilibrium phenomena induced by impacts have been extensively studied in various contexts, such as nuclear reactions, nanotechnology and granular flows. Recent experimental and numerical studies revealed interesting aspects of impact processes of a granular flow. An experimental paper on dense granular jets [Cheng *et al.*, Phys. Rev. Lett. 99, 188001 (2007)] has reported that the fluid state after the impact is similar to that for Quark Gluon Plasma (QGP) achieved in heavy ion colliders, where QGP behaves as a fluid with very small viscosity. Quite recently, a theoretical group at Chicago demonstrated that the solution of inviscid Euler equation is almost identical to that obtained from their molecular dynamics simulation for inelastic hard core particles, at least, for two dimensional frictionless grains. These results are counter intuitive because in a usual setup the dense granular fluid has a large viscosity.

In this dissertation, we investigate impact processes of granular jets on a fixed wall, in both two (2D) and three dimensions (3D) numerically, by using Discrete Element Method, to study the fluid state after the impacts. We found the following properties of the impact processes of granular jets.

(i) In 3D, the equation of states and the shear viscosity are consistent with the kinetic theory, while the shear stress is much smaller than normal stresses, thanks to the small strain rate.
(ii) In 2D, because grains are well packed, the asymptotic divergence of the pressure or the shear viscosity similar to the jamming transition, appears.
(iii) In 2D, for bidispersed systems, the effective friction constant defined as the ratio between shear stress and normal stress, monotonically increases from near zero, as the increment of the strain rate. On the other hand, the friction constant has two metastable branches for mono-disperse system because of the coexistence of a crystallized state and a liquid state.
(iv) Both in 2D and 3D, there exist large normal stress differences, which cannot be observed in the perfect fluid.

These results (i)-(iv) may be in contrast to the experimental suggestion of the similarity between granular jets and “perfect fluid.” In particular, our numerical result (i) provides a theoretical explanation of the similarity between granular flow and perfect fluid, which has been reported in an experiment and the 2D study. Through the investigation of the rheological properties, we may conclude that the similarity between the granular flow and the perfect fluid, which comes from a small strain rate, is superficial. Our results may shed light on the internal fluid structure under strong non-equilibrium situations, i.e., the impact processes of a granular jet.

Chapter 1

Introduction

1.1 Impact Process

Physics of impact processes is one of hot subjects in non-equilibrium physics. Impact processes play important roles in various fields such as nuclear reactions [1–8], atomic collisions [9, 10], nano cluster collisions [11–16], hydrodynamics [17–30] and granular physics [31–40], including industrial applications [41, 42].

1.1.1 Impact process in the nuclei-scale

Dense and high energy states of nuclei are revealed through heavy ion collisions such as Au-Au collisions [1] and Pb-Pb collisions [2]. One of the primary purposes of heavy ion physics at high energies is to explore the properties of strongly interacting matter i.e. the Quark Gluon Plasma (QGP) [3–5]. QGP behaves as a fluid with very small shear viscosity. Kovtun *et al.* characterize how close a given fluid is to being perfect by using the ratio of shear viscosity to volume density of entropy, which is derived via string theory [6]. The numerical study for the nuclei collisions are performed by using hydrodynamical model [3, 4] and the antisymmetrized molecular dynamics (AMD) method [7, 8]

1.1.2 Impact process in the nano-scale

The dynamics of nano clusters have been extensively investigated from both scientific interest [11–16] and technological interest [41, 42]. For example, impact processes of grains with adhesions [12], polymeric nano droplet [13]. Several states after the impact of Lenard-Jones clusters, such as sticking, scattering and fragmentation can be found via Molecular Dynamics (MD) simulations [11]. Super elastic collisions, where restitution coefficients exceeds unity, are also recent hot topics for the non-equilibrium phenomena induced by impacts [14–16]. Industrial applications would be the blast cleaning, which is the cleaning technique for the surface of metal through impinging jets of nano-particles [41], or the ink-jet printing [42].

1.1.3 Impact process in the macroscopic scale

Impact process of water columns

Impact of water columns has a long history [19–30].The studies on water bells start experimentally in 1833 with the work of Savart [19–22]. Savart investigated impact processes of liquid columns on a small target [19] and a large target [20, 21] and a head-on collision of liquid columns [22]. The liquid sheets induced by the liquid jet impacts split into droplets, through the instability from the surface tension. In the twentieth century, the interest in water bells and liquid sheets has mainly moved from physics to engineering for the purpose of controlling the liquid atomization [23, 24]. The investigation for the industrial application triggered the study for the stability of the bells [25–27] and the influence of the rotation [28]. The water bells formed on the underside of a horizontal plate are investigated experimentally [29] and theoretically [30]. The history and the current status for the water bells are summarized in Ref. [27].

Impact process of the granular flow

Recent experimental and numerical studies revealed interesting aspects of impact processes of a granular flow [31–40]. At low volume fractions, impact of a granular flow onto a wall produces a shock, which quantitatively agrees with the Mach cone produced by supersonic gas flow [32–34]. Crater morphology is studied via an impact process of a free-falling water drop or grain onto a granular layer [35, 36], while a sinking grain produces a sand jet [37].

Recently, an experimental paper on dense granular jets [31] has reported that the fluid state after the impact is similar to that for QGP achieved in heavy ion colliders, where QGP behaves as a fluid with very small viscosity [1, 6]. Quite recently, Ellowitz *et al.* [38] demonstrated that the solution of inviscid Euler equation is almost identical to that obtained from their MD simulation for inelastic hard core particles, at least, for two-dimensional (2D) frictionless grains. These results are counter intuitive because in a usual setup the dense granular fluid has a large viscosity [43]. Huang *et al.* reported that the relevant role of the contact stress in a 2D granular jet [40] and Guttenberg constructed the phenomenology for the scattering angle [39], while the rheology during the impact process is not clear.

1.2 The Aim of This Paper

The aim of this dissertation is to investigate non-equilibrium phenomena induced by jet impacts. The length scale of jet-induced phenomena ranges from the scale of grains $mm \sim \mu m$ to that of nuclei, where various interactions can be found, such as excluded volume effects (contact forces), long-range repulsive or attractive interactions and dissipation. To extract the simple physics induced by impacts, we adopt contact forces with dissipation as an interaction

model, which corresponds to that of interaction between dry grains, i.e. Discrete Element Method (DEM) [45, 46].

One of the noteworthy facts would be the jet-induced perfect-fluidity, suggested via experiments. We perform three-dimensional (3D) simulation for granular jet impacts for both frictional and frictionless grains [47, 48]. Small shear stress observed in the experiment [31] is reproduced through our simulation. However, the fluid state after the impact is far from a perfect fluid, and thus, similarity between granular jets and quark gluon plasma is superficial, because the observed viscosity is finite and its value is consistent with the prediction of the kinetic theory.

We perform 2D simulations for the granular jet [49]. Because grains are easily packed through the impact in 2D, the system would be near the jammed state. This 2D study is complementary to the previous 2D DEM study [40], and hard core simulations supplemented by the simulation of a perfect fluid model [38]. Indeed, although Huang *et al.* reported that the relevant role of the contact stress in a 2D granular jet, they were not interested in critical behavior of jammed grains induced by the jet. Guttenberg suggested that the friction constant does not play significant role, at least, in the scattering angle [39] by using an approximate hard-sphere method [44], while the effects on the jammed state induced by jets are unknown.

This paper is organized as follows: After a short review of the kinetic theory for granular flow and studies of the dense granular flow in Chapter 2, we introduce the outline of DEM briefly in Chapter 3. We focus on the scattered states of the granular jets in 3D in Chapter 4. Rheology of the granular jets in 3D and 2D are discussed in Chapter 5 and 6, respectively. We summarize the results and future works in Chapter 7. We show the detailed derivations of hydrodynamical equations in Appendix A and the detailed implementation of DEM in Appendix B. In Appendix C, we derive the local description of stress tensor. We analyze the shear viscosity on a shear stress vs strain rate plane in 3D in Appendix D, and results for artificial burst-like flows in 2D are summarized in Appendix E.

Chapter 2

Many-body System of Granular Matter

In this chapter we briefly review investigations of the granular hydrodynamics and the rheology of dense granular flows to apply them to granular jet impacts. Firstly we review the history of kinetic theory such as Boltzmann equation, Enskog equation, Chapman-Enskog expansion, BBGKY hierarchy, Choh-Uhlenbeck equation and Revised Enskog equation. Next, we explain the kinetic theory for granular flows. The treatment of rotational degree of freedom of grains is also discussed. Lastly, we review the rheology of dense granular flows, including Bagnold scaling, granular friction and the scaling theory of jamming transitions, where the kinetic theory breaks down. If you are familiar with these subjects, you can skip reading this chapter.

2.1 Granular Hydrodynamics

To understand many-body systems of grains, hydrodynamical pictures are necessary, where density n, velocity field $\bar{\mathbf{v}}$ and granular temperature T_g, which denotes the fluctuation of the particle-velocities, are conventionally chosen as hydrodynamical variables. The kinetic theory was applied to a granular flow for the first time by Jenkins and Savage [50]. Hydrodynamics for granular flow, where transport coefficients are calculated explicitly through the kinetic theory, is called granular hydrodynamics [50–76]. There are many studies for granular hydrodynamics including smooth grains [50–53], micro-polar fluid model [54,55], rough grains [56–62], slightly frictional grains [63–68] or grains with dispersity [69–71], which are valid up to moderate dense flow.

2.1.1 Review for the Kinetic Theory:

From Boltzmann equation to Revised Enskog equation

Here, we review the history of the kinetic theory. The kinetic theory is the theory which originates from Boltzmann. There are many textbooks for the kinetic theory [77–84]. The history of the kinetic theory is also summarized and the original paper for Chapman-Enskog methods or Enskog theory is re-printed in Ref. [84].

Boltzmann equation

Boltzmann equation, which is a time evolution equation for the one-body distribution function, is introduced to understand the second law of thermodynamics from mechanical viewpoint in 1872. The velocity before the collision $\mathbf{v}_l$ and after the collision $\mathbf{v}_l'$ of l th grains ($l = 1, 2$) with restitution coefficient e and the same mass are related as

$$\mathbf{v}_1' = \mathbf{v}_1 - \frac{1+e}{2}(\mathbf{k}\cdot\mathbf{v}_{12})\mathbf{k} \tag{2.1}$$

$$\mathbf{v}_2' = \mathbf{v}_2 + \frac{1+e}{2}(\mathbf{k}\cdot\mathbf{v}_{12})\mathbf{k}, \tag{2.2}$$

with the unit vector $\mathbf{k} \equiv (\mathbf{r}_2 - \mathbf{r}_1)/|\mathbf{r}_2 - \mathbf{r}_1|$ and relative velocities $\mathbf{v}_{12} \equiv \mathbf{v}_1 - \mathbf{v}_2$. We introduce the pre-collision velocities $\mathbf{v}_l''$, which lead $\mathbf{v}_l$ after the collision:

$$\mathbf{v}_1'' = \mathbf{v}_1 - \frac{1+e}{2e}(\mathbf{k}\cdot\mathbf{v}_{12})\mathbf{k} \tag{2.3}$$

$$\mathbf{v}_2'' = \mathbf{v}_2 + \frac{1+e}{2e}(\mathbf{k}\cdot\mathbf{v}_{12})\mathbf{k}. \tag{2.4}$$

Equations. (2.1) and (2.2) are called direct collisions and Eqs. (2.3) and (2.4) are called inverse collisions. Boltzmann equation for elastic gas, which corresponds to the case $e = 1$, without external force is described as

$$\frac{\partial f_1}{\partial t} + \mathbf{v}_1 \cdot \nabla_1 f_1 = \int d^3v_2 d^2k S(\mathbf{k}\cdot\mathbf{v}_{12})(f_1'' f_2'' - f_1 f_2), \tag{2.5}$$

with the scattering cross section $S(\mathbf{k}\cdot\mathbf{v}_{12}) \equiv \sigma^2|\mathbf{k}\cdot\mathbf{v}_{12}|\Theta(\mathbf{k}\cdot\mathbf{v}_{12})$, where we have introduced Heaviside function $\Theta(x)$ with $\Theta(x) = 1(x \geq 0)$ and $\Theta(x) = 0(x < 0)$ and particle diameter σ, with abbreviation $f_i \equiv f(\mathbf{r}_i, \mathbf{v}_i)(i = 1, 2)$ and $f_i'' \equiv f(\mathbf{r}_i, \mathbf{v}_i'')$ at the position of i th particle $\mathbf{r}_i$. The right hand side on Eq. (2.5) is called the collision integral

$$I_{\rm el}(f, f) \equiv \int d^3v_2 d^2k S(\mathbf{k}\cdot\mathbf{v}_{12})(f_1'' f_2'' - f_1 f_2). \tag{2.6}$$

The first term of the collision integral denotes the increase of the probability f_1 after the collision and the second term denotes the decrease of f_1. Boltzmann equation has been used not only for classical gases but for electron gases

or plasma [85, 86] and verified via Direct Simulation of Monte Carlo (DSMC) method [87–90].

Hydrodynamical equations, which will be discussed later, can be derived from Boltzmann equation by integrating over $\int d^3v_1$ after multiplying $\psi_1 \equiv 1, v_{1\alpha}, \mathbf{v}_1^2$, which are zero eigenvector of the collision integral:

$$\begin{aligned}
\int d^3v_1\psi_1 I_{\rm el}(f,f) &= \int d^3v_1 d^3v_2\psi_1 \int d^2kS(g_{12})(f_1''f_2'' - f_1f_2) \quad (2.7)\\
&= \frac{1}{4}\int d^3v_1 d^3v_2\{\psi_1+\psi_2-\psi_1'-\psi_2')\} \quad (2.8)\\
&\quad \times \int d^2kS(g_{12})(f_1''f_2'' - f_1f_2)\\
&= 0, \quad (2.9)
\end{aligned}$$

with $g_{12} \equiv \mathbf{k}\cdot\mathbf{v}_{12}$. The time reversal symmetry during local collisions is used to derive the second equation, and the last equation results from the conservation of mass, momentum and kinetic energy. Because the derived hydrodynamical equations contain unknown function, such as the stress tensor or the heat flux, we need the explicit expressions for f_1. The systematic perturbative method to obtain f_1 is known as Chapman-Enskog expansion.

Chapman-Enskog expansion

The explicit calculation of the shear viscosity and the heat conductivity is performed in 1917 by Chapman and Enskog, where Boltzmann equation (2.5) is perturbatively solved by assuming that the distribution function f_1 depends on space ant time variables through hydrodynamic variables $\boldsymbol{a}(\mathbf{r},t) = \{n(\mathbf{r},t), \bar{\mathbf{v}}(\mathbf{r},t), T(\mathbf{r},t)\}$ [91], i.e. the local density $n(\mathbf{r},t)$, the local velocity field $\bar{\mathbf{v}}(\mathbf{r},t)$ and the local temperature $T(\mathbf{r},t)$: $f_1(\mathbf{v}_1,\mathbf{r},t) \to f_1(\mathbf{v}_1|n,\bar{\mathbf{v}},T)$. Namely, $\partial_t f_1 \to (\partial f_1/\partial \boldsymbol{a})\partial_t \boldsymbol{a}$. Because there is a large scale separation between kinetic and hydrodynamical regime, the small expansion parameter $\epsilon \sim l_0\partial_\alpha$, which denotes the non-uniformity parameter, is introduced as a systematic expansion parameter with a mean free path l_0. The distribution function is expanded as $f_1 = f_M + \epsilon f^{(1)} + O(\epsilon^2)$, with local Maxwellian f_M and $\int d^3v_1 f_M = n$. Here, $O(\epsilon^0)$ and $O(\epsilon^1)$ denote Euler and Navier-Stokes order solutions, respectively. In summary, Chapman-Enskog method is the method to solve following equations:

$$\begin{aligned}
\frac{\partial f}{\partial t} + \epsilon\mathbf{v}_1\cdot\nabla_1 f &= I_{\rm el}(f,f), \quad (2.10)\\
f &= f_M + \epsilon f^{(1)} + O(\epsilon^2), \quad (2.11)\\
f(\mathbf{v}_1,\mathbf{r},t) &= f(\mathbf{v}_1|n(\mathbf{r},t),\bar{\mathbf{v}}(\mathbf{r},t),T(\mathbf{r},t)). \quad (2.12)
\end{aligned}$$

BBGKY hierarchy

Let us show the relation betweenn Boltzmann equation Eq. (2.5) and the microscopic equations of motion (EoM) for N particles, following Ref. [83]. The

dynamics of the system can be described as the trajectory of a phase point in the $6N$ dimensional phase spase $(\mathbf{r}^N, \mathbf{p}^N)$ with momenta $\mathbf{p}^N = \mathbf{p}_1, \cdots \mathbf{p}_N$ and $\mathbf{r}^N = \mathbf{r}_1, \cdots, \mathbf{r}_N$. Let H be the Hamiltonian of the system, which we write in general form as

$$H(\mathbf{r}^N, \mathbf{p}^N) = K_N(\mathbf{p}^N) + V_N(\mathbf{r}^N), \tag{2.13}$$

with the total kinetic energy $K_N \equiv \sum_i \mathbf{p}_i^2/2m$ and potential energy $V_N(\mathbf{r}^N)$, where equations of motion are

$$\dot{\mathbf{r}}_i = \frac{\partial H}{\partial \mathbf{p}_i}, \quad \dot{\mathbf{p}}_i = -\frac{\partial H}{\partial \mathbf{r}_i} \tag{2.14}$$

$(i = 1, \cdots N)$. We introduce a phase-space probability density $f^{[N]}(\mathbf{r}^N, \mathbf{p}^N, t)$.

$$\int dr^N dp^N f^{[N]}(\mathbf{r}^N, \mathbf{p}^N, t) = 1. \tag{2.15}$$

The time evolution of the probability density in phase space is governed by the Liouville equation, which is a $6N$ dimensional analogue of the equation of continuity of an incompressible fluid:

$$\frac{df^{[N]}}{dt} = \frac{\partial f^{[N]}}{\partial t} + \sum_i \left(\frac{\partial}{\partial \mathbf{r}_i} \cdot f^{[N]} \dot{\mathbf{r}}_i + \frac{\partial}{\partial \mathbf{p}_i} \cdot f^{[N]} \dot{\mathbf{p}}_i \right) = 0. \tag{2.16}$$

We rewrite Eq. (2.16) for convenience by introducing the pair force f_{ij} between i th and j th particles:

$$\left(\frac{\partial}{\partial t} + \sum_i \cdot \frac{\mathbf{p}_i}{m} \cdot \frac{\partial}{\partial \mathbf{r}_i} \right) f^{[N]} = -\sum_{ij} \mathbf{f}_{ij} \cdot \frac{\partial f^{[N]}}{\partial \mathbf{p}_i}, \tag{2.17}$$

with $f_{ii} = 0$. Because we are usually interested in the behavior of a subset of s particles, we introduce a reduced phase-space distribution function $f^{(s)}$:

$$f^{(s)}(\mathbf{r}^s, \mathbf{p}^s, t) \equiv \frac{N!}{(N-s)!} \int dr^{(N-s)} dp^{(N-s)} f^{[N]}(\mathbf{r}^N, \mathbf{p}^N, t), \tag{2.18}$$

with $\mathbf{r}^s \equiv \mathbf{r}_1, \cdots \mathbf{r}_s$, $\mathbf{p}^s \equiv \mathbf{p}_1, \cdots \mathbf{p}_s$, $\mathbf{r}^{(N-s)} \equiv \mathbf{r}_{s+1}, \cdots \mathbf{r}_N$ and $\mathbf{p}^{(N-s)} \equiv \mathbf{p}_{s+1}, \cdots \mathbf{p}_N$. The time evolution for $f^{(s)}$ can be calculated by integrating Eq. (2.17) over $dr^{(N-s)} dp^{(N-s)}$.

$$\begin{aligned} \left(\frac{\partial}{\partial t} + \sum_i^s \cdot \frac{\mathbf{p}_i}{m} \cdot \frac{\partial}{\partial \mathbf{r}_i} \right) f^{(s)} &= -\sum_{i,j=1}^s \mathbf{f}_{ij} \cdot \frac{\partial f^{(s)}}{\partial \mathbf{p}_i} - \frac{N!}{(N-s)!} \\ &\quad \times \sum_{i=1}^s \sum_{j=s+1}^N \int dr^{(N-s)} dp^{(N-s)} \mathbf{f}_{ij} \cdot \frac{\partial f^{[N]}}{\partial \mathbf{p}_i}. \end{aligned} \tag{2.19}$$

Because $f^{[N]}$ is symmetric with respect to interchange of particle labels and the sum of terms for $j = s+1$ to N in Eq. (2.19) is replaced by $N - s$ times the value of any one term. Thus, Eq. (2.19) can be simplified as

$$\left(\frac{\partial}{\partial t} + \sum_i^s \frac{\mathbf{p}_i}{m} \cdot \frac{\partial}{\partial \mathbf{r}_i} + \sum_{i,j=1}^s \mathbf{f}_{ij} \cdot \frac{\partial}{\partial \mathbf{p}_i} \right) f^{(s)} = - \sum_{i=1}^s \int d\mathbf{r}_{s+1} d\mathbf{p}_{s+1} \mathbf{f}_{i,s+1} \cdot \frac{\partial f^{(s+1)}}{\partial \mathbf{p}_i}. \tag{2.20}$$

The exact equation (2.20), which relates $f^{(s)}$ and $f^{(s+1)}$, is known as the BBGKY (Bogoliubov-Born-Green-Kirkwood-Yvon) hierarchy. The important case is $s = 1$:

$$\left(\frac{\partial}{\partial t} + \frac{\mathbf{p}_1}{m} \cdot \frac{\partial}{\partial \mathbf{r}_1} \right) f \quad = \quad - \int d\mathbf{r}_2 d\mathbf{p}_2 \mathbf{f}_{1,2} \cdot \frac{\partial f^{(2)}}{\partial \mathbf{p}_1} \equiv \left(\frac{\partial f}{\partial t} \right)_{\text{coll}}, \tag{2.21}$$

where we rewrite $f^{(1)} \to f$. Although Eq. (2.21) is exact, we need all $f^{(n)} (n > 1)$ to obtain $f^{(1)}$. Thus, some approximate closure relation is necessary. If we choose

$$\left(\frac{\partial f}{\partial t} \right)_{\text{coll}} = I_{\text{el}}(f, f), \tag{2.22}$$

Boltzmann equation (2.5) is reproduced. Therefore, the assumption of Boltzmann equation is that the two-body distribution function can be approximated as the product of the one-body distribution function. Although the transport coefficients for rarefied can be calculated via Boltzmann equation using Chapman-Enskog expansion, Boltzmann equation is only suitable for dilute gases. Thus, Boltzmann equation has been extended to treat moderate dense gases.

Extension of Boltzmann equation

Indeed, there is a long history to extend Boltzmann equation for the dense fluid [92–102]. In 1922 [92], Enskog proposed one of the generalization of the Boltzmann equation for hard sphere fluid, which is now called "Standard Enskog Theory (SET)," where $f^{(2)}$ is replaced as

$$f^{(2)} \to g(|\mathbf{r}_{12}| = \sigma) f(\mathbf{r}_1, \mathbf{v}_1, t) f(\mathbf{r}_1 - \mathbf{k}\sigma, \mathbf{v}_2, t), \tag{2.23}$$

i.e. the product of the distribution function for the two colliding spheres and $g(\sigma)$ denotes static two-body correlations or the radial distribution function for a hard sphere fluids. This replacement represents the collisional transfer, i.e. instantaneous transfer of momentum and energy over the hard sphere through binary collisions. For the SET, the static correlation g is the function of the number density as in fluid in uniform equilibrium with n evaluated at the contact point $(\mathbf{r}_1 + \mathbf{r}_2)/2$. SET, which is a phenomenology, has been criticized for the absence of the Onsager reciprocity relations in the case of binary mixture of hard-sphere fluids [99].

After the formulation of the BBGKY hierarchy, in 1958, Choh and Uhlenbeck [93] extended the Boltzmann equations to include triple collision term $K(f,f,f)$

$$\frac{\partial f_1}{\partial t} + \mathbf{v}_1 \cdot \nabla f_1 = I_{\rm el}(f,f) + K(f,f,f) + \cdots, \tag{2.24}$$

and performed the density expansion, where the density dependence of the transport coefficients are calculated with the density of the system N/V as an expansion parameter. Here, the correction in Eq. (2.23) is included in $I_{\rm el}(f,f)$. Choh and Uhlenbeck calculated the first order correction of the transport coefficient in three dimensions and Green and Cohen derived the formal structure of l-tuple collision terms ($l = 2, 3, 4, \cdots$). McLennan showed that the first correction term corresponds to the results from Green-Kubo formula [94]. However, Dorfman and Cohen , Weinstock, as well as Goldman and Frieman show that the density expansion contains the logarithmic divergent in the second order correction term in 3D and the first order correction in 2D. Therefore, the convergence of the density expansion might be questionable. Kawasaki and Oppenheim were the first to re-sum the divergent term i.e. ring diagrams [95]. The details of the work by Choh Uhlenbeck are summarized by Ernst [102].

Revised Enskog Theory

Recent accepted phenomenological theory for the kinetic theory is called "Revised Enskog Theory(RET), " which is constructed in 1972 by van Beijeren and Ernst. [96–98, 100]. RET equation is described as

$$(\frac{\partial}{\partial t} + \mathbf{v}_1 \cdot \nabla_1) f(\mathbf{r}_1, \mathbf{v}_1, t) = J_E^{\rm el}[\mathbf{r}_1, \mathbf{v}_1 | f(t)] \tag{2.25}$$

, with collision operator

$$\begin{aligned} J_E^{\rm el}[\mathbf{r}_1, \mathbf{v}_1 | f(t)] \quad \equiv \quad & \int d^3\mathbf{v}_2 d^2k S(\mathbf{k}\cdot\mathbf{v}_{12}) \{ f^{(2)}(\mathbf{r}_1, \mathbf{v}_1'', \mathbf{r}_1 + \sigma\mathbf{k}, \mathbf{v}_2''; t) \\ & - f^{(2)}(\mathbf{r}_1, \mathbf{v}_1; \mathbf{r}_1 - \sigma\mathbf{k}, \mathbf{v}_2; t) \}, \end{aligned} \tag{2.26}$$

where the closure for the two body distribution $f^{(2)}$

$$f^{(2)}(\mathbf{r}_1, \mathbf{v}_1; \mathbf{r}_2 \mathbf{v}_2; t) = \chi(\mathbf{r}_1, \mathbf{r}_2 | n(t)) f(\mathbf{r}_1, \mathbf{v}_1, t) f(\mathbf{r}_2, \mathbf{v}_2, t), \tag{2.27}$$

is adopted. The difference of RET from SET is χ, which is the functional of n as in a fluid in non-uniform under the local equilibrium [103]. RET dose not contradict to the Onsager reciprocal relation [98]. Haro and Garzó showed that the difference between SET and RET emerges in the case of a binary mixture of hard-sphere fluid at Navier-Stokes order [99], or a monatomic fluid at the Burnett order [101].

2.1.2 Kinetic Theory for Granular Flow

Boltzmann equation for granular flow

Let us derive Boltzmann equation for granular gases intuitively, following Ref. [73]. Boltzmann equation consists of the collision integral $I(f,f)$, which denotes

the increase or decrease of $f_1 d^3 r_1$ after the collision per unit time. The number of direct collisions ν^- and that of inverse collisions ν^+ that occur during Δt and whose geometry is specified by $d^2 k$ are described as

$$\begin{aligned} \nu^- &= f_1 f_2 d^3 v_1 d^3 v_2 S(\mathbf{k}\cdot\mathbf{v}_{12}) d^2 k \Delta t d^3 r_1 && (2.28)\\ \nu^+ &= f_1'' f_2'' d^3 v_1'' d^3 v_2'' S(\mathbf{k}\cdot\mathbf{v}_{12}'') d^2 k \Delta t d^3 r_1 && (2.29)\\ &= \Lambda f_1'' f_2'' d^3 v_1 d^3 v_2 S(\mathbf{k}\cdot\mathbf{v}_{12}) d^2 k \Delta t d^3 r_1 && (2.30) \end{aligned}$$

with

$$\Lambda \equiv \frac{1}{e}\frac{\partial(\mathbf{v}_1'', \mathbf{v}_2'')}{\partial(\mathbf{v}_1, \mathbf{v}_2)}, \tag{2.31}$$

where the Jacobian yields

$$\frac{\partial(\mathbf{v}_1'', \mathbf{v}_2'')}{\partial(\mathbf{v}_1, \mathbf{v}_2)} = \frac{1}{e}, \tag{2.32}$$

for $e = $ const. case. Thus, the Boltzmann equation for granular gas follows from the conservation of probability:

$$\frac{Df_1}{Dt} = \frac{\partial f_1}{\partial t} + \mathbf{v}_1 \cdot \nabla_1 f_1 = \int d^3 v_2 d^2 k S(\mathbf{k}\cdot\mathbf{v}_{12}) \left(\frac{1}{e^2} f_1'' f_2'' - f_1 f_2 \right). \tag{2.33}$$

The difference from elastic gas is that the existence of the homogeneous cooling state (HCS) due to the inelastic collisions. Because the kinetic energy dissipates through inelastic collisions, T_g, which is called the granular temperature, goes to zero as time passes. Although the exact solution is not known, the homogeneous solution for Eq. (2.33) is conventionally analyzed by using Sonine polynomial expansion:

$$f(\mathbf{v}, t) = f_M [1 + \sum_{p=1}^{\infty} a_p S_p(\mathbf{c}^2)], \tag{2.34}$$

with $\mathbf{c} \equiv \mathbf{v}_1 / \sqrt{2T_g(t)/m}$ and Sonine polynomials $S_p(x) (p = 0, 1, 2, \cdots)$, which satisfy the orthogonality conditions

$$\int d\mathbf{c} \frac{e^{-\mathbf{c}^2}}{\pi^{-3/2}} S_p(\mathbf{c}^2) S_{p'}(\mathbf{c}^2) = 2\delta_{pp'}(p + \frac{1}{2})!. \tag{2.35}$$

The first few Sonine polynomials in 3D read

$$S_0(x) = 1, \quad S_1(x) = -x + \frac{3}{2}, \quad S_2(x) = \frac{x^2}{2} - \frac{5x}{2} + \frac{15}{8}, \tag{2.36}$$

where the corresponding coefficients for f are known to be $a_1 = 0$ and

$$a_2 = \frac{16(1-e)(1-2e^2)}{81 - 17e + 30e^2(1-e)}, \tag{2.37}$$

which is derived by van Noije and Ernst [74] based on an earlier calculation by Goldstein and Shapiro [56]. The validity of the Sonine polynomial approximation is verified via DSMC simulation [75]. We note that one-dimensional granular gas violates equipartition of energy [76].

RET for granular flow

For the analysis in this paper, we adopt RET for the granular flow in 3D to treat moderate dense granular flow [52]

$$(\frac{\partial}{\partial t} + \mathbf{v}_1 \cdot \nabla_1) f(\mathbf{r}_1, \mathbf{v}_1, t) = J_E[\mathbf{r}_1, \mathbf{v}_1 | f(t)], \tag{2.38}$$

where collision operator for granular flow

$$\begin{aligned} J_E[\mathbf{r}_1, \mathbf{v}_1 | f(t)] \equiv & \int d^3\mathbf{v}_2 d^2k S(\mathbf{k} \cdot \mathbf{v}_{12}) \{\Lambda f^{(2)}(\mathbf{r}_1, \mathbf{v}_1''; \mathbf{r}_1 + \sigma\mathbf{k}, \mathbf{v}_2''; t) \\ & - f^{(2)}(\mathbf{r}_1, \mathbf{v}_1; \mathbf{r}_1 - \sigma\mathbf{k}, \mathbf{v}_2; t)\} \end{aligned} \tag{2.39}$$

is introduced. Here, two-body distribution function is approximated as

$$f^{(2)}(\mathbf{r}_1, \mathbf{v}_1; \mathbf{r}_2 \mathbf{v}_2; t) = \chi(\mathbf{r}_1, \mathbf{r}_2 | n(t)) f(\mathbf{r}_1, \mathbf{v}_1, t) f(\mathbf{r}_2, \mathbf{v}_2, t), \tag{2.40}$$

with the equilibrium pair-correlation function χ as a functional of density n and the Jacobian for constant restitution coefficient case $\Lambda = 1/e^2$,

From RET equation (2.38), the continuity equation for physical quantity $\psi = \psi(\mathbf{v}_1)$ can be calculated through integration $\int d^3v_1$ after multiplying ψ on Eq. (2.38):

$$\frac{\partial}{\partial t}\langle\psi\rangle = -\frac{\partial}{\partial x_\alpha} J_\alpha(\psi) + I(\psi), \tag{2.41}$$

where $\langle \cdots \rangle \equiv \int d^3v_1 f(\mathbf{x}_1, \mathbf{v}_1, t) \cdots$ and $J_\alpha = J_\alpha^c + J_\alpha^k$ with

$$J_\alpha^k \equiv \langle v_{1\alpha} \psi \rangle \tag{2.42}$$

$$\begin{aligned} J_\alpha^c \equiv & \frac{\sigma}{4} \int d^3v_1 d^3v_2 d^2k \int_0^1 d\lambda S(\mathbf{v}_{12} \cdot \mathbf{k}) k_\alpha \\ & \Delta'\psi f^{(2)}(\mathbf{r}_1 + \sigma\mathbf{k}(1-\lambda), \mathbf{v}_1; \mathbf{r}_1 - \lambda\sigma\mathbf{k}, \mathbf{v}_2; t), \end{aligned} \tag{2.43}$$

$$I(\psi) \equiv \frac{1}{2} \int d^3v_1 d^3v_2 d^2k S(\mathbf{v}_{12} \cdot \mathbf{k}) \Delta\psi f^{(2)}(\mathbf{r}_1 + \sigma\mathbf{k}, \mathbf{v}_1; \mathbf{r}_1 \mathbf{v}_2; t), \tag{2.44}$$

with $\Delta'\psi \equiv (\psi_1' - \psi_1) - (\psi_2' - \psi_2)$ and $\Delta\psi \equiv (\psi_1' - \psi_1) + (\psi_2' - \psi_2)$. Hydrodynamical equations are derived by integrating over $\int d^3v_1$ after multiplying $1, v_{1\alpha}, \mathbf{v}_1^2/2$:

$$(\partial_t + \bar{v}_\beta \partial_\beta) n = -n \partial_\beta \bar{v}_\beta, \tag{2.45}$$

$$(\partial_t + \bar{v}_\beta \partial_\beta) \bar{v}_\alpha = -\frac{1}{mn} \partial_\beta \sigma_{\alpha\beta}, \tag{2.46}$$

$$(\partial_t + \bar{v}_\beta \partial_\beta) T_g = -\frac{2}{3n} \{\partial_\beta q_\beta + (\partial_\beta \bar{v}_\alpha) \sigma_{\alpha\beta}\} - \zeta T_g, \tag{2.47}$$

with density $n \equiv \int d^3v_1 f(\mathbf{x}_1, \mathbf{v}_1, t)$, velocity filed $\bar{v}_\alpha \equiv \int d^3v_1 v_1 f(\mathbf{x}_1, \mathbf{v}_1, t)/n$, granular temperature $T_g \equiv \int d^3v_1 m \mathbf{u}_1^2 f(\mathbf{x}_1, \mathbf{v}_1, t)/3n$ and $u_{1\alpha} \equiv v_{1\alpha} - \bar{v}_\alpha$. Here,

the stress tensor $\sigma_{\alpha\beta}$, the heat flux q_α and the cooling rate ζ are introduced:

$$\sigma_{\alpha\beta} = \sigma^k_{\alpha\beta} + \sigma^c_{\alpha\beta}, \tag{2.48}$$

$$\sigma^k_{\alpha\beta} \equiv m\langle u_{1\alpha}\tilde{u}_{1\beta}\rangle, \tag{2.49}$$

$$\sigma^c_{\alpha\beta} \equiv \frac{\sigma^3 m(1+e)}{4}\int dv_1^3 dv_2^3 \int d^2k\Theta(g_{12})g_{12}^2 k_\alpha k_\beta f^{(2)}(\mathbf{r}_1+\sigma\mathbf{k}(1-\lambda),\mathbf{v}_1;\mathbf{r}_1-\lambda\sigma\mathbf{k},\mathbf{v}_2;t), \tag{2.50}$$

$$q_\alpha = q^k_\alpha + q^c_\alpha, \tag{2.51}$$

$$q^k_\alpha \equiv m\langle u_{1\alpha}\mathbf{u}_1^2\rangle/2, \tag{2.52}$$

$$q^c_\alpha \equiv \frac{\sigma^3 m}{4}\int d^3v_1 d^3v_2 d^2k\Theta(g_{12})2(1+e)g_{12}^2 \tilde{V}_{12\beta}k_\beta k_\alpha f^{(2)}(\mathbf{r}_1+\sigma\mathbf{k}(1-\lambda),\mathbf{v}_1;\mathbf{r}_1-\lambda\sigma\mathbf{k},\mathbf{v}_2;t), \tag{2.53}$$

$$\zeta \equiv -\frac{I(m\mathbf{v}^2)}{3nT_g}, \tag{2.54}$$

with $g_{12} \equiv \mathbf{v}_{12}\cdot\mathbf{k}$, $\tilde{V}_{12\alpha} \equiv V_{12\alpha} - \bar{v}_\alpha$ and $\mathbf{V}_{12} \equiv (\mathbf{v}_1+\mathbf{v}_2)/2$. The detail derivations for Eqs. (2.41) and (2.45)-(2.47) are shown in Appendix A.

Treatment of the Rotational Degrees of Freedom

To solve hydrodynamical equations for frictional grains is laborious work. Including the collision rule of frictional grains, hydrodynamical equations can be derived from Enskog equations. However, in addition to equations for the translational degree of freedoms $(n, \bar{\mathbf{v}}, T_g)$, those for the angular velocity fields $\bar{\boldsymbol{\omega}} \equiv \sum_i \boldsymbol{\omega}_i$ and the rotational temperature $T_{\rm rot} \equiv \sum_i I_0(\boldsymbol{\omega}_i - \bar{\boldsymbol{\omega}})^2/2$ with moment of inertia of grains I_0 are necessary, which are quite complicated [54–62].

This difficulty can be avoided in the case of the slightly frictional grains, i.e. small μ_p case, where the effect of the tangential contact in collisions can be absorbed in the renormalized restitution coefficient [63,64]. For the slightly frictional spheres, Jenkins and Zhang [63] suggested that hydrodynamical equations for frictional grains are reduced to those for translational degree of freedoms by introducing an effective restitution coefficient $\bar{e}$

$$\bar{e} = e - \frac{\pi}{2}\mu_p + \frac{9}{2}\mu_p^2 + O(\mu_p^3), \tag{2.55}$$

as an expansion about μ_p, if the friction constant μ_p is small. The validity of three dimensional theory [63] has been tested by Xu *et al* [65] and Jenkins and Zhang [63]. The latter is consistent with Lun and Bent [66] in part. The validity of the case for slightly frictional disks [64] has been verified by Saitoh and Hayakawa [67, 68]. Although the correlation between velocity and angular velocity of grains has been argued at the level of velocity distribution functions (VDFs) [59,62], the transport coefficients for large μ_p case have not been derived, to our knowledge.

2.2 Rheology of the Dense Granular Flow

Rheology for dense granular flow, where the grains are almost in contact, has been discussed by many researchers [104–149]. Because the kinetic theory might not be valid above the volume fraction $\phi \sim 0.50$, which is known to be Alder transition point [150–156], the first principle studies for the dense granular flow are limited [104–109] and there are many phenomenologies, such as Bagnold scaling [110–125], granular friction [126–135] and the scaling theory of jamming transitions [136–149].

2.2.1 Bagnold Scaling

A typical experiment for dense granular flow would be the flow on a inclined plane [110–112]. Bagnold proposed a constitutive equation that the shear stress is proportional to the square of the shear rate [110], so called Bagnold scaling, which is verified experimentally [111] and numerically [112].

The validity of the Bagnold scaling has been investigated under several conditions such as the flow down on a inclined plane [113–117], shear flow under a constant pressure [118, 126, 131] and the Lees-Edwards boundary conditions [114, 119–122]. Under the inclined flow condition, Mitarai and Nakanishi suggested that the Bagnold scaling is reproduced from the kinetic theory [113] and, Lee and Huang recently proposed kinetic-theory-based phenomenological model to reproduce the Bagnold scaling [117]. Under the Lees-Edwards boundary conditions, which is the periodic boundary conditions for the shear flow [123], the stability of the uniform shear flow using DEM [67, 68], hydrodynamical equations [67, 68, 119–122] or time dependent Ginzburg-Landau equations [124, 125], where the Bagnold scaling is no longer valid, because of the inhomogeneous spatial sstructure.

2.2.2 Granular Friction

Physics of dry friction is one of the oldest problems, which has been investigated by da Vinci, Amonton and Coulomb. In particular, the dynamics of granular flow, which is ubiquitous in the earth science and the engineering, is governed by a law that describes the behavior of effective friction constant μ^*, which is defined as the ratio of the shear stress to the normal stress. Examples are avalanches or land- slides. The frictional properties of granular flow, so-called granular friction, has been extensively studied experimentally, numerically and theoretically. The present status of statistical physics of fracture, friction, and earthquakes is summarized in Ref. [135].

The noteworthy experimental research is a paper by the French research collective GDR MiDi - the Groupement de Recherche sur les Milieux Divisés-, comparing flows in several experimental setup, such as plane shear, annular shear, vertical-chute flows, inclined plane, heap flow and rotating drum, to specify the common frictional properties of granular flow [126]. GDR MiDi found that the behavior of the μ^* in several setups can be described as the function of

the inertial number I, which is the ratio of inertial forces of grains to external forces, i.e. shear rate $\dot{\gamma}$:

$$I_D \equiv \frac{\dot{\gamma}}{\sqrt{P\sigma^{D-1}/m}}, \tag{2.56}$$

with dimensions D. Since the appearance of the paper by GDR MiDi, the research using I_D has been popular [128–134].

There are mainly two constitutive equations for μ^*. Jop and co-workers presented a simple friction law that describes flow on inclined planes, which is investigated through massive simulations and experiments [127–130]:

$$\mu^* = \mu_s + \frac{\mu_{\max} - \mu_s}{1 + I_0/I_D}, \tag{2.57}$$

with constants $\mu_s, \mu_{\max}$ and I_0. Eq. 2.57 describes the static behavior $I_D \to 0$ of dense granular flow $\mu^* = \mu_s$ and as I_d becomes larger, μ^* saturate to the maximum value $\mu_{\max}$, monotonically.

Some researchers proposed a different constitutive equation

$$\mu^* = \mu_s + bI_D^{\beta}, \tag{2.58}$$

with constants b and β, which also reproduces numerical simulations [131, 133, 134].

2.2.3 Jamming Transition

A granular system has rigidity above a critical value of density ϕ_J and does not have any rigidity below ϕ_J. This sudden change in rigidity is known as the jamming transition [136–149]. The jamming is not only investigated in the system of grains, but also that of colloidal suspensions [157] and foams [158] . Here, ϕ_J decreases as the friction constant μ_p of grains increases. Moreover, it seems that there are two fictitious jamming points except for the true jamming point for finite μ_p [137]. Critical exponents of the divergence of pressure and the shear viscosity near the transition are extensively discussed [137–149] and the current status are summarized in Ref. [149].

The first principle study for the jamming transition is performed through the theory of "granular-liquid," where long-time, long-range correlations are significant, as well as in molecular liquids [104–109]. Mode Coupling Theory (MCT) has been applied for the glassy behavior of the molecular liquids. Although MCT is still not completely established as a theory of glasses, MCT seems to capture partial aspects of the glass transition and its problem is not serious at least for sheared systems. The conventional approach of projection operators and the Mori-type equations [159, 160] are applied for the dense granular flow under the shear [109].

Chapter 3

Discrete Element Method

In this chapter, we explain the simulation model we used. We adopt the Discrete Element Method (DEM) for grains with identical mass m proposed by Cundall and Strack [45]. In this method, a grain is assumed to be a disk or a sphere and the interaction is repulsive (elastic) force and dissipative (viscous) force.

When the sphere i at the position $\mathbf{r}_i$ and the sphere j at $\mathbf{r}_j$ are in contact $R_i + R_j > r_{ij}$, the normal force F_{ij}^n and tangential forces F_{ij}^t and F_{ij}^s are described as

$$F_n^{ij} = -k_n u_n^{ij} - \eta_n \dot{u}_n^{ij} \tag{3.1}$$

$$F_t^{ij} = \begin{cases} \tilde{F}_t^{ij} & (\tilde{F}_t^{ij} < \mu_p |F_n^{ij}|) \\ -\mu |F_n^{ij}| & (\mu_p |F_n^{ij}| \leq F_t^{ij}) \end{cases} \tag{3.2}$$

$$F_s^{ij} = \begin{cases} \tilde{F}_s^{ij} & (\tilde{F}_s^{ij} < \mu_p |F_n^{ij}|) \\ -\mu |F_n^{ij}| & (\mu_p |F_n^{ij}| \leq F_s^{ij}) \end{cases} \tag{3.3}$$

with $\tilde{F}_t^{ij} \equiv -k_t u_t^{ij} - \eta_t \dot{u}_t^{ij}$ and $\tilde{F}_s^{ij} \equiv -k_t u_s^{ij} - \eta_t \dot{u}_s^{ij}$, by using the relative displacement ${}^t(u_t, u_s, u_n)$ in normal direction u_n and tangential directions u_t, u_s, where the dot denotes the time derivative, and the radii of i th and j th particle R_i and R_j, respectively. In the case of the collisions of disks, only F_n^{ij} and F_t^{ij} are adopted. μ_p is the friction constant. The detailed implementation of DEM is explained in Appendix B.

Here, we adopt parameters $k_t = 0.2k_n, \eta_t = 0.5\eta_n$. We write adopted values of other parameters k_n, η_n and μ_p in each Chapter. We use the maximum diameter of grains $d \equiv \max_i\{2R_i\}$ as a unit of the length, d/u_0 with the incident velocity of the jet u_0 as a unit of the time and m as a unit of the mass. These parameters are related to the duration time t_c and the restitution coefficient e:

$$t_c = \frac{\pi}{\sqrt{\frac{2k_n}{m} - \eta_n^2}} \tag{3.4}$$

$$e = \exp[-t_c \eta_n]. \tag{3.5}$$

We mainly use the value of $\mu_p = 0.2$ close to the experimental value for nylon

spheres [165]. The second-order Adams-Bashforth method for the time integration with the time interval $\Delta t = 0.02 t_c$ is adopted.

The initial granular temperature, which represents the fluctuation of particle motion, is zero. The wall consists of one-layer of DEM particles with the same diameter d and the same mass m, which are connected to each other and with their own initial positions via the spring and the dashpot with spring constant $k_w = 10.0 m u_0^2/d^2$ and the dashpot constant $\eta_w = 5.0\eta_n$, respectively. The interaction between a grain and a wall particle is calculated via DEM, while that between wall particles is done only via the spring k_w and the dashpot η_w.

In 3D, initial configurations are generated as follows: We prepare fcc crystals and remove particles randomly to reach the desired density. We control the initial volume fraction $\phi_0/\phi_{\rm fcc} \equiv \tilde{\phi}_0$ before the impact as $0.30 \leq \tilde{\phi}_0 \leq 0.90$ with volume fraction for a fcc crystal $\phi_{\rm fcc} \simeq 0.74$ and 20,000 particles are used. We average numerical data over the time $50.0 \leq t u_0/d \leq 100.0$ after the impact.

In 2D, initial configurations are generated as follows: We prepare a triangular lattice with distance between grains $1.1d$ and remove particles randomly to reach the desired density. We control the initial area fraction $\phi_0/\phi_{\rm ini} \equiv \tilde{\phi}_0$ before the impact as $0.30 \leq \tilde{\phi}_0 \leq 0.90$ with the initial area fraction before the removal $\phi_{\rm ini} = 0.612, 0.780$ for the bi-disperse and the mono-disperse case, respectively, and 8,000 particles are used. We average numerical data over the time $180.0 \leq t u_0/d < 300.0$ after the impact.

Chapter 4

Scattered States of Granular Jets

In this chapter, we discuss the scattered states of granular jets. We focus on the crossover of the scattering angle, depending on the ratio of the target diameter and the jet diameter, and the effect of the initial anisotropy of the cross section of the jet. We use the particles with $\mu_p = 0.2$ and coefficients of the restitution from 0.75 to 0.99, where the corresponding parameters are summarized in the Table 4.1.

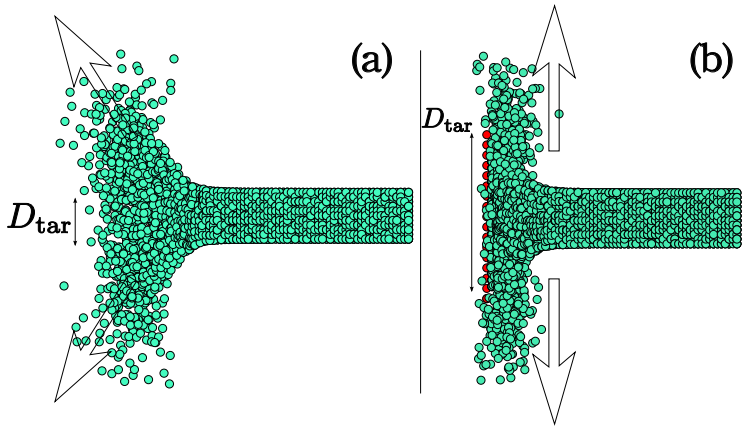

Figure 4.1: The side view of snapshot for the three dimensional simulation. Green colored particles denote grains, and red colored particles are wall particles. For $D_{\mathrm{tar}}/D_{\mathrm{jet}} = 0.8$, cone-like scattered jet is reproduced (a), where wall particles are hidden by scattered jet. For $D_{\mathrm{tar}}/D_{\mathrm{jet}} = 2.5$, sheet-like scattered jet is reproduced (b).

Table 4.1: Table for k_n, η_n and e for $t_c = 0.10d/u_0$

e	$k_n d^2/mu_0^2$	$\eta_n d/u_0$
0.75	4.98×10^2	2.88
0.80	4.96×10^2	2.23
0.90	4.94×10^2	1.05
0.99	4.93×10^2	0.101

4.1 Scattering Angle

Experimentally, it is known that the scattered state exhibits the crossover from a cone-like pattern and a sheet-like pattern by changing $X \equiv D_{\rm tar}/D_{\rm jet}$ with the jet diameter $D_{\rm jet}$ and the target diameter $D_{\rm tar}$. The crossover can be reproduced through DEM, where the jet diameter $D_{\rm jet}$ is fixed $D_{\rm jet}/d = 4.5$ (Fig. 4.1). Green particles are grains and red ones are wall particles. Figure 4.1 (a) is a typical con-like pattern with $D_{\rm tar}/D_{\rm jet} = 0.8$. Figure 4.1 (b) is an example of the sheet-like pattern with $D_{\rm tar}/D_{\rm jet} = 2.5$ (b). We note that wall particles are hidden in (a).

4.1.1 Theory for the scattering angle

A phenomenological model for the scattering angle has been proposed by Clanet [26]. Clanet assumes that the scattered momentum flux $j_{\rm sc}$ is conserved after the impact. In our case, since grains collide inelastically, the assumption may not be correct. However, with simple modification, their results can be reproduced.

The momentum flux of the incident jet $j_{\rm in}$ is scattered with scattering angle ψ_0 and width of the flux $h(r)$ at distance r, where cylindrical axis is chosen. Conservations of the mass and the momentum flux are, respectively, described as

$$\pi D_{\rm tar} h(\frac{D_{\rm tar}}{2}) j_{\rm sc} - \frac{\pi D_{\rm jet}^2}{4} j_{\rm in} = 0 \tag{4.1}$$

$$\pi D_{\rm tar} h(\frac{D_{\rm tar}}{2}) j_{\rm sc} \cos\psi_0 - \frac{\pi D_{\rm jet}^2}{4} j_{\rm in} = -F_{\rm wall}, \tag{4.2}$$

with the force from the wall $F_{\rm wall}$. From Eqs. (4.1) and (4.2), the equation for ψ_0 is obtained:

$$\frac{4A_{\rm cs}}{\pi D_{\rm jet}^2} = 1 - \cos\psi_0 \simeq \frac{\psi_0^2}{2}, \tag{4.3}$$

where total cross section $A_{\rm cs} \equiv F_{\rm wall}/j_{\rm in}$ is introduced. Let us think of the asymptotic behavior for cases $X \gg 1$ and $X \ll 1$. For $X \gg 1$, $A_{\rm sc} \propto \pi D_{\rm jet}^2/4$. With constant C_0,

$$\psi_0 \simeq C_0. \tag{4.4}$$

On the other hand, for $X \ll 1$, with $A_{\rm sc} \propto \pi D_{\rm tar}^2/4$,

$$\psi_0 \simeq C_1 X, \tag{4.5}$$

with constant C_1. ψ_0 depends linearly on X.

4.1.2 Numerical results for the scattering angle

The scattering angle ψ_0 for the frictional case with $\tilde{\phi}_0 = 0.90$, and $D_{\rm jet}/d = 4.5$ for several e exhibits a crossover from a cone-like structure to a sheet-like one, depending on $X \equiv D_{\rm tar}/D_{\rm jet}$, which is almost independent of the restitution coefficient [166](Fig. 4.2). We average the data over ten different initial configurations in the followings. The dotted lines in Fig. 4.2, $\psi_0 = C_0$ for $X \gg 1$ and $\psi_0 = C_1 X + C_2$ for $X \ll 1$, are asymptotic lines, where constant C_2 is introduced for the fitting. The solid line is an interpolation function $\psi_0 = \sqrt{C_0'^2\{1 - \exp(-C_1^2 X^2/C_0'^2)\} + C_2}$, which reproduces the asymptotic behavior for ψ_0 with $C_0' \equiv C_0 - C_2$. We obtain fitting parameters $C_0 = 1.68, C_1 = 0.563$ and $C_2 = 0.554$ by fitting the interpolation function to the numerical data. Thus, the crossover from the con-like pattern and the sheet-like pattern, which is reported in Ref. [31], can be reproduced by our model qualitatively.

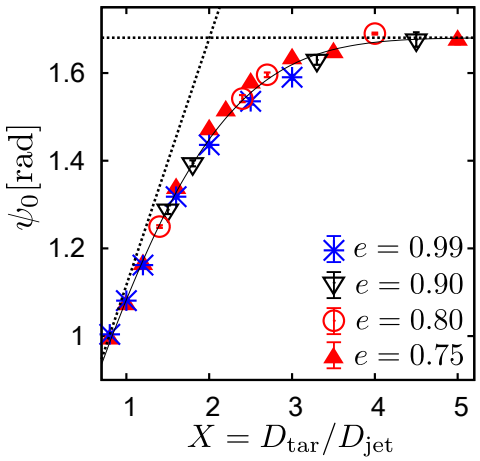

Figure 4.2: The dependence of ψ_0 [rad] on X for the frictional case with $\tilde{\phi}_0 = 0.90$, $e = 0.75$ and $D_{\rm jet}/d = 4.5$. Here, ψ_0 does not depend on the restitution coefficient. The dotted lines are asymptotic ones $\psi_0 = C_0$ for $X \gg 1$ and $\psi_0 = C_1 X + C_2$ for $X \ll 1$ and the solid line is the interpolation function. The asymptotic behavior which is observed in experiments [31] is obtained.

4.2 On the effect of initial anisotropy

To estimate the effect of the initial spatial anisotropy, v_2, which is the coefficient of $\cos 2\varphi$ with the azimuthal angle φ for scattering flux $dN/d\varphi$, is conventionally used [3]. The scattering flux $dN/d\varphi$ is related to the differential scattering cross section $d\sigma(\theta, \varphi)/d\Omega$ with the scattering angle θ and the other coefficients v_n

with $n = 0, 1, \cdots$ as

$$\frac{dN}{d\varphi} \equiv \int \frac{d\sigma}{d\Omega} d\cos\theta = \sum_{n=0}^{\infty} v_n \cos n\varphi. \tag{4.6}$$

If the fluid behaves as a perfect fluid, v_2/ε is expected to be a constant for ε, where ε is the eccentricity $\varepsilon = (l^2 - 1)/(l^2 + 1)$ with an aspect ratio l for an initial rectangular cross section of the jet. The aspect ratio is changed with fixing the area for the cross section to $16d^2$. Although v_2 is enhanced as ε increases, the observed v_2 is not proportional to ε for $e = 0.75$ (Fig. 4.3). We also indicate that Ref. [31] only reports one parameter of $v_2 = 0.16$ and $\varepsilon = 0.615$ and thus, they cannot discuss whether v_2 is proportional to ε. It should be noted, however, that our v_2 is much smaller than the experimental value for the same ε.

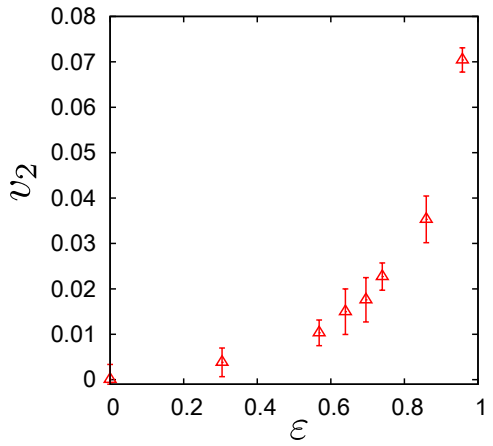

Figure 4.3: (Color online) The dependence of v_2 on ε for the frictional case with $\tilde{\phi}_0 = 0.90$ and $e = 0.75$, where the initial cross section of the jet is fixed to $16d^2$. v_2 does not linearly depend on ε. It should be noted that the observed v_2 is much smaller than the value reported in Ref. [31].

Chapter 5

Rheology of Granular Jets in Three Dimensions: Is granular flow really a "perfect fluid?"

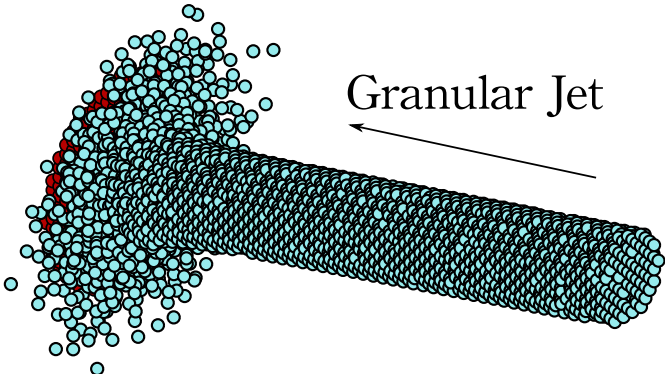

Figure 5.1: Snapshot of a three-dimensional simulation. Sky-blue-colored particles are grains and red ones are wall particles. Grains consisting of a regular lattice with missing particles collide on a bumpy wall, where grains are scattered randomly, and the jet ejected along with the wall.

In this chapter, we investigate the rheology of granular jets in 3D. We use both frictional $\mu_p = 0.2$ and frictionless grains with $e = 0.75$ and k_n, η_n for Table 4.1. A typical snapshot of our simulation is shown in Fig. 5.1. We evaluate physical quantities near the wall at the height $z = \Delta z \equiv 5.0d$ from the wall $z = 0$. The jet diameter $D_{\rm jet}/d = 10.0$ and the target diameter $D_{\rm tar}/d = 22.0$

are fixed. We divide the system into cylindrical calculation region in the radial direction $r = 0, \Delta r, \cdots, 5\Delta r$, with $\Delta r \equiv R_{\rm tar}/5$ and the target radius $R_{\rm tar}$, and estimate physical quantities in the corresponding mesh region with $k\Delta r < r < (k+1)\Delta r$ $(k = 0, 1, \cdots, 5)$, where r is denoted to the distance from the symmetric axis of the cylindrical coordinate(Fig. 5.2).

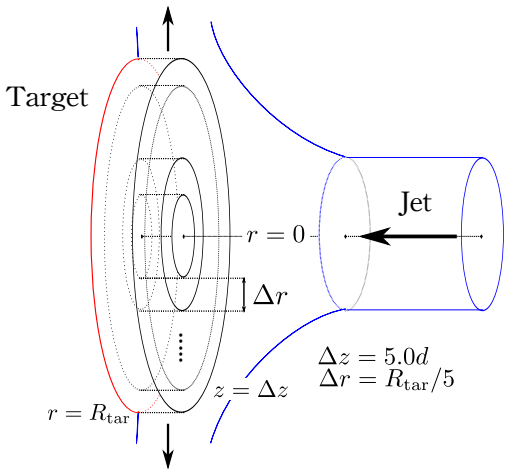

Figure 5.2: A schematic picture of the calculation region. The cylinder with radius $R_{\rm tar}$ and height $5d$ is divided into cylindrical mesh, where physical quantities are estimated.

5.1 Profiles of Stress Tensor

Let us evaluate the stress tensor near the wall as in Appendix C. The microscopic definition of the stress tensor at $\mathbf{r}$ is given by

$$\sigma_{\alpha\beta}(\mathbf{r}) = \frac{1}{V}\sum_i m u_{i\alpha} u_{i\beta} + \frac{1}{V}\sum_{i<j} F_\alpha^{ij} r_\beta^{ij}, \tag{5.1}$$

where i and j are indices of particles, $\alpha, \beta = r, \theta, z$ denote cylindrical coordinates and $\sum$ denotes the summation over the particles located at $\mathbf{r}$. Here, z axis is parallel to the incident jet axis, and V is the volume of each mesh at $\mathbf{r}$ and $u_{i\alpha} = v_\alpha^i - \bar{v}_\alpha(\mathbf{r})$ with the mean velocity $\bar{v}_\alpha(\mathbf{r})$ in the mesh at $\mathbf{r}$. To calculate the stress tensor in cylindrical coordinates, we firstly calculate $\sigma_{\alpha'\beta'}$ in Cartesian coordinate, $\alpha', \beta' = x, y, z$, whose origin is the same as cylindrical one, and transform it into that for cylindrical one.

Here we show the profile of the stress tensor for the frictional case (Fig. 5.3 for $\tilde{\phi}_0 = 0.90$). From Fig. 5.3, it is apparent that off-diagonal components of the stress tensor σ_{rz} and σ_{zr} are much smaller than diagonal components, where the ratio of the off-diagonal to the diagonal element is estimated as $|\sigma_{rz}/\sigma_{zz}| \simeq$

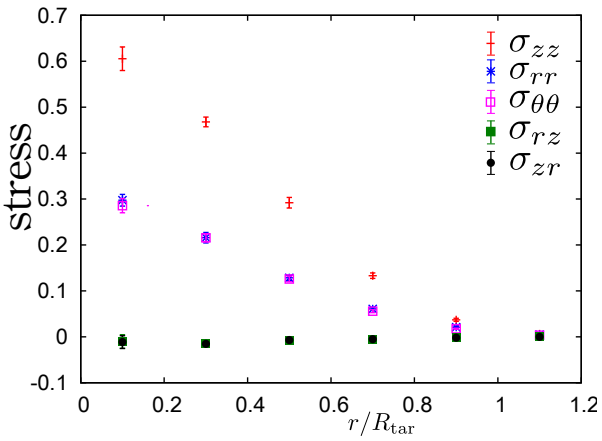

Figure 5.3: The profile of the stress tensor $\sigma_{\alpha\beta}(mu_0^2/d^3)$ as the functions of distance from the jet axis r with $R_{\rm tar}$ for frictional grains with $\tilde{\phi}_0 = 0.90$. The off-diagonal components of the stress tensor σ_{rz} and σ_{zr} are much smaller than diagonal components as $|\sigma_{rz}/\sigma_{zz}| \simeq 1.7 \times 10^{-2}$ at $r/R_{\rm tar} = 0.1$.

1.7×10^{-2} at $r/R_{\rm tar} = 0.1$. This result supports that the solution of Euler equation well reproduce the granular flow after the impact [38]. We also found that there exists a large normal stress difference, i.e. the difference between diagonal components of $\sigma_{\alpha\beta}$, which is also observed in our two-dimensional case. We obtain the ratio $|\sigma_{rz}/\sigma_{zz}| \simeq 3.0 \times 10^{-2}$ at $r/R_{\rm tar} = 0.1$ for the frictionless case, where off-diagonal components are much smaller than diagonal ones as in the case of the frictional case.

5.2 Velocity profile

The profile of $\bar{v}_r$ and $\sqrt{T_g/m}$ for the frictional case is shown in Fig. 5.4, with the granular temperature $T_g(\mathbf{r}) \equiv \sum_{i\alpha} mu_{i\alpha}^2(\mathbf{r})/3N$. Ellowitz *et al.* suggests that the dead zone, where the motion of grains is frozen, exist near the target in 2D [38, 39]. However, as is shown in Fig. 5.4, although the velocity of grains at the center is small, the fluctuation of the particle velocity $\sqrt{T_g/m}$ is the largest at the center. Thus, the motion of particles near the target in 3D is not frozen. Namely, there is no dead zone in 3D granular jets.

5.3 Comparison with the Kinetic Theory

5.3.1 Pressure

Let us look at the result of the pressure (Fig. 5.5). It is known that the granular sheared flow such as a chute flow and a plane shear flow can be approximately

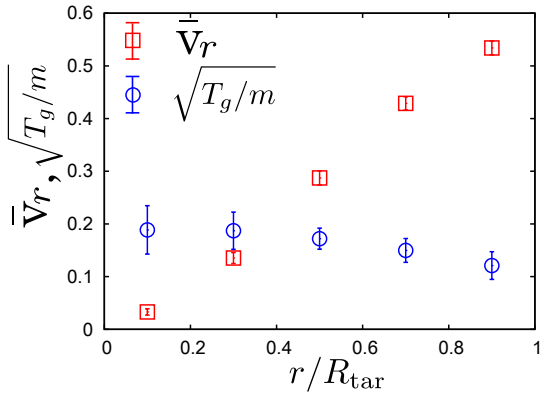

Figure 5.4: The profile of the radial component of the velocity field $\bar{v}_r$ and $\sqrt{T_g/m}$.

described by granular hydrodynamics with transport coefficient derived from kinetic theory, i.e. the Enskog equation [51–53, 56, 63, 64, 67]. We compare our simulation with the transport coefficients derived by Garzó and Dufty [52] with the pressure $P \equiv \sum_\alpha \sigma_{\alpha\alpha}/3$, the density n, the volume fraction ϕ, and the granular temperature $T_g(\mathbf{r})$. The pressure is conventionally given by

$$\frac{P}{nT_g} = 1 + 2\phi(1+e)\chi, \tag{5.2}$$

$$\chi = \begin{cases} \frac{1-\phi/2}{(1-\phi)^3} & (0 < \phi < \phi_f) \\ \frac{(1-\phi_f/2)(\phi_c-\phi_f)}{(1-\phi_f)^3(\phi_c-\phi)} & (\phi_f < \phi < \phi_c), \end{cases} \tag{5.3}$$

where $\phi_f = 0.49$ and $\phi_c = 0.64$ [103]. For the frictional case $\mu_p = 0.2$, we use the renormalization of e in Eq. (2.55). According to this simplification we use the effective restitution coefficient $\bar{e} = 0.616$ for $e = 0.75$ and $\mu_p = 0.2$, for frictional case in the following analysis.

Let us compare the theoretical curve with numerical results for several $\tilde{\phi}_0$ (Fig. 5.5). The black solid line in Fig. 5.5 and that in the inset denote the theoretical curves for the frictionless case and the frictional case, respectively. Surprisingly, the expression for the pressure in Eq. (5.2) well reproduces the numerical result for $\phi < 0.5$ inspite of the existence of the normal stress difference i.e. $\sigma_{zz} > \sigma_{\theta\theta} \simeq \sigma_{rr}$, while Eq.(5.2) for $0.5 < \phi < 0.6$ may have significant deviation from the theoretical line. The deviation, which may result from the singularity near the symmetrical axis $r \simeq 0$ of the cylindrical coordinate, emerges only at $r/R_{\rm tar} = 0.1$.

5.3.2 Anisotropic Temperature

Although there exists large normal stress differences, our numerical results can be reproduced from the empirical relation (5.2), if we introduce an anisotropic

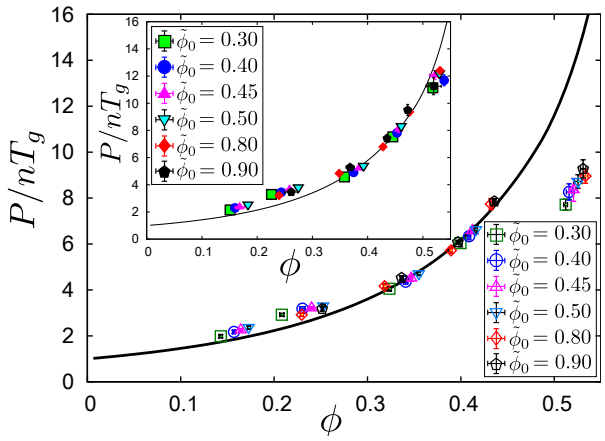

Figure 5.5: The comparison between the theoretical pressure in Eq. (5.2) and the observed pressure for several $\tilde{\phi}_0$, where the vertical axis is P divided by the density n and the granular temperature T_g for the frictionless case. The inset denotes comparison among those for the frictional case. The black solid lines in these figures denote Eq. (5.2) for the frictionless and the frictional case, respectively.

temperature. Indeed, equations of state for each coordinate satisfies, $P_\alpha = nT_\alpha\{1 + 2\phi(1 + e)\chi\}$ for $\alpha = r, \theta, z$ and $P_r = \sigma_{rr}$, $P_\theta = \sigma_{\theta\theta}$ and $P_z = \sigma_{zz}$. By summing up $P_\alpha = nT_\alpha\{1 + 2\phi(1 + e)\chi\}$ over α, we can reproduce Eq. (5.2). From Fig. 5.6, we verify that P_z/nT_z and P_r/nT_r are on the theoretical curve for isotropic systems, but P_θ/nT_θ has a systematically larger value from the isotropic one. Although our suggestion that the anisotropy of the stress only reflects on the anisotropy of the kinetic temperature is not perfect, the result gives a reasonable physical picture, at least, for r and z directions.

5.3.3 Constitutive Equation

Here, let us estimate the constitutive equations for granular jets. Let us evaluate the shear viscosity from the data of the stress tensor. The theoretical shear viscosity for frictionless granular fluids, which depends on temperature and volume fraction, is given by

$$\sigma_{rz} = -\eta_{\rm kin} D_{rz}, \tag{5.4}$$

$$\eta_{\rm kin}(\phi, T_g) = \frac{5}{16d^2}\sqrt{\frac{mT_g}{\pi}}\eta^*(\phi) \tag{5.5}$$

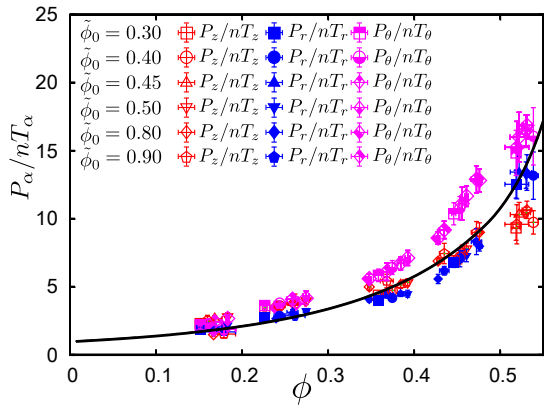

Figure 5.6: The diagonal components of the stress tensor for the frictional case with several $\tilde{\phi}_0$ divided by nT_α, where T_α is the temperature for α direction $T_\alpha \equiv \sum_i m u_{i\alpha}^2/N$. Red empty points, blue filled points, purple half-filled points and the solid black line denote $P_z/nT_z, P_r/nT_r, P_\theta/nT_\theta$ and Eq. (5.2), respectively.

with strain rate $D_{rz} \equiv (\partial \bar{v}_r/\partial z + \partial \bar{v}_z/\partial r)/2$. The dimensionless shear viscosity $\eta^*(\phi)$ [52] is described as

$$\eta^*(\phi) \equiv \eta^{k*}\{1 + \frac{4\phi\chi(1+e)}{5}\} + \frac{3\gamma^*}{5} \tag{5.6}$$

$$\eta^{k*}(\phi) \equiv \frac{1 - 2(1+e)(1-3e)\phi\chi/5}{\nu_\eta^* - \zeta^*/2} \tag{5.7}$$

$$\gamma^*(\phi) \equiv \frac{128}{5\pi}\phi^2\chi(1+e)(1-\frac{c^*}{32}) \tag{5.8}$$

$$\nu_\eta^*(\phi) \equiv \chi[1 - \frac{(1-e)^2}{4}][1 - \frac{c^*}{64}] \tag{5.9}$$

$$\zeta^*(\phi) \equiv \frac{5}{12}\chi(1-e^2)(1+\frac{3c^*}{32}) \tag{5.10}$$

$$c^* \equiv \frac{32(1-e)(1-2e^2)}{81 - 17e + 30e^2(1-e)}. \tag{5.11}$$

The shear viscosity is usually evaluated by plotting data points on a σ_{rz} vs D_{rz} plane. However, as shown in Appendix D, if we plot data for each mesh on the plane, the shear viscosity evaluated from a slope on the plane is negative, which is totally unphysical. This negative slope is caused by large density and temperature variations in each mesh. Therefore, the viscosity may be estimated locally by using density and temperature in the corresponding mesh.

For the frictional case, the yield stress σ_Y, which is the residual stress without deformation may exist in general. Thus, the constitutive equation in Eq. (5.4) is replaced by $\sigma_{rz} = \sigma_Y - \eta D_{rz}$, for this case. However, in this paper, we assume $\sigma_Y = 0$. The reason for the absence of the yield stress is based on the following observations.

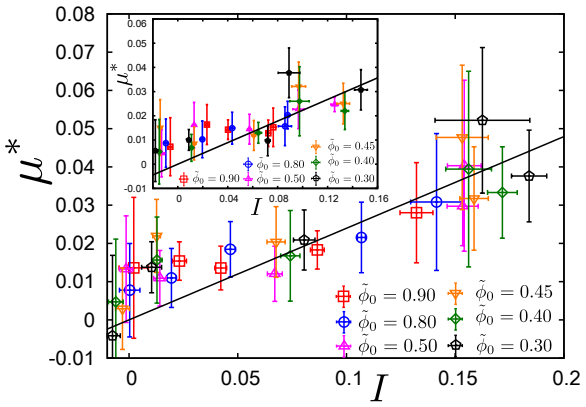

Figure 5.7: Analysis on the μ^* vs I plane. Numerical data can be fitted into black solid lines $\mu^* = aI$.

On the assumption of the zero yield stress

We show that the assumption of the zero yield stress would be natural, by introducing the effective friction coefficient. Let us analyze the friction coefficient, following the ref. [131]. We estimate strain rate D_{rz} as $\partial \bar{v}_r(r, \Delta z/2)/\partial z \simeq (\bar{v}_r(r, 3\Delta z/4) - \bar{v}_r(r, \Delta z/4))/(\Delta z/2)$ and $\partial \bar{v}_z(r,z)/\partial r \simeq (\bar{v}_z(r+\Delta r/2, z) - \bar{v}_z(r-\Delta r/2, z))/\Delta r$. Since we evaluate the physical quantities near the wall, the mesh $0 < z < \Delta z$ is divided into $0 < z < \Delta z/2$ and $\Delta z/2 < z < \Delta z$ to calculate $\partial \bar{v}_r(r, \Delta z/2)/\partial z$ and $0 < r < R_{\rm tar}$ is divided into $0 < r < \Delta r/2, \Delta r/2 < r < 3\Delta r/2, \cdots$.

Introducing the effective friction coefficient $\mu^* \equiv -\sigma_{rz}/P$ and the inertia number $I \equiv D_{rz}\sqrt{P/md}$, we plot the observed data μ^* vs I in Fig. 5.7. From the result of simulation, the obtained effective friction coefficient μ^* can be fitted by $\mu^* = aI$ with a constant a within error bars, where fitting values are $a = 0.240$ and $a = 0.223$ for frictional and frictionless case, respectively. The solid lines represent the corresponding fitting lines. Judging from the fitting, the assumption of zero yield stress in our setup [47] would be natural.

There are other three reasons. The first reason is the velocity distribution function. It is known that the significant effect of Coulombic slip may appear in the non-Gaussianity of velocity distribution functions (VDF), which is characterized by flatness of them. For grains in a vibrating container, the VDF are near to the Gaussian for frictionless cases, while the VDF for frictional cases are exponential-like [161]. We scale VDF $f(v_\alpha)$ as $f(v_\alpha) = v_{\alpha 0}^{-1}\tilde{f}(c_\alpha)$ with $\int dc_\alpha \tilde{f}(c_\alpha) = \int dc_\alpha c_\alpha^2 \tilde{f}(c_\alpha) = 1$, $\int dc_\alpha c_\alpha \tilde{f}(c_\alpha) = 0$ and $v_{\alpha 0} \equiv \sqrt{2T_\alpha/m}$ for each α. Scaled VDF for each velocity components are shown in Fig. 5.8, where all of the VDFs are near to Gaussian $\tilde{f}(c_\alpha) = \exp(-c_\alpha^2/2)/\sqrt{2\pi}$ even for the frictional case, because friction constant $\mu = 0.2$ is sufficiently small, and are far from exponential-like VDF $\tilde{f}(c_\alpha) = \exp(-\sqrt{2}|c_\alpha|)/\sqrt{2}$. The flatness, which is defined as $\langle x^4\rangle/\langle x^2\rangle^2 = \langle x^4\rangle$ for $\langle x^2\rangle = 1$ with $\langle \cdots \rangle \equiv \int dx \tilde{f}(x) \cdots$, is summarized in

Table 5.1: Flatness for the frictionless and the frictional case.

	z	r	θ
frictionless case	2.87	2.86	3.41
frictional case	2.70	2.98	3.71

Table 5.1 for $\tilde{\phi}_0 = 0.90$. It should be noted that the flatness with Gaussian VDF is 3.0 and that with exponential VDF is 6.0. Although the flatness with θ component of VDF slightly deviates from 3.0, it is still far from 6.0, and thus, the effect of Coulombic slip with friction constant $\mu_p = 0.2$ is not significant.

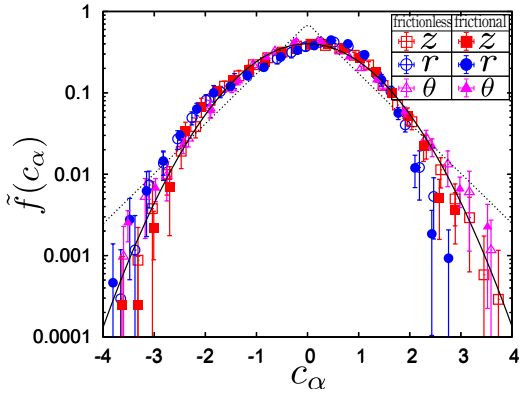

Figure 5.8: Scaled VDF $\tilde{f}(c_\alpha)$ for $\tilde{\phi}_0 = 0.90$. Empty points and filled points denote the frictionless case and the frictional case, respectively. The black solid line is $\tilde{f}(c_\alpha) = \exp(-c_\alpha^2/2)/\sqrt{2\pi}$ and the dashed line is $\tilde{f}(c_\alpha) = \exp(-\sqrt{2}|c_\alpha|)/\sqrt{2}$.

The second reason is the small Coulombic constant. In this case, renormalization of restitution coefficient is known to be valid [63, 64, 67]. We stress here that the residual stress for the frictional granular fluid with small Coulombic constant does not exist in a usual setup. We also note that there exists no characteristic feature of Coulombic friction for small μ_p such as $\mu_p = 0.2$ except for the decreases of the jamming density even for the jamming transition [163].

Moreover, once we assume that shear viscosity corresponds to the value from kinetic theory $\eta(r) = \eta_{\rm kin}(\phi, T_g)$, the extrapolated σ_Y are obtained at each mesh, through $\sigma_{rz}(r) = \sigma_Y(r) - \eta_{\rm kin}(\phi(r), T_g(r))D_{rz}(r)$. As a result, $|\sigma_Y|$ is sufficiently small for $r/R_{\rm tar} > 0.40$ (Table 5.2).

Thus, $\sigma_Y = 0$ is a self consistent assumption if kinetic theory is adopted. From these reasons, we assume $\sigma_Y = 0$.

Shear Viscosity

Now, let us try to compare the theoretical expression in Eq. (5.5) with the numerical measured shear viscosity. The comparison of η^*, which is the non-dimensional shear viscosity introduced in Eq. (5.5), for $0.2 < r/R_{\rm tar} < 1.0$

Table 5.2: Extrapolated yield stress $-\sigma_Y \times 10^3$.

$\tilde{\phi}_0$ \ $r/R_{\rm tar}$	0.30	0.50	0.70	0.90
0.30	6.41 ± 3.3	0.701 ± 1.5	0.434 ± 0.66	0.447 ± 0.26
0.40	7.54 ± 5.8	-0.159 ± 3.2	0.538 ± 1.1	0.364 ± 0.52
0.45	8.79 ± 2.3	0.800 ± 2.1	0.440 ± 0.94	0.783 ± 0.44
0.50	6.79 ± 2.8	-0.574 ± 1.9	0.632 ± 0.94	0.608 ± 0.32
0.80	7.00 ± 4.8	2.19 ± 1.7	-0.953 ± 1.3	0.392 ± 0.50
0.90	5.21 ± 2.7	-0.540 ± 2.9	-0.396 ± 1.2	0.243 ± 0.83

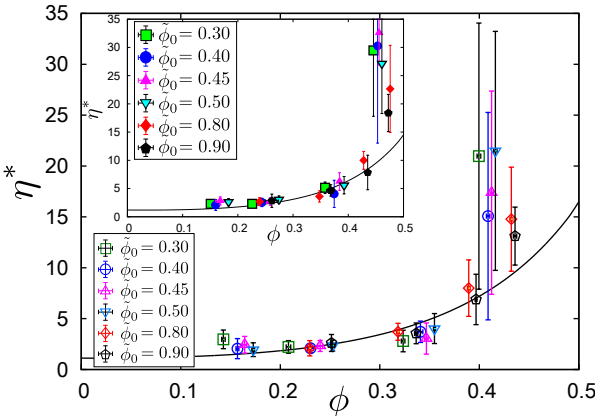

Figure 5.9: Non-dimensional shear viscosity η^*, which is defined in Eq. (5.5), for several $\phi_0/\phi_{\rm fcc}$ in $0.2R_{\rm tar} < r < R_{\rm tar}$. Black solid lines denote theoretical curves.

is shown in Fig. 5.9. Although there is a slight deviation between them for large ϕ i.e. small r, which may be the effect of the singularity in the center $r = 0$, the theoretical curve reproduces other numerical results. We can, thus, conclude that the flow has the finite shear viscosity which has the same order of the predicted value by kinetic theory. The reason why the simulations are approximately described by the Euler equation is that the strain rate itself is small i.e. $0.01 < D_{rz}d/\sqrt{T_g/m} < 0.4$, and thus σ_{rz}/σ_{zz} is small.

Shear viscosity on μ^* vs I plane

From the analysis on μ^* vs I plane, the constitutive equations can be obtained as

$$\sigma_{rz} = -\eta D_{rz} \tag{5.12}$$

$$\eta^*_\mu = \frac{16a}{5}\sqrt{6\phi(1+2\phi(1+e)\chi)}. \tag{5.13}$$

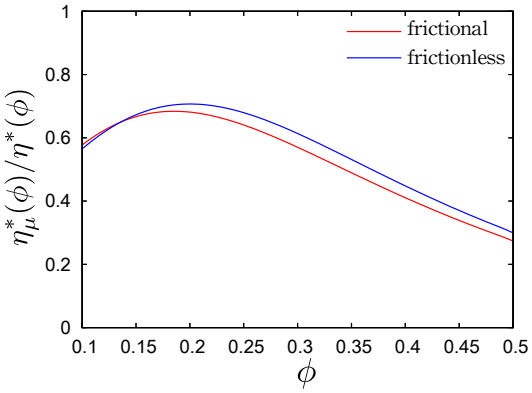

Figure 5.10: Comparison of the non-dimensional shear viscosity based on the kinetic theory $\eta^*(\phi)$ [52] with our result, where the solid line and the dashed line denotes for the frictional case and the frictionless case, respectively.

Here, non-dimensional shear viscosity $\eta_\mu^* = \eta_\mu^*(\phi)$ on μ^* vs I plane is introduced as $\eta_\mu^* \equiv \eta/\eta_0$ with the shear viscosity η and $\eta_0 \equiv 5\sqrt{\pi m T_g}/16d^2$ by convention [52].

The obtained shear viscosity is proportional to $\sqrt{T_g}$, which is consistent with kinetic theoretical results [47]. However, the obtained density dependence of η_μ^* is different from ref. [52]. The non-dimensional shear viscosity based on the kinetic theory $\eta^*(\phi)$ is compared with our result in Fig. 5.10. The solid line and the dashed line denotes for the frictional case and the frictionless case, respectively. The obtained shear viscosity is less than 80% of that of the kinetic theory. It should be noted that the obtained shear viscosity is also finite, even through the analysis based on the effective friction coefficient.

The difference of density dependence of non-dimensional shear viscosity would be understood in the followings. In the analysis on μ^* vs I plane, the density dependence of transport coefficient is assumed to appear only through pressure P, i.e.

$$\eta(P, T_g, \phi) = \eta(P(\phi, T_g)). \tag{5.14}$$

Thus, once the equation of state is determined, $\eta_\mu^*(\phi)$ is uniquely obtained. On the other hand, in ref. [52], because density dependence of η^* results from the kinetic theory, results are different. At present, we could not judge which viscosity is better. However, we should note that the $\eta \propto \sqrt{T_g}$ can be obtained, even under the assumption of Eq. (5.14) [48].

5.4 Is granular flow really a “perfect fluid?”

We have numerically investigated the granular jet which impacts on a fixed wall. We have revealed that the granular flow after the impact has a finite shear viscosity which has the same order as the predicted value from kinetic

theory, and thus the similarity between the granular flow and the perfect fluid is superficial, which comes from a small strain rate. This result gives a theoretical explanation of the similarity between granular flow and perfect fluid, which is reported in the experiment and the two-dimensional study [31, 38] Although both the pressure and the viscosity are not far from the predictions by kinetic theory, there exists a large normal stress difference in contrast to the case of kinetic theory.

Chapter 6

Rheology of Granular Jets in Two Dimensions: Jet-induced jamming

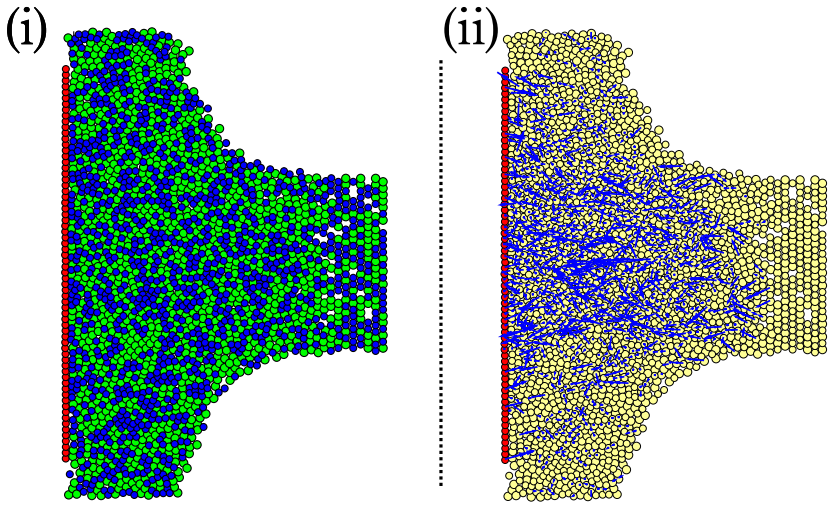

Figure 6.1: (i) A typical snapshot of the simulation for the frictional case with $\tilde{\phi}_0 = 0.90$. Blue particles and green particles denote grains with diameter $0.8d$ and d, respectively and red particles are wall-particles. (ii) All of the corresponding contact forces between grains are visualized as blue colored arrows.

In this chapter, we investigate the rheology of the granular jets in two dimensions. We evaluate physical quantities near the wall in two regions: $0 < x \leq 5d$ and $5d < x \leq 10d$, where we call (a) and (b) layers in the followings, respec-

tively. We use $R_{\rm jet}/d = 15.0$ and $R_{\rm tar}/R_{\rm jet} = 2.2$ with the target radius $R_{\rm tar}$ and the jet radius $R_{\rm jet}$. We adopt the Cartesian coordinate, where $y = 0$ is chosen to be the jet axis, and divide calculation region into the y direction $y = -5\Delta y, -4\Delta y, \cdots, 0, \cdots, 5\Delta y$, with $\Delta y \equiv R_{\rm tar}/5$. Then we estimate physical quantities in the corresponding mesh region with $k\Delta y < y < (k+1)\Delta y$ $(k = -5, -4, \cdots, 4)$. Numerical data are averaged over ten initial configurations with the same $\tilde{\phi}_0$ and error bars in figures denote their difference.

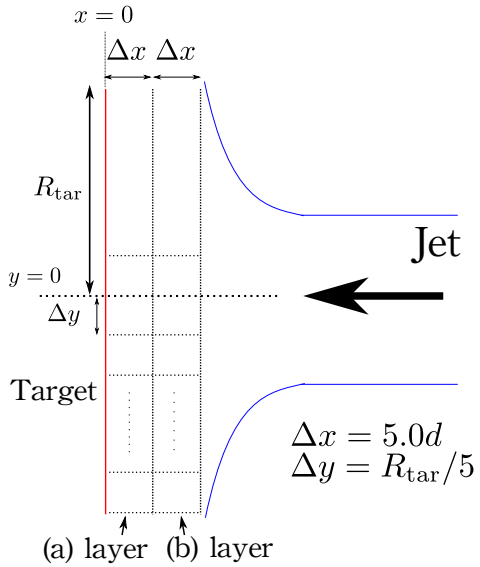

Figure 6.2: A schematic picture of the calculation region. We evaluate physical quantities near the wall in (a) layer $0 < x \leq 5d$ and (b) layer $5d < x \leq 10d$.

We use $k_n = 1.99 \times 10^3 m u_0^2/d^2, \eta_n = 5.75 u_0/d$ for $\mu_p = 0.4$, and $k_n = 7.96 \times 10^2 m u_0^2/d^2, \eta_n = 10.15 u_0/d$ for $\mu_p = 1.0$. As for $\mu_p = 0.2$ or frictionless case, we adopt k_n and η_n in Table 4.1. This set of parameters implies that the duration time is $t_c = 0.10 d/u_0$ for frictionless case and $\mu_p = 0.2$, $t_c = 0.05 d/u_0$ for $\mu_p = 0.4$ and $t_c = 0.01 d/u_0$ for $\mu_p = 1.0$, the restitution coefficient for normal impact is unchanged $e = 0.75$ for the frictionless or all μ_p cases. If we use the same t_c for large μ_p, because of the existence of many overlaps between grains, an artificial burst-like flow emerges, as is shown in the Appendix E, which is suppressed as t_c becomes smaller.

A typical snapshot of simulation and that of the contact force for the frictionless case are shown in Fig. 6.1 (i) and (ii), respectively. Blue and green particles and red particles denote grains with diameter $0.8d$ and d, and wall-particles, respectively in Fig. 6.1 (i) and all of the corresponding contact forces between grains are visualized as blue colored arrows in Fig. 6.1 (ii). It is easily found that the dense flow with well-developed contact forces emerges during the impact.

We calculate the stress tensor as in Appendix C. The microscopic definition of the stress tensor at $\mathbf{r}$ is given by

$$\sigma_{\mu\nu}(\mathbf{r}) = \frac{1}{A}\sum_i m u_{i\mu} u_{i\nu} + \frac{1}{A}\sum_{i<j} F_\mu^{ij} r_\nu^{ij}, \tag{6.1}$$

where i and j are indices of particles, $\mu, \nu = x, y$, contact force between i th and j th particles F_μ^{ij} and $\sum_i$ denotes the summation over the particles denoted by i located at $\mathbf{r}$. A is the are of each mesh at $\mathbf{r}$ and $u_{i\mu}(\mathbf{r}) = v_{i\mu} - \bar{v}_\mu(\mathbf{r})$ with the mean velocity $\bar{v}_\mu(\mathbf{r})$ in the mesh at $\mathbf{r}$.

6.1 Rheology of Granular Jets for the frictionless bi-disperse grains

In this section, we explain the obtained results on rheological properties of 2D granular jets for frictionless grains. There are four subsections in this section, which are the discussion on the dead zone, the profile of the stress tensor, the equation of state and the constitutive equation, respectively.

6.1.1 Existence of the dead zone and the profile of the are fraction

The existence of the dead zone near the target, where the motion of the grains is frozen, has been reported by Ellowitz *et al* [38] and Guttenberg [39]. In our 3D study, however, we confirm that there is no definite dead zone through the analysis of the granular temperature $T_g \equiv \sum_i m\mathbf{u}_i^2/DN$ in $D(=2,3)$ dimensions, while the average velocity of grains becomes small near the target [48]. On the other hand, we verify the existence of the frozen layer (a) in 2D, while the motion is not frozen in (b) layer. The comparisons of T_g in 2D and 3D for the frictionless case are shown in Fig. 6.3 (i). Although T_g slightly smaller at the center in 3D, it is still larger than those in 2D.

The profile of the area fraction divided by $\phi_{\max}$ with $\phi_{\max} \equiv \pi/(2\sqrt{3}) \simeq 0.907$ in 2D and $\phi_{\max} \equiv 0.740$ in 3D are shown in Fig. 6.3 (ii) for the frictionless case. It is apparent that the granular flow in 2D becomes denser than that in 3D.

6.1.2 Profile of the stress tensor

The profiles of the stress tensor for (a) and (b) layer of frictionless grains are shown in Fig. 6.4 (i) and (ii), respectively. We stress that there exists a large normal stress difference between σ_{xx} and σ_{yy} in each layer as in 3D case [47], which has not been reported in other papers.

Ellowitz *et al.* suggested that the profile of the velocity and the pressure for the granular jet is reproducible from the simulation of a perfect fluid [38] but our result may not support their claim. Indeed, the shear stress looks small

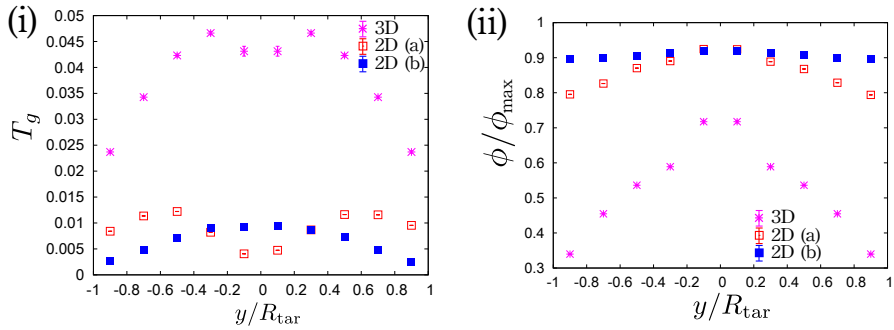

Figure 6.3: The profile of T_g for $\tilde{\phi}_0 = 0.90$ is shown in (i). There exists the dead zone in (a) layer, which is denoted by red empty squares. Blue filled squares denote T_g in (b) layer, where the dead zone does not exist. T_g in 3D, which is denoted by purple asterisks, is higher than those in 2D. The profile of $\phi/\phi_{\rm max}$ for $\tilde{\phi}_0 = 0.90$ is shown in (ii). $\phi/\phi_{\rm max}$ Grains are well packed in 2D, while they are not in 3D.

but finite. Moreover, the large normal stress difference exists in both layers, which cannot be observed in the perfect fluid. We should note that their claim is supported by the simulation of a perfect fluid which reproduces some similar feature of their hard core simulation. However, they have not discussed the stress tensor itself in their simulation. In addition, Huang *et al.* indicated the relevant role of the contact stress in their DEM simulation, which may be an indirect objection to the perfect fluidity of the 2D granular jet flow [40].

6.1.3 Equation of state

Let us discuss the equation of state for the 2D granular jet impact. We estimate strain rate $D_{xy} \equiv (\partial \bar{v}_y/\partial x + \partial \bar{v}_x/\partial y)/2$ as $\partial \bar{v}_y(\Delta x/2, y)/\partial x \simeq (\bar{v}_y(3\Delta x/4, y) - \bar{v}_y(\Delta x/4, y))/(\Delta x/2)$, $\partial \bar{v}_y(3\Delta x/2, y)/\partial x \simeq (\bar{v}_y(7\Delta x/4, y) - \bar{v}_y(5\Delta x/4, y))/(\Delta x/2)$ and $\partial \bar{v}_x(x, y)/\partial y \simeq (\bar{v}_x(x, y + \Delta y/2) - \bar{v}_x(x, y - \Delta y/2))/\Delta y$. Since we evaluate the physical quantities near the wall, the mesh $0 < x < \Delta x$ is divided into $0 < x \leq \Delta x/2$ and $\Delta x/2 < x < \Delta x$, and $\Delta x \leq x < 2\Delta x$ is divided into $\Delta x \leq x < 3\Delta x/2$ and $3\Delta x/2 \leq x < 2\Delta x$ to calculate $\partial \bar{v}_y(\Delta x/2, y)/\partial x$ and $\partial \bar{v}_y(3\Delta x/2, y)/\partial x$. $-R_{\rm tar} < y < R_{\rm tar}$ is divided into $-11\Delta y/2 < y < -9\Delta y/2, -9\Delta y/2 < y < -7\Delta y/2, \cdots 9\Delta y/2 < y < 11\Delta y/2$ to calculate $\partial \bar{v}_x(x, y)/\partial y$.

We follow the analysis in ref. [131]. Here, we introduce two dimensionless numbers consisting of pressure: $I_T \equiv \sqrt{T_g/Pd^2}$ and $I_s \equiv D_{xy}\sqrt{m/P}$ with pressure $P \equiv (\sigma_{xx} + \sigma_{yy})/2$. We plot numerical data on ϕ vs I_T plane and ϕ vs I_s plane, in Fig. 6.5 (i) and (ii), respectively.

We can fit the data by the equations

$$\phi = \phi_T - a_T I_T^{2/\alpha_T} \tag{6.2}$$

$$\phi = \phi_s - a_s I_s^{2/\alpha_s}, \tag{6.3}$$

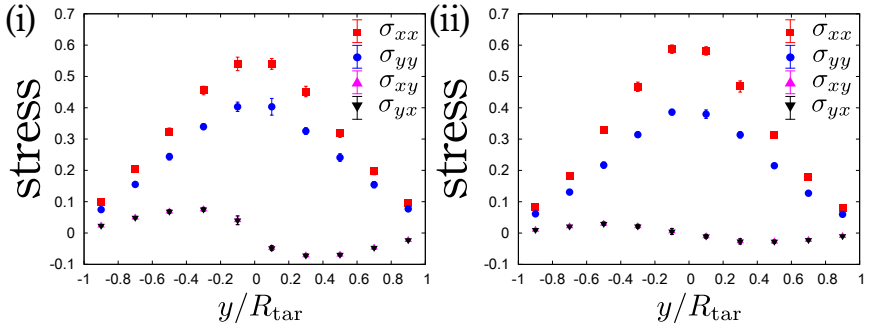

Figure 6.4: The profile of the stress tensor for $\tilde{\phi}_0 = 0.90$ in (a) and (b) layer is shown in (i) and (ii), respectively. There exist large normal stress differences between σ_{xx} and σ_{yy} and the shear stress is much smaller than the normal stress in (b) layer, though it is not so small in (a) layer.

with constants $\phi_T, a_T, \alpha_T, \phi_s, a_s$ and α_s. Fitting parameters are determined simultaneously by using Levenberg-Marquardt algorithm [169]. The obtained equations of states are written as

$$\frac{Pd^2}{T_g} = \frac{a_T^{\alpha_T}}{(\phi_T - \phi)^{\alpha_T}} \tag{6.4}$$

$$\frac{P}{mD_{xy}^2} = \frac{a_s^{\alpha_s}}{(\phi_s - \phi)^{\alpha_s}}, \tag{6.5}$$

where the comparison of Eqs. (6.2) and (6.3)with numerical data for the frictionless case are shown in Fig. 6.5 (i) and (ii), respectively.

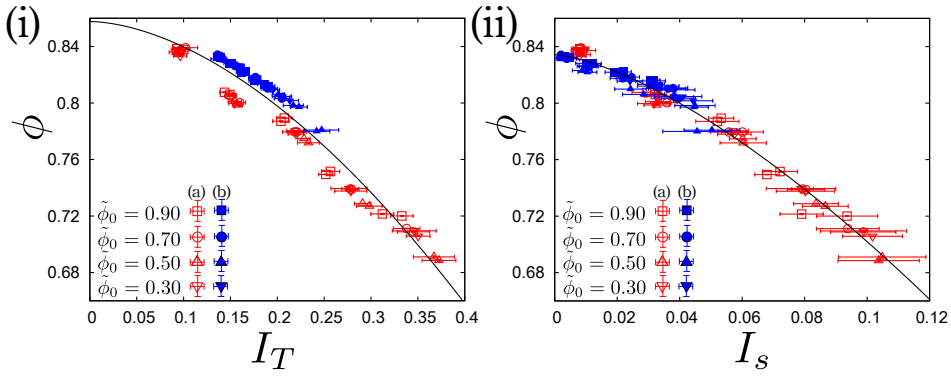

Figure 6.5: Numerical data for the bi-disperse case of frictionless grains are plotted on ϕ vs I_T plane (i) and ϕ vs I_s plane (ii). Red empty and blue filled points denote data of (a) and (b) layer for several $\tilde{\phi}_0$, respectively. The corresponding solid lines in figures are fitting equations (6.2) and (6.3).

Obtained parameters are $\phi_T = 0.858 \pm 0.006, a_T = 0.980 \pm 0.1, \alpha_T = 1.15 \pm 0.1, \phi_s = 0.834 \pm 0.001, a_s = 3.94 \pm 0.5$ and $\alpha_s = 1.36 \pm 0.05$, where error originates from the fitting (Fig, 6.5 (i)(ii)). Note that the conventional jamming point $\phi_J \simeq 0.8425$ is located between ϕ_s and ϕ_T and close to ϕ_s [149]. The divergences of pressure for the frictionless case are written as

$$\frac{Pd^2}{T_g} \sim (\phi_T - \phi)^{-1.15}, \quad \frac{P}{mD_{xy}^2} \sim (\phi_s - \phi)^{-1.36}. \tag{6.6}$$

Hatano demonstrated the elegant scaling law in the vicinity of ϕ_J, where the corresponding exponents are estimated as $\alpha_s = 2.8$ and $\alpha_T = 1.7$ from his data [146]. Otsuki and Hayakawa showed the phenomenological explanation of the critical behavior near ϕ_J and they predicted $\alpha_s = 4.0$ and $\alpha_T = 2.0$ [142, 145]. Our obtained exponents are smaller than conventional ones. The discrepancy between these may result from difference of the setups. Because the strain rate cannot be controlled in our setup, the jamming point is not clearly defined. Therefore, the divergence of the pressure is duller than the case of the usual jamming. We note that the exponents for the conventional jamming strongly depends on the choice of ϕ_J [145].

On the other hand, by extrapolating the critical behavior from the kinetic regime, the pressure behaves as $\alpha_T = 1.0$ i.e.

$$\frac{Pd^2}{T_g} - 1 = \phi g(\phi) \propto \frac{\phi_c}{\phi_c - \phi} \tag{6.7}$$

as $\phi \to \phi_c$, with radial distribution function $g(\phi)$ and critical density ϕ_c, while $\alpha_T > 1$ for the jamming [142, 145, 146]. In our case, the data may satisfy $Pd^2/T_g \sim (\phi_c - \phi)^{-1}$. Thus, the divergence of Pd^2/T_g is similar to the extrapolation from the kinetic theoretical regime, rather than the jamming. We note that one of the obtained diverging densities is larger than conventional one: $\phi_T > \phi_J$. Although α_T is close to the kinetic theoretical result, the analysis of α_T and ϕ_T may not be reliable, because the data for (a) and (b) layer are separate, due to the difference of the profile of T_g. The separation of data in (a) and (b) layer is discussed in Sec. 6.2.

From Eqs. (6.4) and (6.5), T_g and D_{xy} are expected to satisfy

$$\frac{md^2 D_{xy}^2}{T_g} = \frac{a_T^{\alpha_T}(\phi_s - \phi)^{\alpha_s}}{a_s^{\alpha_s}(\phi_T - \phi)^{\alpha_T}}. \tag{6.8}$$

The validity of Eq. (6.8) is verified in Fig. 6.6 for the frictionless case, which can be independent check of the scaling laws (6.4) and (6.5). From Fig. 6.6, Eq. (6.8) well reproduces the data for $\phi < \phi_s$. We note that the proportional relation between $T_g \propto md^2 D_{xy}$ as in Eq. (6.8) can be found in the context of the Bagnold scaling [113].

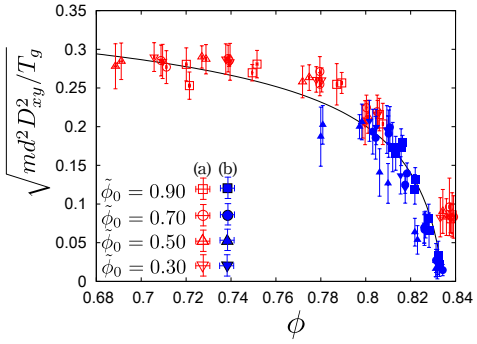

Figure 6.6: Comparison of the numerical data for $\sqrt{md^2D_{xy}/T_g}$ with Eq. (6.8) are compared for $\phi < \phi_s$.

6.1.4 Constitutive relation

Effective friction constant

We discuss I_s dependence of effective friction constant $\mu^* \equiv -\sigma_{xy}/P$ to obtain the constitutive equation. Numerical data for the frictionless case and the frictional case are shown in Fig. 6.7 (i) and (ii), respectively. The behavior of μ^* is conventionally described as

$$\mu^*(I_s) = \mu_s + (\mu_{\max} - \mu_s)(1 + I_0/I_s), \tag{6.9}$$

where μ^* starts from a critical value of μ_s at zero shear rate and converges to a limiting value of $\mu_{\max}$ at high I_s. We obtain $\mu_s = 0.0153 \pm 0.009, \mu_{\max} = 0.521 \pm 0.06$ and $I_0 = 0.0820 \pm 0.02$ for the frictionless case by fitting. Thus, $\mu^*(I_s)$ can be fitted by the conventional relation (6.9). We should stress that μ_s is close to zero.

Some researchers proposed a different constitutive equation

$$\mu = \mu_s + bI_s^\beta, \tag{6.10}$$

which also well reproduces numerical data [126, 129, 131–134], where β ranges from $0.28 \sim 1.0$, depending on the dimension, microscopic parameters and the friction constant of grains. We can fit it into numerical data within error bars, where we obtain $b = 1.18 \pm 0.1$ and $\beta = 0.592 \pm 0.03$, assuming $\mu_s = 0$. The constitutive equation can be described as

$$\frac{\sigma_{xy}}{mD_{xy}^2} = -\frac{ba_s^{(1-\beta/2)\alpha_s}}{(\phi_s - \phi)^{(1-\beta/2)\alpha_s}}, \tag{6.11}$$

which is checked independently against the numerical data in Fig. 6.8. Exponents are estimated as $(1 - \beta/2)\alpha_s \simeq 0.96$. Because, we use the power-law friction $\beta > 0$, the divergences of shear stress are weaker than those of P. Here, because the shear stress is proportional to the square of the shear rate, the Bagnold scaling is valid in our setup.

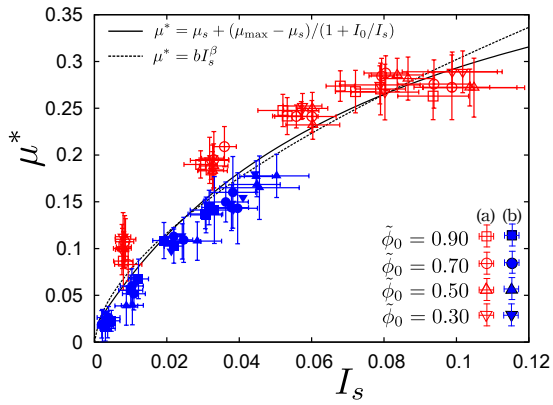

Figure 6.7: Numerical data for the bi-disperse case of frictionless grains are plotted on μ^* vs I_s plane. Red and blue points denote data for (a) and (b) layer for several $\tilde{\phi}_0$, respectively. All points are fitted into Eq. (6.9) proposed phenomenologically in Ref. [127] and the Eq. (6.10) for power-law friction, where we cannot judge which equation is better from the data.

Shear viscosity

Here, let us discuss the divergence of the shear viscosity. We define shear viscosity $\eta \equiv -\sigma_{xy}/D_{xy}$ and non-dimensional shear viscosity $\eta^* \equiv \eta/\eta_0$ with $\eta_0 \equiv \sqrt{mT_g/4\pi d^2}$ and

$$\eta^* \propto (\phi_s - \phi)^{-\beta_s}. \tag{6.12}$$

By using the result from the power-law friction in Eq. (6.11), η^* diverges as

$$\eta^* = \frac{-\sigma_{xy}}{D_{xy}\eta_0} \propto (\phi_T - \phi)^{-(1-\beta/2)\alpha_T} \left(\frac{md^2 D_{xy}^2}{T_g}\right)^{-(1-\beta/2)\alpha_T} \propto (\phi_s - \phi)^{-(1-\beta/2)\alpha_s}, \tag{6.13}$$

where we have used Eq. (6.8) and (6.11). η^* diverges at ϕ_s, which is different from the divergence of Pd^2/T_g, with exponent $\beta_s = (1-\beta/2)\alpha_s \simeq 0.96$.

For the conventional jamming transitions of frictionless grains, the exponents for the divergence of η^* are estimated to be 1.95 from data in Ref. [146] and 3.0 in Ref. [142]. Thus, our corresponding exponent $\beta_s = 0.96$ is much smaller than conventional ones, rather close to the prediction that η^* diverges at density different from Pd^2/T_g with the exponent $\beta_s = 1.0$, which is the result of the extrapolation from kinetic theoretical regime by Garcia-Rojo [147].

Let us summarize the results for the frictionless case. There exists the dead zone, at least, in (a) layer, though it does not exist in (b) layer. The shear stress is much smaller than normal stress, at least in (b) layer. Because grains are easily packed after the impact, the system is near the jammed state, while diverging exponents are smaller than conventional ones. Although, the data in (a) and (b) layer are separate on ϕ vs I_T plane, due to the coexistence of the

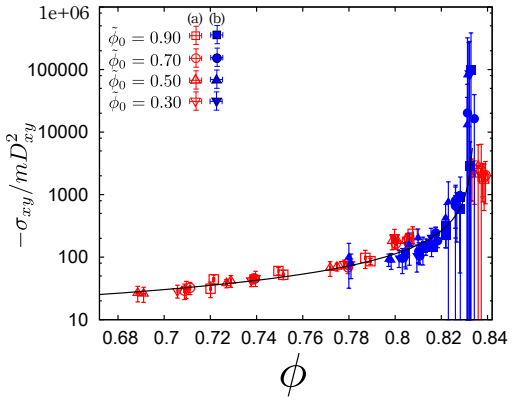

Figure 6.8: The divergences of the shear stress and Eq. (6.11) are independently checked for the bi-disperse case of frictionless grains. Red and blue points denote data for (a) and (b) layer for several $\tilde{\phi}_0$, respectively. Eq. (6.11) well reproduces numerical results. Because σ_{xy} itself in (b) layer are small, the error bars in (b) layer are larger than those in (a) layer.

frozen layer and non-frozen layer, Pd^2/T_g diverges at ϕ_T with the exponent close to the extrapolation from the kinetic theoretical regime. As for the analysis on ϕ vs I_s plane, the conventional diverging density ϕ_J is located between ϕ_s and ϕ_T and close to ϕ_s, and the corresponding exponent α_s is smaller than conventional one. We can use both of Eqs. (6.9) and (6.10) for μ^*. If we adopt the power-law friction, non-dimensional shear viscosity η^* diverges, similar to the prediction by Garcia-Rojo [147].

6.2 Effects of the friction constant

In this section, we discuss the effects of the friction constant on the jet-induced jamming. There are four subsections in this section, which are the discussion on the dead zone, the profile of the stress tensor, the divergence of the pressure and the friction law, respectively.

6.2.1 Existence of the dead zone and the profile of the are fraction for the frictional case

We show the profile of T_g and ϕ in Fig. 6.9 (i) and (ii), respectively. Red empty points denote the data in (a) layer, and blue filled ones denote those in (b) layer. In Fig. 6.9 (i), numerical data for T_g in (a) layer drop at the center, i.e. the motion of grains is frozen, while those in (b) layer do not. The existence of the dead zone in (a) layer and its absence in (b) layer are confirmed even for the frictional case. Thus, the frozen layer (a) and the non-frozen layer (b) coexist even for the frictional cases. ϕ decreases, as μ_p becomes larger.

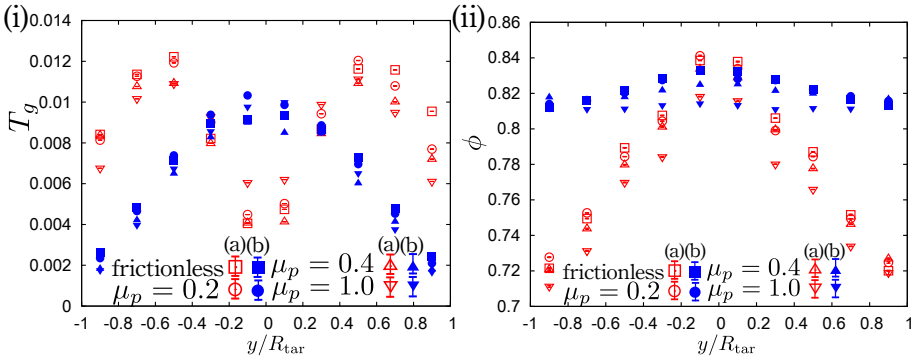

Figure 6.9: The profile of T_g and ϕ are shown in (i) and (ii), respectively. The existence of the dead zone in (a) layer and its absence in (b) layer are confirmed even for the frictional case. ϕ decreases, as μ_p becomes larger.

6.2.2 Profile of the stress tensor

The profiles of the stress tensor for (a) and (b) layer are shown in Fig. 6.10 (i)(ii) for $\mu_p = 0.2$, (iii)(iv) for $\mu_p = 0.4$ and (v)(vi) for $\mu_p = 1.0$. Regardless of the friction constant μ_p, the shear stress is much smaller than the normal stress in (b) layer, though it is not so small in (a) layer. We stress that the profile of $\sigma_{\mu\nu}$ is not much affected by μ_p and that there exists a large normal stress difference between σ_{xx} and σ_{yy} in each layer.

6.2.3 Divergence of the pressure

Let us discuss the effect of μ_p on the divergence of the pressure. We obtain the diverging density ϕ_T and ϕ_s and the corresponding exponents α_T and α_s for (a) and (b) layer separately, via fitting numerical data into Eqs. (6.2) and (6.3), respectively. The results for the fitting are shown in Fig. 6.11 (i)(ii) for the frictionless case, (iii)(iv) for $\mu_p = 0.2$, (v)(vi) for $\mu_p = 0.4$ and (vii)(viii) for $\mu_p = 1.0$. The effect of μ_p would be apparent as the separation of data between (a) and (b) layer not only on ϕ vs I_T plane, but also ϕ vs I_s plane, which reflects the coexistence of the frozen layer (a) and the non-frozen layer (b).

The changes in our diverging densities ϕ_s and ϕ_T for each layer are shown in Fig. 6.12 (i). For comparison, we show one of the jamming points ϕ_L in Ref. [137]. ϕ_s slightly decreases as the value of μ_p increases, while ϕ_T shows different tendency between (a) and (b) layer. ϕ_T for $\mu_p = 1.0$ may be unphysical, because the interpolation into $I_T \to 0$ is unreliable. Although the qualitative behavior of ϕ_s in (a) and (b) layer is similar to ϕ_L, we note that the decrease of our critical densities ϕ_s is a little gentler than that of ϕ_L. The results for exponents are shown in Fig. 6.12 (ii), where both exponents in (a) layer increases as μ_p increases, while they decrease in (b) layer.

6.2.4 Friction law

The results for the friction laws Eqs. (6.9) and (6.10) are shown in Fig. 6.13 (i) for $\mu_p = 0.2$, (ii) for $\mu_p = 0.4$ and (iii) for $\mu_p = 1.0$, where numerical data can be fitted by both Eqs. (6.9) and (6.10). We stress that the μ^* monotonically increases from near zero, as the increment of I_s, even for the large μ_p case. Assuming $\mu_s = 0$, we obtain the exponents β of Eq. (6.10) for frictional cases, which are insensitive to μ_p. The results for β, μ_0 and $\mu_{\max}$ are shown in Fig. 6.14.

Let us summarize the roles of the friction μ_p in the granular jet impacts in 2D. The profile of the stress tensor, the existence of the dead zone in (a) layer and its absence in (b) layer, and the friction law are insensitive to μ_p, at least $\mu_p \leq 1.0$. One of the critical densities ϕ_s decreases gentler than conventional one ϕ_L, while some of ϕ_s in (a) or (b) layer are close to ϕ_L. The data (a) and (b) layer deviate from each other on ϕ vs I_T and ϕ vs I_s plane, as μ_p becomes larger. Although interpolation on ϕ vs I_T plane is unreliable, both exponents α_T and α_s increases (decreases) as the increment of μ_p in (a) layer ((b) layer).

6.3 Rheology of Granular Jets for the mono-disperse grains

Here, we discuss the impact of granular jets in 2D for the mono-disperse case. A typical snapshot zoomed near the target is shown in Fig. 6.15, where grains are crystalized near the wall. The black solid lines in Fig. 6.15 (i) are drawn by hand to clarify the grain boundary between the crystallized region and the disordered region, where the boundary becomes a slip line. We also visualize all of the corresponding contact forces in Fig. 6.15 (ii).

6.3.1 Profile of the stress tensor

The profiles of the stress tensor are shown in Fig. 6.16. In contrast to the bi-disperse systems, because of the crystalized regions, the shear stress is not small for mono-dispersed systems, even in (b) layer. Because the system is crystalized in (a) layer, σ_{xx} or σ_{yy} might be flat at the center.

6.3.2 Divergence of the pressure

Here, we discuss the divergence of the pressure. Fitting results for Eqs. (6.2) and (6.3) are shown in Fig. 6.17 for the frictionless case (i)(ii), $\mu_p = 0.2$ case (iii)(iv), $\mu_p = 0.4$ (v)(vi) and $\mu_p = 1.0$ (vii)(viii), where the fitting might be inappropriate as μ_p become larger and the critical behavior of Pd^2/T_g and P/mD_{xy}^2 would be questionable, because obtained critical area fractions exceed the maximum packing $\phi_{\max} \simeq 0.907$. The obtained critical fractions and exponents for the frictionless case are $\phi_T = 0.936 \pm 0.006, \alpha_T = 2.06 \pm 0.1, \phi_s = 0.904 \pm 0.003, \alpha_s = 3.28 \pm 0.2$ for (a) layer and $\phi_T = 0.975 \pm 0.01, \alpha_T = 0.975 \pm 0.01, \phi_s = 0.984 \pm$

$0.03, \alpha_s = 6.86 \pm 2$ for (b) layer. Due to the crystallization, exponents α_s are larger than those for the corresponding bi-disperse case. Because there exists the crystalized region in (a) layer, one of the critical fractions ϕ_s for the frictionless case is close to the area fraction for a triangular crystal $\phi_{\max} \simeq 0.907$, while other critical fractions exceeds $\phi_{\max}$. It is apparent that the data for (a) and (b) layer are separated each other, due to the coexistence of the crystalized region and disordered region, even on ϕ vs I_s plane for the frictionless case.

6.3.3 Existence of two metastable branches in Friction law

We plot $\mu^*(I_s)$ for the mono-disperse case of the frictionless case, $\mu_p = 0.2, 0.4$ and $\mu_p = 1.0$ case in Fig. 6.18 (i)(ii)(iii) and (iv), respectively. Obviously, the behavior for the mono-disperse case is different from that for the bi-disperse case. First of all, $\mu^*(I_s)$ for (a) layer and (b) layer cannot be fitted into a single curve, unlike the bi-disperse case. Judging from the snapshot (Fig. 6.15), grains, at least, in (a) layer are partially crystallized. Therefore, it is reasonable that the response of the crystallized region would be different from that in disordered regions.

The non-monotonic behavior of $\mu^*(I_s)$ in (a) layer, which are observed in both frictional and frictionless cases, can be understood as follows. Because of the crystallization, a grain is trapped in a crystallized region, at low I_s, where μ^* would increase. However, as I_s increases, the grain can escape from the crystallized region. Thus, μ^* decreases, for large I_s.

$\mu^*(I_s)$ for frictionless and frictional cases are different in (b) layer. The most remarkable difference between the frictionless and the frictional cases is the existence of peak of μ^* at a small I_s for frictionless case, while there is no such a peak for frictional case. Because a frictional grain can roll over grains, grains easily form a group. Therefore, the boundary between such groups becomes a slip line. Thus, $\mu^*(I_s)$ would be constant as I_s becomes smaller. On the other hand, because a frictionless grain cannot either roll over them nor slip, it is trapped in the crystallized region, even as I_s increases. For this reason, $\mu^*(I_s)$ for frictional and frictionless case exhibit different behavior in (b) layer. However, we should stress that there exist two metastable branches both frictionless and frictional cases.

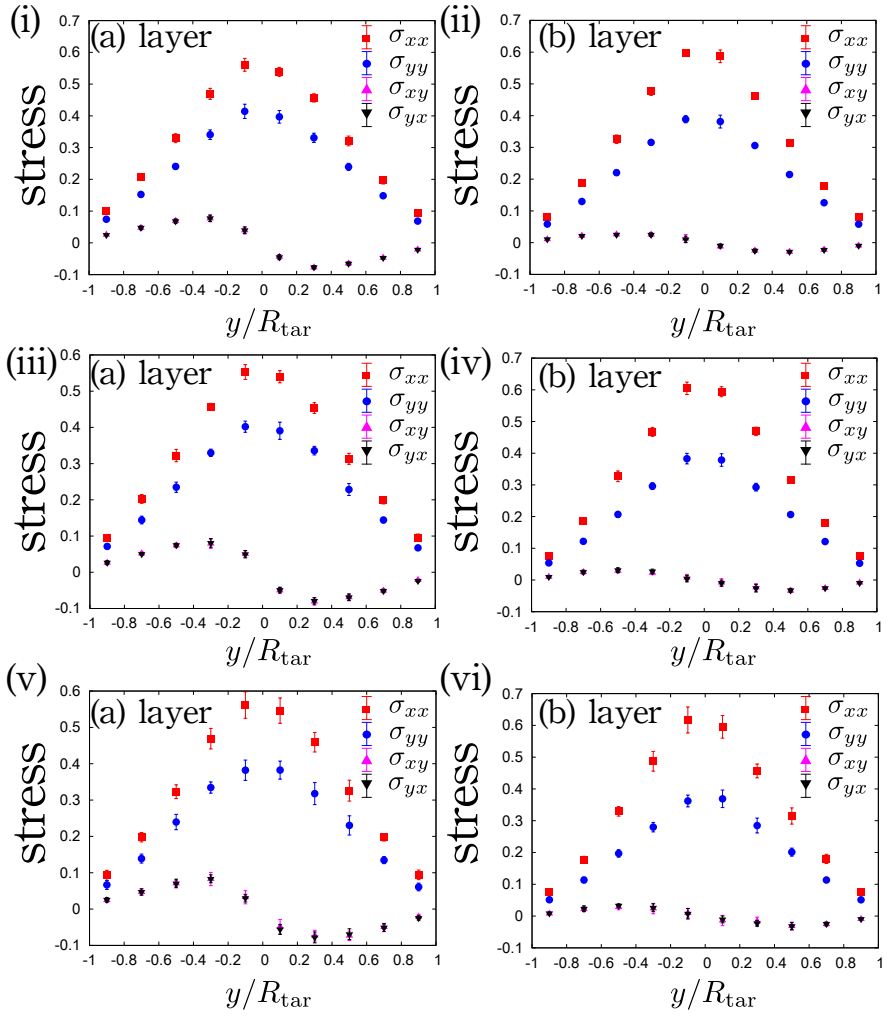

Figure 6.10: The profile of the stress tensor in the corresponding layer (a) and (b) for $\tilde{\phi}_0 = 0.90$, (i)(ii) for $\mu_p = 0.2$ case, (iii)(iv) for $\mu_p = 0.4$ case and (v)(vi) for $\mu_p = 1.0$ case. There exist large normal stress differences between σ_{xx} and σ_{yy} and the shear stress is much smaller than the normal stress in (b) layer, though it is not so small in (a) layer.

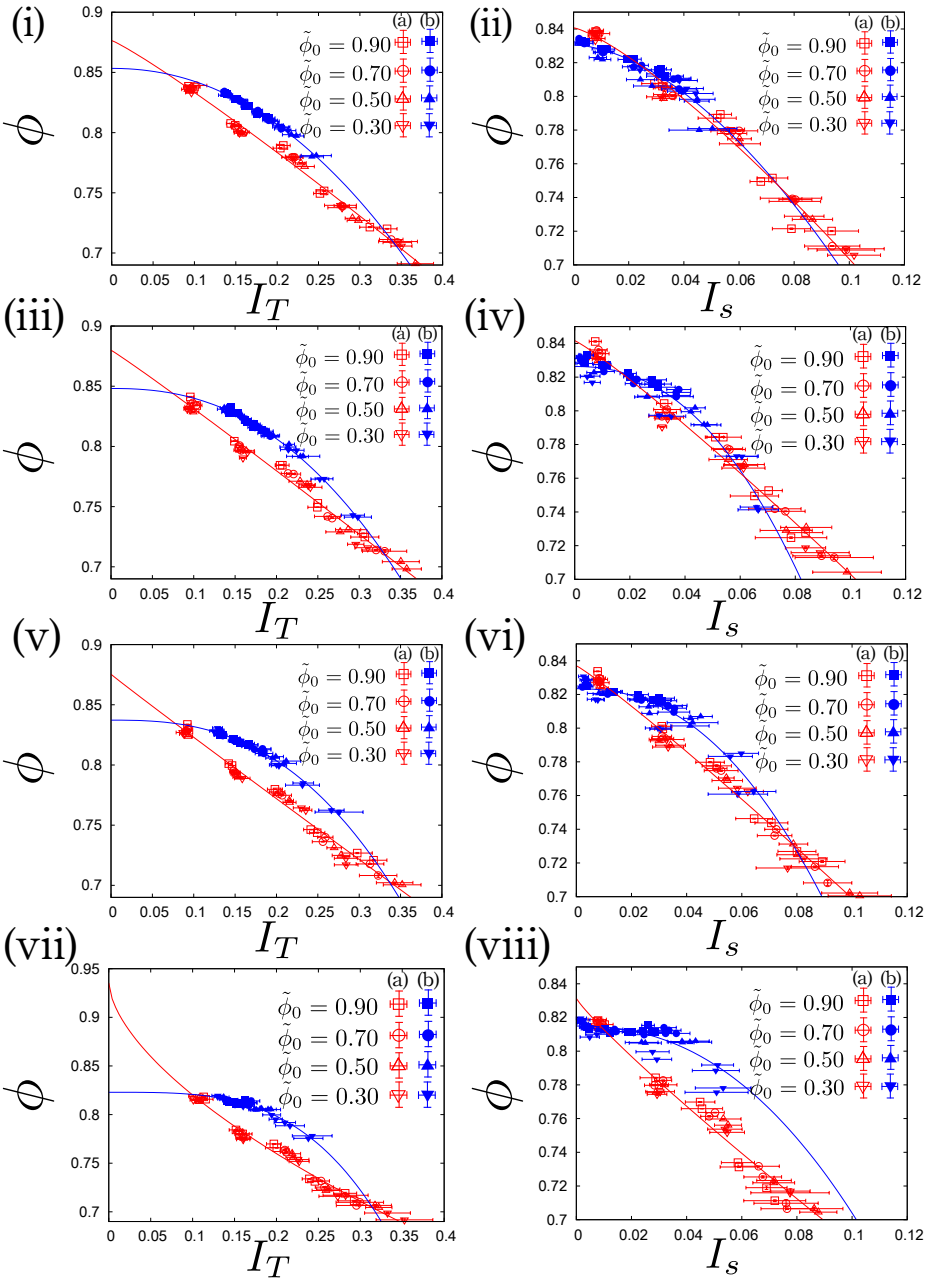

Figure 6.11: Numerical data for (a) and (b) layer are fitted into Eqs. (6.2) and (6.3) separately, for the frictionless case (i)(ii), $\mu_p = 0.2$ (iii)(iv), $\mu_p = 0.4$ (v)(vi) and $\mu_p = 1.0$ (vii)(viii). As μ_p becomes larger, data for (a) and (b) layer deviates from each other.

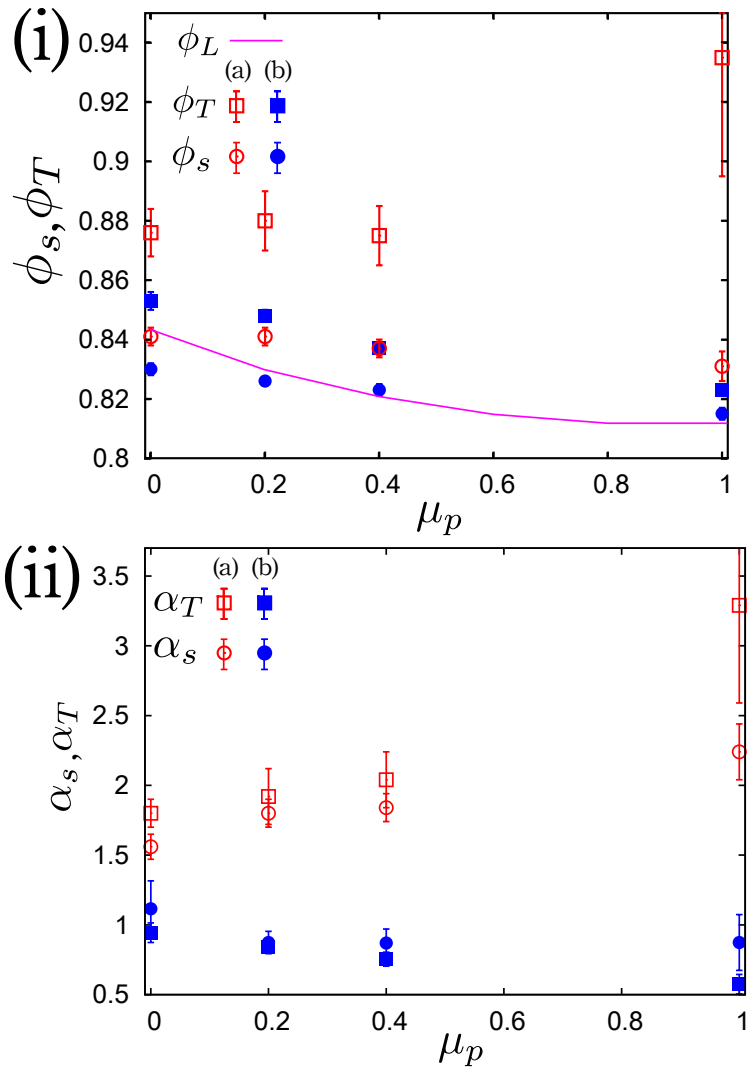

Figure 6.12: The change in ϕ_T and ϕ_s (i) and corresponding exponents α_T and α_s (ii) obtained from fitting. ϕ_s slightly decreases as μ_p increases. ϕ_T for $\mu_p = 1.0$ may be unphysical value, because the interpolation into $I_T \to 0$ is unreliable. The solid line in (i) denotes ϕ_L in [137]. Both exponents α_T and α_s increases (decreases) as the increment of μ_p in (a) layer ((b) layer).

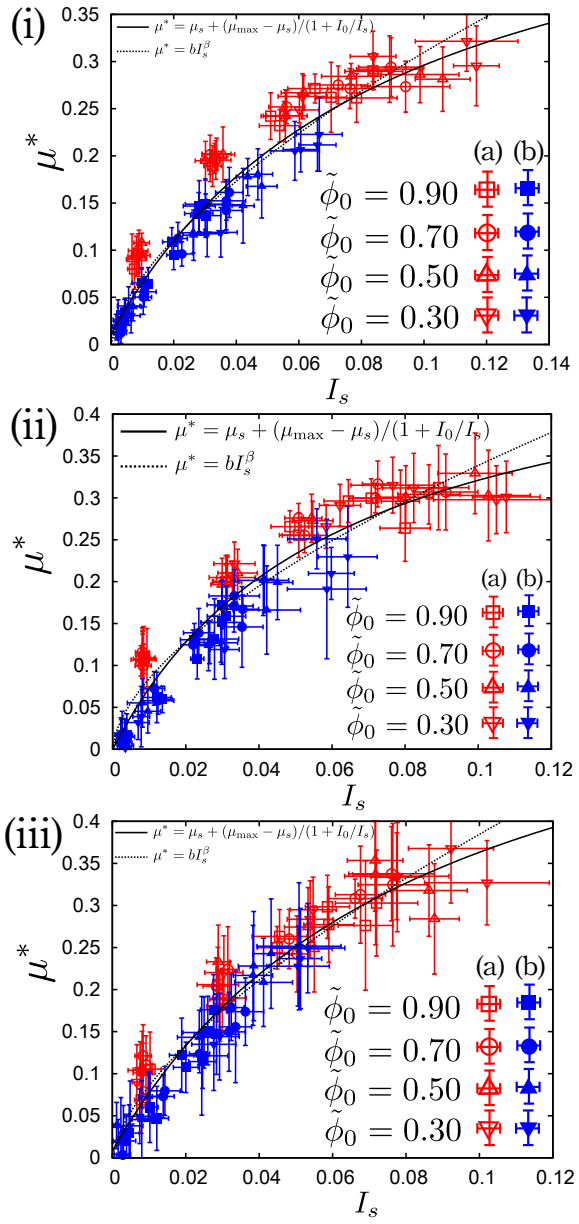

Figure 6.13: Numerical data for $\mu_p = 0.2$ (i), $\mu_p = 0.4$ (ii) and $\mu_p = 1.0$ (iii) within error bars can be fitted into Eqs. (6.9) and (6.10), where we cannot judge which equations are better. It should be noted that the μ^* monotonically increases from near zero, as the increment of I_s, even for the large μ_p case.

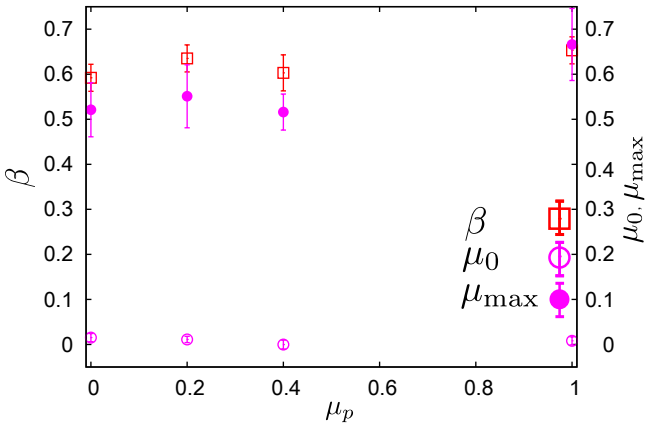

Figure 6.14: The insensitivity of β, μ_0 and $\mu_{\max}$ to μ_p. μ_0 is almost zero, even for large μ_p case.

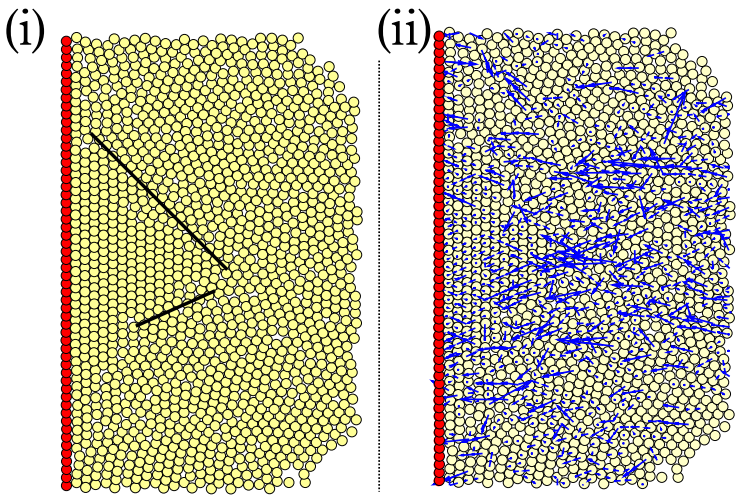

Figure 6.15: Typical snapshot of the simulation for the frictionless case with $\tilde{\phi}_0 = 0.90$ near the target. Yellow particles denote mono-disperse grains and red particles are wall-particles (i). The black solid lines are drawn by hand to clarify the grain boundary between the crystallized region and the disordered region, where the boundary becomes a slip line. Crystallization into triangular lattice can be seen near the region enclosed by the black lines. All of the corresponding contact forces between grains are visualized as blue colored arrows in (ii).

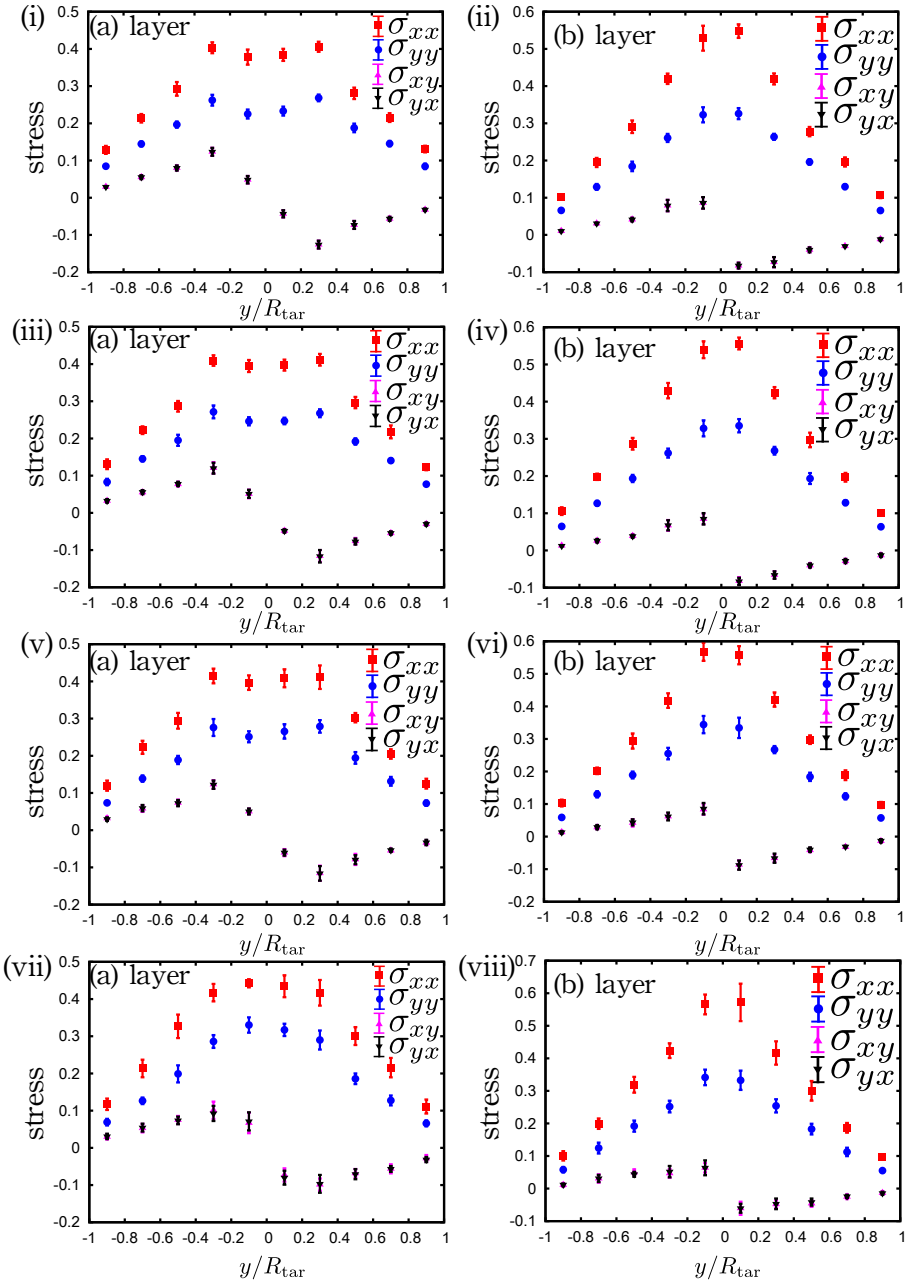

Figure 6.16: The profile of the stress tensor for the frictionless case (i)(ii), $\mu_p = 0.2$ case (iii)(iv), $\mu_p = 0.4$ (v)(vi) and $\mu_p = 1.0$ (vii)(viii), in (a) or (b) layer.

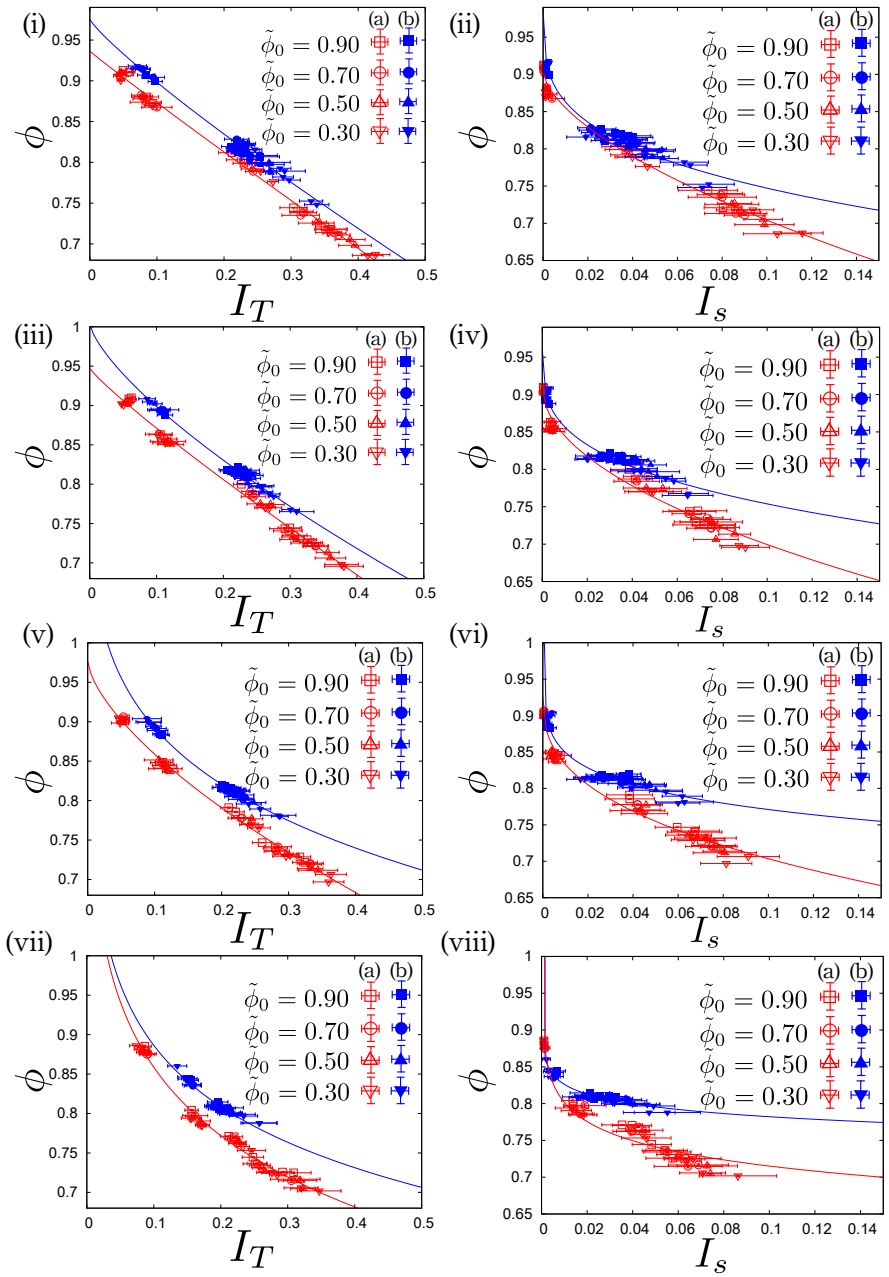

Figure 6.17: Numerical data for (a) and (b) layer are fitted into Eqs. (6.2) and (6.3) separately, for the frictionless case (i)(ii), $\mu_p = 0.2$ case (iii)(iv), $\mu_p = 0.4$ (v)(vi) and $\mu_p = 1.0$ (vii)(viii), where the fitting might be inappropriate as μ_p become larger, because obtained critical densities exceed 1.0. It is apparent that the data for (a) and (b) layer separated each other, due to the coexistence of the crystalized region and disordered region, even on ϕ vs I_s plane for the frictionless case.

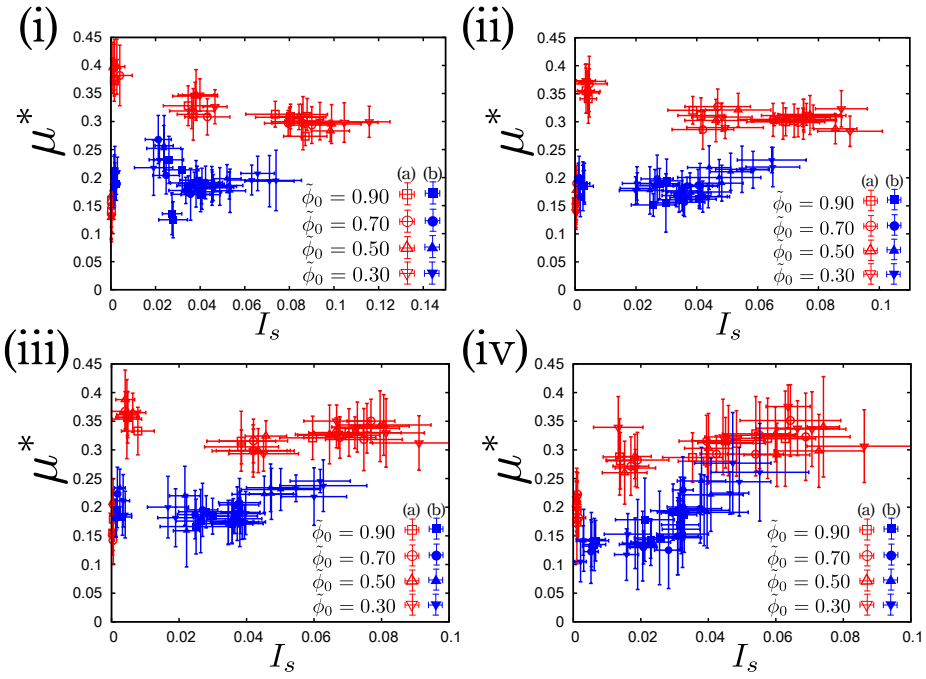

Figure 6.18: Numerical data for the frictionless case (i), $\mu_p = 0.2$ case (ii), $\mu_p = 0.4$ case and $\mu_p = 1.0$ case are plotted on μ^* vs I_s plane. Red and blue points denote data for (a) and (b) layer for several $\tilde{\phi}_0$, respectively. Unlike the bi-disperse case, $\mu^*(I_s)$ for (a) and (b) cannot be fitted into a single curve and behave non-monotonically. $\mu^*(I_s)$ for frictional and frictionless cases show similar behavior in (a) layer. However in (b) layer, because frictionless grains cannot roll over the crystallized region, $\mu^*(I_s)$ for the frictionless case shows similar dependence on I_s to that in (a) layer, while the corresponding $\mu^*(I_s)$ for frictional case dose not.

Chapter 7

Discussion and Summary

We have numerically investigated impact processes of granular jets both in 2D and 3D by using DEM, to study the fluid state after the impacts. The cone-like scattering pattern and the sheet-like pattern observed in an experiment can be reproduced through our calculation. We have found that v_2 is not proportional to the eccentricity ε in 3D. The rheology of the granular jets after the impact seem to depend on spatial dimensions.

In 3D, we have revealed that the mono-disperse granular flow after the impact has a finite shear viscosity which has the same order as the predicted value from kinetic theory. Therefore, the similarity between the granular flow and the perfect fluid, which comes from a small strain rate, is superficial [47]. This result provides a theoretical explanation of the similarity between granular flow and perfect fluid, which has been reported in an experiment and a two-dimensional study [31, 38]. We have assumed $\sigma_Y = 0$ based on the analysis on μ^* vs I plane [48]. This assumption is strong for the comparison between kinetic theory and our data. For the large-μ_p case, non-Gaussianity emerges compared with the small-μ_p case, and the validity of the renormalization of the restitution coefficient may not be valid. Results for the large Coulombic constant case will be left as the future work, including the establishment of the kinetic theory of grains with large μ_p. From the analysis on μ^* vs I plane, we also obtain the shear viscosity for the jet, whose density dependence is different from the kinetic theoretical prediction. The difference of density dependence of non-dimensional shear viscosity would result from the assumption that the density dependence for the results on μ^* vs I plane is assumed to appear only through the pressure P.

Because the small strain rate would be the consequence for the geometry of impact processes, we might expect that the shear stress is small not only for dry grains, but also grains with attractive interactions or quantum many body systems, such as the system of neutrons. Thus, the impacts of the jets composed of Lenard-Jones particles through MD simulations or those composed of neutrons through AMD [7, 8] are left as the future numerical work in 3D. Although both the pressure and the viscosity are not far from the predictions of kinetic

theory, there exists a large normal stress difference in contrast to the case of kinetic theory. Though this inconsistency may be understood through a simple phenomenology, the kinetic theory under strong non-equilibrium conditions would be necessary to construct, by introducing the anisotropic temperature T_α instead of the granular temperature T_g as hydrodynamical variables.

In 2D, because grains are easily packed, the system is near the jammed state. We confirmed the existence of the dead zone, which is reported in Ref. [38] in our study at least in (a) layer, unlike our three-dimensional case [47,48]. There exists large normal stress difference as in 3D. The shear stress is much smaller than the normal stress, at least in (b) layer. We need to solve the inconsistency in (a) layer with Ref. [38].

We have analyzed the jet-impact of frictionless bi-disperse grains. We found the divergences of the pressure and the shear viscosity, which are similar to the situation near the jamming transition, while the exponents are smaller than the conventional jamming exponents. Although, reflecting the coexistence of frozen layer and non-frozen layer, data on ϕ vs I_T plane in (a) layer and (b) layer separate, Pd^2/T_g diverges similar to the extrapolation from the kinetic theoretical regime at ϕ_T. However, data on ϕ vs I_s plane can be fitted by a single curve $P/mD_{xy}^2 \sim (\phi_s - \phi)^{-\alpha_s}$, where α_s is smaller than conventional exponent but is close to unity, and conventional ϕ_J is located between ϕ_s and ϕ_T. The effective friction constant μ^* defined as the ratio between shear stress and normal stress, monotonically increases from near zero, as the increment of the strain rate. If we adopt power-law friction for μ^*, dimensionless shear viscosity η^* diverges at $\phi_s < \phi_T$ similar to the extrapolation from the kinetic theoretical regime. The different diverging densities between Pd^2/T_g and η^* can be also found in the usual jamming [147].

The effects of the friction of grains μ_p have been discussed. The larger μ_p is, the more apparent the separation between (a) and (b) layer is, even on ϕ vs I_s plane, while the profile of the stress tensor, the friction law and the existence of the dead zone in (a) layer and its absence in (b) layers are little affected by μ_p, at least $\mu_p \leq 1.0$. One of the critical fractions ϕ_s decreases similar to the behavior of ϕ_L. Although interpolation on ϕ vs I_T plane is unreliable, both exponents α_T and α_s increases (decreases) as the increment of μ_p in (a) layer ((b) layer).

For mono-dispersed systems, grains are crystalized near the wall after the impact and several slip lines appears. In contrast to the bi- disperse systems, because the crystalized regions exist, the shear stress is not small for mono-dispersed systems, even in (b) layer. One of the critical densities ϕ_s for the frictionless case in (a) layer is close to $\phi_{\max} \simeq 0.9069$, though some of the obtained critical densities for frictional cases are larger than 1.0, where the fitting might be inappropriate and the critical behavior of Pd^2/T_g and P/mD_{xy}^2 would be questionable, as μ_p become larger. The separation of the data for (a) and (b) layer is apparent, due to the coexistence of the crystalized region and disordered region, even on ϕ vs I_s plane for the frictionless case. Unlike the bi-dispersed systems, the effective friction constants μ^* for both frictional and frictionless cases have two metastable branches for mono-disperse system

because of the coexistence of a crystallized state and a liquid state, while μ^* for the frictionless case in (b) layer is slightly different from that for frictional cases.

Because the conventional jamming transition does not depend on the spatial dimensions, the jamming induced by granular jet in 2D would be a new phenomena during impact processes. To understand the jet-induced jamming through analytical approaches, such as non-equilibrium MCT, are left as the future works.

Acknowledgement

I would like to express my deepest gratitude for Prof. Hayakawa, who is my supervisor of master course of science in Kyoto University. I am very grateful that he taught me many things about non-equilibrium physics and numerical methods. I really appreciate all the advice he gave me for writing this thesis. I also gratefully thank Prof. Sagawa, Prof. Wada, Prof. Watanabe and all present members, past members and visitors in Prof. Hayakawa's group for fruitful comments and discussions. Especially, I would like to thank my senior Mr. Kanazawa for giving me many advices not only about my research but also about my presentation for two years. Mr. Ito in Univ. of Tokyo gives insightful comments for my future works during his stay in Kyoto. I am also grateful my colleague Mr. Takada for discussion of my study, even at midnight. It is needless to say that my work is supported by the daily chatting with the present and past members in the room K402, Mr. Ikeda, Mr. Murakami, Mr. Sugimoto, Mr. Sinjo, Mr. Watanabe, Ms. Ichioka, Mr. Tanimoto and Mr. Yoshii.

I would like to thank W. W. Zhang and T. Hirano for fruitful discussions during the Nonequilibrium Dynamics in Astrophysics and Materials Science, Kyoto, Japan, and Andrew Hillier for corrections of the manuscript Phys. Rev. E **86**, 041308 (2012). Prof. Otsuki gives me insightful comments and suggestions about the granular physics in the meetings of the Physical Society of Japan. Discussions with Prof. Hatano have been illuminating during the 57 th Condensed Matter Physics Summer School.

Finally, I would like to thank my father, mother, brother and all of the people around me for much support to my research and my life.

Appendix A

The detail derivation for the hydrodynamical equations from Enskog equation

Here, we derive the hydrodynamical equations from RET equation.

A.1 Derivation of the moment equation from RET equation

First, we derive continuity equation for $\langle\psi\rangle$

$$\frac{\partial}{\partial t}\langle\psi\rangle = -\frac{\partial}{\partial x_{1\alpha}}J_\alpha(\psi) + I(\psi). \tag{A.1}$$

, where $\langle\cdots\rangle \equiv \int d^3v_1 f(\mathbf{x}_1, \mathbf{v}_1, t)\cdots$ and $J_\alpha = J^c_\alpha + J^k_\alpha$ with

$$J^k_\alpha \equiv \langle v_{1\alpha}\psi\rangle \tag{A.2}$$

$$\begin{aligned} J^c_\alpha &\equiv \frac{\sigma^3}{4}\int d^3v_1 d^3v_2 d^2k \int_0^1 d\lambda S(\mathbf{v}_{12}\cdot\mathbf{k})k_\alpha \qquad (A.3)\\ &\quad \Delta'\psi f^{(2)}(\mathbf{r}_1 + \sigma\mathbf{k}(1-\lambda), \mathbf{v}_1; \mathbf{r}_1 - \lambda\sigma\mathbf{k}, \mathbf{v}_2; t), \\ I(\psi) &\equiv \frac{\sigma^2}{2}\int d^3v_1 d^3v_2 d^2k S(\mathbf{v}_{12}\cdot\mathbf{k})\Delta\psi f^{(2)}(\mathbf{r}_1 + \sigma\mathbf{k}, \mathbf{v}_1; \mathbf{r}_1\mathbf{v}_2; t) \qquad (A.4) \end{aligned}$$

from Enskog equation:

$$\begin{aligned} (\frac{\partial}{\partial t} + \mathbf{v}_1\cdot\nabla_1)f(\mathbf{r}_1, \mathbf{v}_1, t) &= J_E[\mathbf{r}_1, \mathbf{v}_1|f(t)] \qquad (A.5)\\ J_E[\mathbf{r}_1, \mathbf{v}_1|f(t)] &\equiv \sigma^2\int d^3\mathbf{v}_2 d^2k S(\mathbf{k}\cdot\mathbf{v}_{12})\{\Lambda f^{(2)}(\mathbf{r}_1, \mathbf{v}_1''; \mathbf{r}_1 + \sigma\mathbf{k}, \mathbf{v}_2''; t) \\ &\quad -f^{(2)}(\mathbf{r}_1, \mathbf{v}_1; \mathbf{r}_1 - \sigma\mathbf{k}, \mathbf{v}_2; t)\} \qquad (A.6) \end{aligned}$$

Eq. (A.2) is directly obtained from the second term on the left hand side in Eq. (A.5). We perform the calculation for

$$\begin{aligned} & \int d^3v_1\psi(\mathbf{v}_1)J_E[\mathbf{r}_1,\mathbf{v}_1|f(t)] \\ = \;& \sigma^2\int d^3v_1d^3v_2d^2kS(\mathbf{k}\cdot\mathbf{v}_{12})\{\Lambda f^{(2)}(\mathbf{r}_1,\mathbf{v}_1'';\mathbf{r}_1+\sigma\mathbf{k},\mathbf{v}_2'';t) \\ & -f^{(2)}(\mathbf{r}_1,\mathbf{v}_1;\mathbf{r}_1-\sigma\mathbf{k},\mathbf{v}_2;t)\}\psi(\mathbf{v}_1), \end{aligned} \tag{A.7}$$

in the followings. By using

$$\Lambda d^3v_1d^3v_2|\mathbf{v}_{12}\cdot\mathbf{k}| = d^3v_1''d^3v_2''|\mathbf{v}_{12}''\cdot\mathbf{k}| \tag{A.8}$$

$$\Theta(\mathbf{v}_{12}''\cdot\mathbf{k}) = \Theta(-\mathbf{v}_{12}\cdot\mathbf{k}), \tag{A.9}$$

and $\mathbf{k}\to-\mathbf{k}$, the first term on the right hand side of Eq. (A.7) is rewritten as

$$\sigma^2\int d^3v_1''d^3v_2''dk^2S(\mathbf{k}\cdot\mathbf{v}_{12}'')f^{(2)}(\mathbf{r}_1,\mathbf{v}_1'';\mathbf{r}_1-\sigma\mathbf{k},\mathbf{v}_2'';t)\psi(\mathbf{v}_1). \tag{A.10}$$

Equation (A.10) contains the pre-collision velocities $(\mathbf{v}_1'',\mathbf{v}_2'')$ and the after-collision velocity $\mathbf{v}_1$. Considering the velocities before and after the collision are related as "$(\mathbf{v}_1'',\mathbf{v}_2'')\to(\mathbf{v}_1,\mathbf{v}_2)$" and "$(\mathbf{v}_1,\mathbf{v}_2)\to(\mathbf{v}_1',\mathbf{v}_2')$, " we can replace Eq. (A.10) to

$$\sigma^2\int d^3v_1d^3v_2dk^2S(\mathbf{k}\cdot\mathbf{v}_{12})f^{(2)}(\mathbf{r}_1,\mathbf{v}_1;\mathbf{r}_1-\sigma\mathbf{k},\mathbf{v}_2;t)\psi(\mathbf{v}_1'). \tag{A.11}$$

Thus, we obtain

$$\begin{aligned} & \int d^3v_1\psi(\mathbf{v}_1)J_E[\mathbf{r}_1,\mathbf{v}_1|f(t)] \\ = \;& \sigma^2\int d^3v_1d^3v_2d^2kS(\mathbf{k}\cdot\mathbf{v}_{12})f^{(2)}(\mathbf{r}_1,\mathbf{v}_1;\mathbf{r}_1-\sigma\mathbf{k},\mathbf{v}_2;t)(\psi(\mathbf{v}_1')-\psi(\mathbf{v}_1)). \end{aligned} \tag{A.12}$$

We can symmetrize Eq. (A.12) in terms of integration variables,

$$\begin{aligned} & \int d^3v_1\psi(\mathbf{v}_1)J_E[\mathbf{r}_1,\mathbf{v}_1|f(t)] \\ = \;& \frac{\sigma^2}{2}\int d^3v_1d^3v_2d^2k\{S(\mathbf{k}\cdot\mathbf{v}_{12})f^{(2)}(\mathbf{r}_1,\mathbf{v}_1;\mathbf{r}_1-\sigma\mathbf{k},\mathbf{v}_2;t)(\psi(\mathbf{v}_1')-\psi(\mathbf{v}_1)) \\ & +S(-\mathbf{k}\cdot\mathbf{v}_{12})f^{(2)}(\mathbf{r}_1,\mathbf{v}_2;\mathbf{r}_1-\sigma\mathbf{k},\mathbf{v}_1;t)(\psi(\mathbf{v}_2')-\psi(\mathbf{v}_2))\} \\ = \;& \frac{\sigma^2}{2}\int d^3v_1d^3v_2d^2k\{S(\mathbf{k}\cdot\mathbf{v}_{12})f^{(2)}(\mathbf{r}_1,\mathbf{v}_1;\mathbf{r}_1-\sigma\mathbf{k},\mathbf{v}_2;t)(\psi(\mathbf{v}_1')-\psi(\mathbf{v}_1)) \\ & +S(-\mathbf{k}\cdot\mathbf{v}_{12})f^{(2)}(\mathbf{r}_1-\sigma\mathbf{k},\mathbf{v}_1;\mathbf{r}_1,\mathbf{v}_2;t)(\psi(\mathbf{v}_2')-\psi(\mathbf{v}_2))\} \end{aligned} \tag{A.13}$$

$$\begin{aligned} = \;& \frac{\sigma^2}{2}\int d^3v_1d^3v_2d^2k\{S(\mathbf{k}\cdot\mathbf{v}_{12})f^{(2)}(\mathbf{r}_1,\mathbf{v}_1;\mathbf{r}_1-\sigma\mathbf{k},\mathbf{v}_2;t)(\psi(\mathbf{v}_1')-\psi(\mathbf{v}_1)) \\ & +S(\mathbf{k}\cdot\mathbf{v}_{12})f^{(2)}(\mathbf{r}_1+\sigma\mathbf{k},\mathbf{v}_1;\mathbf{r}_1,\mathbf{v}_2;t)(\psi(\mathbf{v}_2')-\psi(\mathbf{v}_2))\}. \end{aligned} \tag{A.14}$$

We used the property of two-body distribution function $f^{(2)}(\mathbf{r}_1, \mathbf{v}_1; \mathbf{r}_2, \mathbf{v}_2; t) = f^{(2)}(\mathbf{r}_2, \mathbf{v}_2; \mathbf{r}_1, \mathbf{v}_1; t)$ in Eq. (A.13) and changed as $\mathbf{k} \to -\mathbf{k}$ in the second term in Eq. (A.14). We use two identities:

$$\begin{aligned} & f^{(2)}(\mathbf{r}_1, \mathbf{v}_1; \mathbf{r}_1 - \sigma\mathbf{k}, \mathbf{v}_2; t) - f^{(2)}(\mathbf{r}_1 + \sigma\mathbf{k}, \mathbf{v}_1; \mathbf{r}_1, \mathbf{v}_2; t) \\ = & \int_0^1 d\lambda \frac{\partial}{\partial \lambda} f^{(2)}(\mathbf{r}_1 + \sigma\mathbf{k}(1-\lambda), \mathbf{v}_1; \mathbf{r}_1 - \lambda\sigma\mathbf{k}, \mathbf{v}_2; t) \end{aligned} \tag{A.15}$$

$$\begin{aligned} & \frac{\partial}{\partial \lambda} f^{(2)}(\mathbf{r}_1 + \sigma\mathbf{k}(1-\lambda), \mathbf{v}_1; \mathbf{r}_1 - \lambda\sigma\mathbf{k}, \mathbf{v}_2; t) \\ = & -\sigma k_\alpha \frac{\partial}{\partial x_{1\alpha}} f^{(2)}(\mathbf{r}_1 + \sigma\mathbf{k}(1-\lambda), \mathbf{v}_1; \mathbf{r}_1 - \lambda\sigma\mathbf{k}, \mathbf{v}_2; t), \end{aligned} \tag{A.16}$$

for the first term in Eq. (A.14). Then,

$$\begin{aligned} & \int d^3v_1 \psi(\mathbf{v}_1) J_E[\mathbf{r}_1, \mathbf{v}_1 | f(t)] \\ = & \frac{\sigma^2}{2} \int d^3v_1 d^3v_2 d^2k S(\mathbf{k} \cdot \mathbf{v}_{12}) \{ f^{(2)}(\mathbf{r}_1 + \sigma\mathbf{k}, \mathbf{v}_1; \mathbf{r}_1, \mathbf{v}_2; t)(\psi(\mathbf{v}_1') - \psi(\mathbf{v}_1)) \\ & + f^{(2)}(\mathbf{r}_1 + \sigma\mathbf{k}, \mathbf{v}_1; \mathbf{r}_1, \mathbf{v}_2; t)(\psi(\mathbf{v}_2') - \psi(\mathbf{v}_2)) \\ & - \sigma k_\alpha \frac{\partial}{\partial x_{1\alpha}} f^{(2)}(\mathbf{r}_1 + \sigma\mathbf{k}(1-\lambda), \mathbf{v}_1; \mathbf{r}_1 - \lambda\sigma\mathbf{k}, \mathbf{v}_2; t)(\psi(\mathbf{v}_1') - \psi(\mathbf{v}_1)) \} \end{aligned} \tag{A.17}$$

$$\begin{aligned} = & \frac{\sigma^2}{2} \int d^3v_1 d^3v_2 d^2k S(\mathbf{k} \cdot \mathbf{v}_{12}) \{ f^{(2)}(\mathbf{r}_1 + \sigma\mathbf{k}, \mathbf{v}_1; \mathbf{r}_1, \mathbf{v}_2; t) \Delta\psi \\ & - \sigma k_\alpha \frac{\partial}{\partial x_{1\alpha}} f^{(2)}(\mathbf{r}_1 + \sigma\mathbf{k}(1-\lambda), \mathbf{v}_1; \mathbf{r}_1 - \lambda\sigma\mathbf{k}, \mathbf{v}_2; t)(\psi(\mathbf{v}_1') - \psi(\mathbf{v}_1)) \} \end{aligned} \tag{A.18}$$

$$\begin{aligned} = & I(\psi) + \frac{\sigma^3}{2} \frac{\partial}{\partial x_{1\alpha}} \int d^3v_1 d^3v_2 d^2k S(\mathbf{k} \cdot \mathbf{v}_{12}) k_\alpha \\ & \int_0^1 d\lambda f^{(2)}(\mathbf{r}_1 + \sigma\mathbf{k}(1-\lambda), \mathbf{v}_1; \mathbf{r}_1 - \lambda\sigma\mathbf{k}, \mathbf{v}_2; t)(\psi(\mathbf{v}_1') - \psi(\mathbf{v}_1)). \end{aligned} \tag{A.19}$$

By using the similar symmetrization

$$\text{The second term in Eq. (A.19)} \tag{A.20}$$

$$\begin{aligned} = & -\frac{\sigma^3}{4} \frac{\partial}{\partial x_{1\alpha}} \int d^3v_1 d^3v_2 d^2k \int_0^1 d\lambda S(\mathbf{k} \cdot \mathbf{v}_{12}) k_\alpha \\ & \{ f^{(2)}(\mathbf{r}_1 + \sigma\mathbf{k}(1-\lambda), \mathbf{v}_1; \mathbf{r}_1 - \lambda\sigma\mathbf{k}, \mathbf{v}_2; t)(\psi(\mathbf{v}_1') - \psi(\mathbf{v}_1)) \\ & + f^{(2)}(\mathbf{r}_1 + \sigma\mathbf{k}(1-\lambda), \mathbf{v}_2; \mathbf{r}_1 - \lambda\sigma\mathbf{k}, \mathbf{v}_1; t)(\psi(\mathbf{v}_2') - \psi(\mathbf{v}_2)) \} \end{aligned} \tag{A.21}$$

$$\begin{aligned} = & -\frac{\sigma^3}{4} \frac{\partial}{\partial x_{1\alpha}} \int d^3v_1 d^3v_2 d^2k \int_0^1 d\lambda S(\mathbf{k} \cdot \mathbf{v}_{12}) k_\alpha \\ & \{ f^{(2)}(\mathbf{r}_1 + \sigma\mathbf{k}(1-\lambda), \mathbf{v}_1; \mathbf{r}_1 - \lambda\sigma\mathbf{k}, \mathbf{v}_2; t)(\psi(\mathbf{v}_1') - \psi(\mathbf{v}_1)) \\ & + f^{(2)}(\mathbf{r}_1 - \lambda\sigma\mathbf{k}, \mathbf{v}_1; \mathbf{r}_1 + \sigma\mathbf{k}(1-\lambda), \mathbf{v}_2; t)(\psi(\mathbf{v}_2') - \psi(\mathbf{v}_2)) \} \end{aligned} \tag{A.22}$$

$$= -\frac{\sigma^3}{4}\frac{\partial}{\partial x_{1\alpha}}\int d^3v_1 d^3v_2 d^2k \int_0^1 d\lambda S(\mathbf{k}\cdot\mathbf{v}_{12})k_\alpha \{f^{(2)}(\mathbf{r}_1+\sigma\mathbf{k}(1-\lambda),\mathbf{v}_1;\mathbf{r}_1-\lambda\sigma\mathbf{k},\mathbf{v}_2;t)\Delta'\psi, \quad (A.23)$$

we obtain Eq. (A.3).

A.2 Derivation of the hydrodynamical equations

Let us derive hydrodynamical equations

$$(\partial_t + \bar{v}_\beta\partial_\beta)n = -n\partial_\beta\bar{v}_\beta \quad (A.24)$$

$$(\partial_t + \bar{v}_\beta\partial_\beta)\bar{v}_\alpha = -\frac{1}{mn}\partial_\beta\sigma_{\alpha\beta} \quad (A.25)$$

$$(\partial_t + \bar{v}_\beta\partial_\beta)T_g = -\frac{2}{3n}\{\partial_\beta q_\beta + (\partial_\beta\bar{v}_\alpha)\sigma_{\alpha\beta}\} - \zeta T_g, \quad (A.26)$$

by substituting $\psi = 1, v_{1\alpha}, \mathbf{v}_1^2$ in Eq. (A.5). Eq. (A.24) is trivial. $\Delta\psi$ and $\Delta'\psi$ are described as

$$\Delta' v_{1\alpha} = (1+e)g_{21}k_\alpha \quad (A.27)$$

$$\Delta v_{1\alpha} = 0 \quad (A.28)$$

$$\Delta'\mathbf{v}_1^2 = 2(1+e)g_{21}k_\alpha V_{12\alpha} \quad (A.29)$$

$$\Delta\mathbf{v}_1^2 = (1+e)g_{21}\{\frac{1+e}{2}g_{21}k_\alpha k_\alpha - v_{21\alpha}k_\alpha\} \quad (A.30)$$

$$= -\frac{(1-e^2)}{2}g_{21}^2, \quad (A.31)$$

with $V_{12\alpha} \equiv (v_{1\alpha}+v_{2\alpha})/2$. By using Eq. (A.24),

$$\partial_t n\bar{v}_\alpha + \partial_\beta\langle v_{1\alpha}v_{1\alpha}\rangle = \bar{v}_\alpha\partial_t n + n\partial_t\bar{v}_\alpha + \partial_\beta(n\bar{v}_\alpha\bar{v}_\beta + \frac{\sigma^k_{\alpha\beta}}{m}) \quad (A.32)$$

$$= n(\partial_t + \bar{v}_\beta\partial_\beta)\bar{v}_\alpha + \frac{1}{m}\partial_\beta\sigma^k_{\alpha\beta}. \quad (A.33)$$

The expression for the contact stress is directly obtained from the definition of J^c. Thus, Eq. (A.25) is obtained. From

$$J^c_\beta(m\mathbf{v}_1^2) = \frac{\sigma^3 m}{4}\int d^3v_1 d^3v_2 d^2k S(g_{12})k_\beta\Delta' v_\alpha^2 f^{(2)} \quad (A.34)$$

$$= \frac{\sigma^3 m}{4}\int d^3v_1 d^3v_2 d^2k\Theta(g_{12})2(1+e)g_{12}^2 k_\alpha k_\beta V_{12\alpha}f^{(2)} \quad (A.35)$$

$$= \frac{\sigma^3 m}{4}\int d^3v_1 d^3v_2 d^2k\Theta(g_{12})2(1+e)g_{12}^2(\bar{v}_\alpha + \tilde{V}_{12\alpha})k_\alpha k_\beta f^{(2)}$$

$$= 2\bar{v}_\alpha\sigma^c_{\alpha\beta} + 2q^c_\beta, \quad (A.36)$$

and

$$J^k_\beta(m\mathbf{v}_1^2) = \langle m v_{1\beta}\mathbf{v}_1^2\rangle \quad (A.37)$$

$$= \bar{v}_\beta\{mn\bar{\mathbf{v}}^2 + 3nT_g\} + 2\bar{v}_\alpha\sigma^k_{\alpha\beta} + 2q^k_\beta, \quad (A.38)$$

we obtain

$$J^k_\beta(m\mathbf{v}_1^2) + J^c_\beta(m\mathbf{v}_1^2) = \bar{v}_\beta\{mn\bar{\mathbf{v}}^2 + nT_\alpha\} + 2\bar{v}_\alpha\sigma_{\alpha\beta} + 2q_\beta, \quad (A.39)$$

with heat flux $q_\alpha \equiv q^k_\alpha + q^c_\alpha$ and the kinetic contribution $q^k_\alpha \equiv m\langle \mathbf{u}_1^2 u_{1\alpha}\rangle/2$. And the cooling rate ζ_α would be

$$\zeta = -\frac{I(m\mathbf{v}_1^2)}{3nT_g}. \quad (A.40)$$

$$\partial_t\{mn\bar{\mathbf{v}}^2 + n3T_g\} = (m\mathbf{v}^2 + 3T_g)\partial_t n + 2mn\bar{v}_\alpha\partial_t\bar{v}_\alpha + n\partial_t 3T_g \quad (A.41)$$

$$= -(m\mathbf{v}^2 + 3T_g)\sum_\beta \bar{v}_\beta\partial_\beta n - 2mn\bar{v}_\alpha\sum_\beta\frac{\partial\sigma_{\alpha\beta}}{\partial x_\beta}$$

$$-2mn\bar{v}_\alpha\sum_\beta\bar{v}_\beta\partial_\beta\bar{v}_\alpha + n\partial_t 3T_g \quad (A.42)$$

From Eqs. (A.5)(A.39)(A.40) and (A.42), we obtain Eq. (A.26).

Appendix B

Discrete Element Method in detail

In this appendix, how to implement DEM is explained. We follow the notation in Ref. [68]

B.1 Transformation of Coodinates

The positions, velocities and angular velocities of grains are described in the Cartesian coordinate. To calculate the force between grains, the relative displacements and relative velocities of them in normal and tangential directions, which is obtained from their positions velocities and angular velocities, are necessary. After the calculation of forces, those in normal and tangential directions are transformed into those in Cartesian coordinate. Here, we explain how to transform the relative velocities and displacements in Cartesian coordinate into those in the normal and tangential directions, and vice versa.

The transformation matrix $R(\hat{\phi}, \hat{\theta})$ of basis from Cartesian coordinate $(\hat{x}, \hat{y}, \hat{z})$ to the spherical coordinate $(\hat{r}, \hat{\theta}, \hat{\phi})$ can be written as,

$$R(\hat{\phi}, \hat{\theta}) = \begin{pmatrix} \cos\hat{\phi} & -\sin\hat{\phi} & 0 \\ \sin\hat{\phi} & \cos\hat{\phi} & 0 \\ 0 & 0 & 1 \end{pmatrix} \begin{pmatrix} \cos\hat{\theta} & 0 & -\sin\hat{\theta} \\ 0 & 1 & 0 \\ \sin\hat{\theta} & 0 & \cos\hat{\theta} \end{pmatrix} \tag{B.1}$$

$$= \begin{pmatrix} \cos\hat{\phi}\cos\hat{\theta} & -\sin\hat{\phi} & \cos\hat{\phi}\sin\hat{\theta} \\ \sin\hat{\phi}\cos\hat{\theta} & \cos\hat{\phi} & \sin\hat{\phi}\sin\hat{\theta} \\ -\sin\hat{\theta} & 0 & \cos\hat{\theta} \end{pmatrix}. \tag{B.2}$$

i.e. basis vectors in spherical coordinate $\mathbf{e}_r, \mathbf{e}_\theta$ and $\mathbf{e}_\phi$ and those in Cartesian

coordinate $\mathbf{e}_x, \mathbf{e}_y$ and $\mathbf{e}_z$ are related as

$$\begin{aligned} \mathbf{e}_\theta &= R(\hat{\phi},\hat{\theta})\mathbf{e}_x && \text{(B.3)} \\ \mathbf{e}_\phi &= R(\hat{\phi},\hat{\theta})\mathbf{e}_y && \text{(B.4)} \\ \mathbf{e}_r &= R(\hat{\phi},\hat{\theta})\mathbf{e}_z && \text{(B.5)} \end{aligned}$$

For an arbitrary vector $\mathbf{A}$,

$$\begin{aligned} \begin{pmatrix} A_{\hat{x}} \\ A_{\hat{y}} \\ A_{\hat{z}} \end{pmatrix} &= A_x\mathbf{e}_x + A_y\mathbf{e}_y + A_z\mathbf{e}_z && \text{(B.6)} \\ &= A_\theta\mathbf{e}_\theta + A_\phi\mathbf{e}_\phi + A_r\mathbf{e}_r && \text{(B.7)} \\ &= A_\theta R(\hat{\phi},\hat{\theta})\mathbf{e}_x + A_\phi R(\hat{\phi},\hat{\theta})\mathbf{e}_y + A_r R(\hat{\phi},\hat{\theta})\mathbf{e}_z && \text{(B.8)} \\ &= R(\hat{\phi},\hat{\theta}) \begin{pmatrix} A_{\hat{\theta}} \\ A_{\hat{\phi}} \\ A_{\hat{r}} \end{pmatrix} && \text{(B.9)} \end{aligned}$$

holds. Then, by using $R(\hat{\phi},\hat{\theta})R^t(\hat{\phi},\hat{\theta}) = \mathbf{1}$ with identity matrix $\mathbf{1}$, $\mathbf{A}$ would be transformed via

$$\begin{pmatrix} A_{\hat{\theta}} \\ A_{\hat{\phi}} \\ A_{\hat{r}} \end{pmatrix} = R^t(\hat{\phi},\hat{\theta}) \begin{pmatrix} A_{\hat{x}} \\ A_{\hat{y}} \\ A_{\hat{z}} \end{pmatrix}, \qquad \text{(B.10)}$$

where R^t denotes the transposed matrix of R.

On the contact point of grains, by using the transformation rule Eq. (B.10), the contribution of the rotation of grains to the velocity is

$$\begin{aligned} \boldsymbol{\omega}_i \times \frac{\sigma}{2}\mathbf{e}_r &= \frac{\sigma}{2}(\omega_r\mathbf{e}_r + \omega_\theta\mathbf{e}_\theta + \omega_\phi\mathbf{e}_\phi) \times \mathbf{e}_r && \text{(B.11)} \\ &= \frac{\sigma}{2} \begin{pmatrix} \omega_\phi \\ -\omega_\theta \\ 0 \end{pmatrix} && \text{(B.12)} \\ &= \frac{\sigma}{2} \begin{pmatrix} -\omega_x \sin\hat{\phi} + \omega_y \cos\hat{\phi} \\ -(\omega_x \cos\hat{\theta}\cos\hat{\phi} + \omega_y \cos\hat{\theta}\sin\hat{\phi} - \omega_z \sin\hat{\theta}) \\ 0 \end{pmatrix} && \text{(B.13)} \\ &= \frac{\sigma}{2} L(\hat{\phi},\hat{\theta}) \begin{pmatrix} \omega_x \\ \omega_y \\ \omega_z \end{pmatrix}, && \text{(B.14)} \end{aligned}$$

where the new matrix $L(\hat{\phi},\hat{\theta})$ is introduced:

$$L(\hat{\phi},\hat{\theta}) \equiv \begin{pmatrix} -\sin\hat{\phi} & \cos\hat{\phi} & 0 \\ -\cos\hat{\theta}\cos\hat{\phi} & \cos\hat{\theta}\sin\hat{\phi} & \sin\hat{\theta} \\ 0 & 0 & 0 \end{pmatrix}. \qquad \text{(B.15)}$$

Following the similar calculation, the moment $\mathbf{M}^{ij}$ and $\mathbf{F}^{ij}$ in the spherical coordinate are related via

$$\begin{pmatrix} M_x^{ij} \\ M_y^{ij} \\ M_z^{ij} \end{pmatrix} = \frac{\sigma}{2} L^t \begin{pmatrix} F_\theta^{ij} \\ F_\phi^{ij} \\ F_r^{ij} \end{pmatrix}. \tag{B.16}$$

The transformation rule Eq. (B.10) and (B.16) are adopted with $\cos\hat{\theta} = (z_j - z_i)/r_{ij}, \sin\hat{\theta} = r_{ij}^{(z)}/r_{ij}, \cos\hat{\theta} = (x_j - x_i)/r_{ij}^{(z)}$, $\sin\hat{\theta} = (y_j - y_i)/r_{ij}^{(z)}$ and $r_{ij}^{(z)} \equiv \sqrt{(x_j - x_i)^2 + (y_j - y_i)^2}$, where, in the case of, $r_{ij}^{(z)} = 0$, we choose $\hat{\theta} = 0$ for $z_j - z_i > 0$ and $\hat{\theta} = \pi$ for $z_j - z_i \leq 0$. Thus, the relative displacement on the contact point ${}^t(u_t, u_s, u_n)$ would be described as

$$\begin{pmatrix} u_t^{ij} \\ u_s^{ij} \\ u_n^{ij} \end{pmatrix} = R^t(\hat{\phi}, \hat{\theta}) \begin{pmatrix} \Delta x^{ij} \\ \Delta y^{ij} \\ \Delta z^{ij} \end{pmatrix} + \frac{\sigma}{2} L(\hat{\phi}, \hat{\theta}) \begin{pmatrix} \Delta\Psi_x^{ij} \\ \Delta\Psi_y^{ij} \\ \Delta\Psi_z^{ij} \end{pmatrix}. \tag{B.17}$$

After the calculation of the force, the inverse transformation is performed for $(F_x^{ij}, F_y^{ij}, F_z^{ij})$:

$$\begin{pmatrix} F_x^{ij} \\ F_y^{ij} \\ F_z^{ij} \end{pmatrix} = R(\hat{\phi}, \hat{\theta}) \begin{pmatrix} F_t^{ij} \\ F_s^{ij} \\ F_n^{ij} \end{pmatrix} \tag{B.18}$$

to integrate EoM in Cartesian coordinate.

For two-dimensional case, since $z_j - z_i = 0$, we choose $\cos\hat{\theta} = 0, \sin\hat{\theta} = 1, \cos\hat{\phi} = (x_j - x_i)/r_{ij}^{(z)}$ and $\sin\hat{\phi} = (y_j - y_i)/r_{ij}^{(z)}$ for matrix $R(\hat{\phi}, \hat{\theta})$ and $L(\hat{\phi}, \hat{\theta})$.

B.2 Time Integration of Equations of Motion

We adopt the second-order Adams-Bashforth method for the time integration with the time interval $\Delta t = 0.02 t_c$. We solve EoMs for i th particle

$$m\dot{v}_{i\alpha} = F_\alpha^i \tag{B.19}$$

$$I\dot{\omega}_{i\alpha} = M_\alpha^i, \tag{B.20}$$

where $F_\alpha^i \equiv \sum_j F_\alpha^{ij}$ and $M_\alpha^i \equiv M_\alpha^{ij}$ are introduced. After the time interval $t \to t + \Delta t$, $v_{i\alpha}(t + \Delta t), \omega_{i\alpha}(t + \Delta t), x_{i\alpha}(t + \Delta t)$ and $\phi_{i\alpha}(t + \Delta t)$ are described as

$$v_{i\alpha}(t + \Delta t) = v_{i\alpha}(t) + \frac{\Delta t}{2m}(3F_{i\alpha}(t) - F_{i\alpha}(t - \Delta t)) \tag{B.21}$$

$$\omega_{i\alpha}(t + \Delta t) = \omega_{i\alpha}(t) + \frac{\Delta t}{2I}(3M_{i\alpha}(t) - M_{i\alpha}(t - \Delta t)) \tag{B.22}$$

$$x_{i\alpha}(t + \Delta t) = x_{i\alpha}(t) + \frac{\Delta t}{2}(v_{i\alpha}(t + \Delta t) + v_{i\alpha}(t)) \tag{B.23}$$

$$\phi_{i\alpha}(t + \Delta t) = \phi_{i\alpha}(t) + \frac{\Delta t}{2}(\omega_{i\alpha}(t + \Delta t) + \omega_{i\alpha}(t)) \tag{B.24}$$

It should be noted that $\Delta t(3F_{i\alpha}(t)-F_{i\alpha}(t-\Delta t))/2m \simeq \Delta t F_{i\alpha}(t)/m+\Delta t^2 \dot{F}_{i\alpha}(t)/2m+ O(\Delta t^3)$ and $\Delta t(3M_{i\alpha}(t) - M_{i\alpha}(t-\Delta t))/2I \simeq \Delta t M_{i\alpha}(t)/I + \Delta t^2 \dot{M}_{i\alpha}(t)/2I + O(\Delta t^3)$ hold. Thus, by adopting this method, the Δt^2 accuracy is promised.

B.3 Event-Driven algorithm for collisions of grains

Event-Driven algorithms are sometimes used, because they are efficient. ED algorithms contain following steps. First, from the data of positions and velocities of grains, all possible interval in which two grains collide and their minimum is chosen as the time step Δt. Secondly, the chosen two grains collide and their velocities are converted into new ones under the collision rule and other non-collision grains move freely at their respective velocities. Then the next collision pair is chosen.

Actually the ED algorithm is more efficient than DEM. However, because the ED algorithms are oversimplified procedures, there are several problems in them. The superiority of the DEM would be followings. The DEM can be used even for dense systems above the jamming point, while ED algorithm simulation cannot reach the jamming point. We also indicate that the primitive ED algorithms encounter the inelastic collapse, though it can be avoided by introducing velocity-dependent restitution coefficient to the ED algorithms [164]. In contrast, DEM has an advantage that it is free from the inelastic collapse and we can easily include the effect of friction and rotation of grains. For these reasons, we adopt DEM.

Appendix C

How to calculate the local stress tensor

In this appendix, we show how to calculate the stress tensor locally, following Ref. [167, 168].

C.1 Derivation of the microscopic description of the stress tensor

Firstly, we derive the microscopic definition of the stress tensor. Let us write the density $n(\mathbf{x}, t)$ and the velocity field $\bar{v}_\alpha(\mathbf{x}, t)$ in terms of the delta function:

$$n(\mathbf{x}, t) = \sum_i \delta(\mathbf{r}_i(t) - \mathbf{x}) \tag{C.1}$$

$$n\bar{v}_\alpha(\mathbf{x}, t) = \sum_i v_{i\alpha}\delta(\mathbf{r}_i(t) - \mathbf{x}). \tag{C.2}$$

The continuity equations would be

$$\frac{\partial n}{\partial t} + \bar{v}_\alpha \frac{\partial n}{\partial x_\alpha} = -n\frac{\partial \bar{v}_\alpha}{\partial x_\alpha}, \tag{C.3}$$

and

$$n\frac{\partial \bar{v}_\alpha}{\partial t} = \frac{\partial n\bar{v}_\alpha}{\partial t} - \bar{v}_\alpha \frac{\partial n}{\partial t} \tag{C.4}$$

$$= \sum_i (v_{i\alpha}\dot{\mathbf{x}} \cdot \nabla\delta(\mathbf{r}_i - \mathbf{x})) + \sum_i \dot{v}_{i\alpha}\delta(\mathbf{r}_i - \mathbf{x}) + \bar{v}_\alpha\bar{v}_\beta\frac{\partial n}{\partial x_\beta} + n\bar{v}_\alpha\frac{\partial \bar{v}_\beta}{\partial x_\beta} \tag{C.5}$$

$$= -\frac{\partial}{\partial x_\beta}\sum_i \{v_{i\alpha}v_{i\beta}\delta(\mathbf{r}_i - \mathbf{x})\} + \sum_i \dot{v}_{i\alpha}\delta(\mathbf{r}_i - \mathbf{x})$$

$$+\bar{v}_\alpha \bar{v}_\beta \frac{\partial n}{\partial x_\beta} + n\bar{v}_\alpha \frac{\partial \bar{v}_\beta}{\partial x_\beta} \tag{C.6}$$

$$= -\frac{\partial}{\partial x_\beta} \sum_i \left(u_{i\alpha} u_{i\beta} \delta(\mathbf{r}_i - \mathbf{x}) \right) + \sum_i \dot{v}_{i\alpha} \delta(\mathbf{r}_i - \mathbf{x}) \tag{C.7}$$

$$= -\frac{1}{m} \left(\frac{\partial \sigma^k_{\alpha\beta}}{\partial x_\beta} + S \right), \tag{C.8}$$

where the kinetic contribution of the stress tensor $\sigma^k_{\alpha\beta}$ and the interaction potential-contribution S are introduced as

$$\sigma^k_{\alpha\beta} \equiv \sum_i m u_{i\alpha} u_{i\beta} \delta(\mathbf{r}_i - \mathbf{x}) \tag{C.9}$$

$$S \equiv \sum_i m \dot{v}_{i\alpha} \delta(\mathbf{r}_i - \mathbf{x}) \tag{C.10}$$

We derive the explicit expression for S in the followings. By using EoMs $m\dot{v}_{i\alpha} = f_{i\alpha} = \sum_j F^{ij}_\alpha$,

$$S = \sum_i F_{i\alpha} \delta(\mathbf{r}_i(t) - \mathbf{x}) \tag{C.11}$$

$$= \sum_{ij} F^{ij}_\alpha \delta(\mathbf{r}_i(t) - \mathbf{x}) \tag{C.12}$$

$$= \sum_{i<j} F^{ij}_\alpha \delta(\mathbf{r}_i(t) - \mathbf{x}) + \sum_{j<i} f^{ij}_\alpha \delta(\mathbf{r}_i(t) - \mathbf{x}) \tag{C.13}$$

$$= \sum_{i<j} F^{ij}_\alpha \{ \delta(\mathbf{r}_i(t) - \mathbf{x}) - \delta(\mathbf{r}_j(t) - \mathbf{x}) \} \tag{C.14}$$

We use the identity for $\delta(\mathbf{r}_i(t) - \mathbf{x}) - \delta(\mathbf{r}_j(t) - \mathbf{x})$.

$$\delta(\mathbf{r}_i - \mathbf{x}) - \delta(\mathbf{r}_j - \mathbf{x}) = -\int_0^1 d\lambda \frac{d}{d\lambda} \delta(\mathbf{r}_i - \mathbf{x} + \lambda(\mathbf{r}_j - \mathbf{r}_i)) \tag{C.15}$$

$$= -\frac{\partial}{\partial x_\beta} r_{ij\beta} \int_0^1 d\lambda \delta(\mathbf{r}_i - \mathbf{x} + \lambda(\mathbf{r}_j - \mathbf{r}_i)). \tag{C.16}$$

Substituting Eq. (C.16) into Eq. (C.14), we obtain

$$S = -\sum_{i<j} F^{ij}_\alpha \frac{\partial}{\partial x_\beta} r_{ij\beta} \int_0^1 d\lambda \delta(\mathbf{r}_i - \mathbf{x} + \lambda(\mathbf{r}_j - \mathbf{r}_i)) \tag{C.17}$$

$$= -\frac{\partial \sigma^c_{\alpha\beta}}{\partial x_\beta}, \tag{C.18}$$

where we define the potential-contribution of the stress tensor, which we call the contact stress,

$$\sigma^c_{\alpha\beta} \equiv \sum_{i<j} F^{ij}_\alpha r_{ij\beta} \int_0^1 d\lambda \delta(\mathbf{r}_i - \mathbf{x} + \lambda(\mathbf{r}_j - \mathbf{r}_i)) \tag{C.19}$$

In summary, the microscopic definition of the kinetic and contact stress are

$$\sigma^k_{\alpha\beta}(\mathbf{x},t) = \sum_i m u_{i\alpha} u_{i\beta} \delta(\mathbf{r}_i - \mathbf{x}) \tag{C.20}$$

$$\sigma^c_{\alpha\beta}(\mathbf{x},t) = \sum_{i,j} \frac{1}{2} F^{ij}_\alpha r_{ij\beta} \int_0^1 d\lambda \delta(\mathbf{r}_i - \mathbf{x} + \lambda(\mathbf{r}_j - \mathbf{r}_i)). \tag{C.21}$$

C.2 Derivation the local stress tensor

From here, we show how to calculate Eqs. (C.20) and (C.21) in the local mesh whose volume is $|\omega|$. For simplicity, we consider one-dimensional case $z < z' < z + \Delta z$, where the extension toward 2D, 3D or several coordinate cases would be straightforward. We introduce local $\bar{\sigma}^k$ and $\bar{\sigma}^c$ as

$$\bar{\sigma}^k_{\alpha\beta} \equiv \frac{1}{|\omega|} \int_{\mathbf{x}\in\omega} \sigma^k_{\alpha\beta} d\mathbf{x} \tag{C.22}$$

$$\bar{\sigma}^c_{\alpha\beta} \equiv \frac{1}{|\omega|} \int_{\mathbf{x}\in\omega} \sigma^c_{\alpha\beta} d\mathbf{x}. \tag{C.23}$$

The kinetic part can be calculated easily:

$$\bar{\sigma}^k_{\alpha\beta} = \frac{1}{\Delta z} \sum_{z<r_{iz}<z+\Delta z} m u_{i\alpha} u_{i\beta}. \tag{C.24}$$

However, the calculation for $\bar{\sigma}^c_{\alpha\beta}$ in non-trivial, in the case that the interaction between i and j cross the different mesh. We use the Heaviside functions for integration:

$$\frac{1}{|\omega|} \int dx \int dy \int_z^{z+\Delta z} dz' \cdots = \frac{1}{|\omega|} \int dx \int dy \int dz' \Theta(z'-z)\Theta(z+\Delta z - z') \cdots . \tag{C.25}$$

$$\bar{\sigma}^c_{\alpha\beta} = \frac{1}{|\omega|} \int dxdy \int dz' \Theta(z'-z)\Theta(z+\Delta z - z')\sigma^c_{\alpha\beta} \tag{C.26}$$

$$= \frac{1}{\Delta z} \sum_{i,j} \frac{1}{2} F^{ij}_\alpha r_{ij\beta} A(r_{iz}, r_{jz}, z), \tag{C.27}$$

where we define

$$A(r_{iz}, r_{jz}, z) \equiv \int dz' \Theta(z'-z)\Theta(z+\Delta z - z') \int_0^1 d\lambda \delta(r_{iz} - z + \lambda(r_{jz} - r_{iz}))$$

$$= \int dz' \Theta(z'-z)\Theta(z+\Delta z - z') \int_{r_{iz}}^{r_{jz}} \frac{d\tilde{\lambda}}{r_{jz} - r_{iz}} \delta(\tilde{\lambda} - z) \tag{C.28}$$

$$= \frac{1}{r_{jz} - r_{iz}} \int_{r_{iz}}^{r_{jz}} d\tilde{\lambda} \Theta(\tilde{\lambda} - z)\Theta(z + \Delta z - \tilde{\lambda}). \tag{C.29}$$

The factor $A(r_{iz}, r_{jz}, z)$ denotes the ratio of the overlap between the distance toward the mesh boundary from r_{iz} and the interaction length $r_{jz} - r_{iz}$. For example, if i th and j th particles are in the same mesh $z < r_{iz}, r_{jz} < z + \Delta z$, $A(r_{iz}, r_{jz}, z) = 1$. However, if they are in the different mesh $z < r_{iz} < z + \Delta z < r_{jz}$,

$$A(r_{iz}, r_{jz}, z) = \frac{z + \Delta z - r_{iz}}{r_{jz} - r_{iz}}. \tag{C.30}$$

In Fig. (C.1), we show the schematic picture for the calculation of A in the

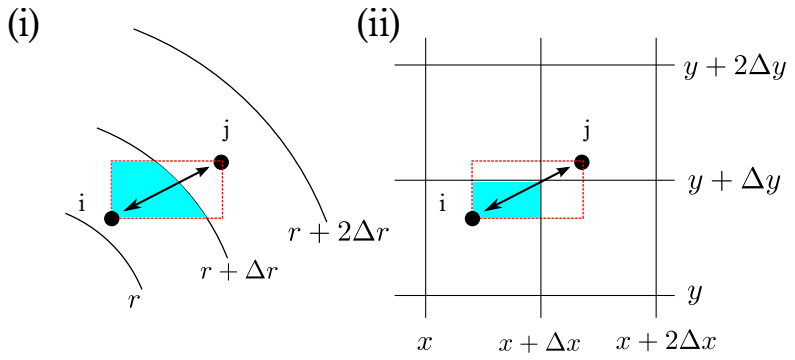

Figure C.1: Schematic picture for the calculation of A in the cylindrical coordinate (i) and 2D Cartesian coordinate (ii). A denotes the ratio of area of the sky-colored region to that of the region enclosed by the red dashed line.

cylindrical coordinate (i) and 2D Cartesian coordinate (ii). A denotes the ratio of area of the sky-colored region to that of the region enclosed by the red dashed line. In general, we write

$$\bar{\sigma}^k_{\alpha\beta} = \frac{1}{|\omega|} \sum_{i \in \omega} m u_{i\alpha} u_{i\beta} \tag{C.31}$$

$$\bar{\sigma}^c_{\alpha\beta} = \frac{1}{|\omega|} \sum_{i,j \in \omega} \frac{1}{2} F^{ij}_\alpha r_{ij\beta} A(\mathbf{r}_i, \mathbf{r}_j, \mathbf{r}), \tag{C.32}$$

where we define the general form of A

$$\begin{aligned} A(\mathbf{r}_i, \mathbf{r}_j, \mathbf{r}) \equiv & \frac{1}{A_{ij}} \int_{r_{ix}}^{r_{jx}} d\lambda_x \Theta(\lambda_x - x)\Theta(x + \Delta x - \lambda_x) \\ & \times \int_{r_{iy}}^{r_{jy}} d\lambda_y \Theta(\lambda_y - y)\Theta(y + \Delta y - \lambda_y) \\ & \times \int_{r_{iz}}^{r_{jz}} d\lambda_z \Theta(\lambda_z - z)\Theta(z + \Delta z - \lambda_z), \end{aligned} \tag{C.33}$$

with $A_{ij} \equiv (r_{jx} - r_{ix})(r_{jy} - r_{iy})(r_{jz} - r_{iz})$. We analyze the stress tensor $\sigma_{\alpha\beta} = \bar{\sigma}^k_{\alpha\beta} + \bar{\sigma}^c_{\alpha\beta}$ locally by using the description, using Eqs. (C.31), (C.32) and (C.33)

Appendix D

Analysis on a shear stress vs strain rate plane in 3D

In this Appendix, we try to estimate the shear viscosity data on a shear stress σ_{rz} vs strain rate D_{rz} plane. Data points for σ_{rz} and D_{rz} in the each mesh for frictional case with $\tilde{\phi}_0 \equiv \phi_0/\phi_{\rm fcc} = 0.90$, where ϕ_0 is the volume fraction before the impact and and $\phi_{\rm fcc}$ is that for fcc crystals, are plotted(Fig. D. 1). The point for the smallest D_{rz} and for the smallest σ_{rz} denote that for $r/R_{\rm tar} = 0.1$ and $r/R_{\rm tar} = 0.9$ with the target radius $R_{\rm tar}$, respectively. Although from fitting a line to three other points, we may estimate the shear viscosity, but the estimated value is negative. We have verified that this tendency is insensitive to the choice of a specific $\tilde{\phi}_0$.

The negative viscosity, which is totally unphysical, may be the consequence of the local variation of the volume fraction ϕ and the granular temperature T_g between each mesh. The profiles of ϕ and T_g are shown in Fig. D.2. In a usual setup, when we estimate the shear viscosity on a σ_{rz} vs D_{rz} plane, σ_{rz} and D_{rz} are not the local quantities, but the bulk quantities. Thus, ϕ and T_g are homogeneous and D_{rz} can be controlled [137]. However, in our setup with fixing ϕ and T_g, D_{rz} cannot be controlled.

Judging from non-uniformity for volume fraction and granular temperature, we do not adopt the viscosity evaluated on the stress-strain rate plane, but adopt the local viscosity as explained in the text.

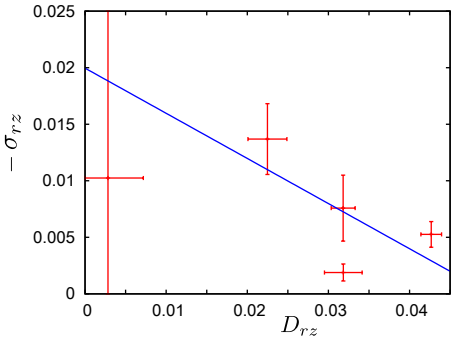

Figure D.1: σ_{rz} and D_{rz} for frictional case with $\tilde{\phi}_0 = 0.90$ are plotted. The point for the smallest D_{rz} and for the smallest σ_{rz} denote that for $r = \Delta r/2$ and $r = 5\Delta r/2$, respectively. By fitting a line to three other points, negative shear viscosity may be estimated.

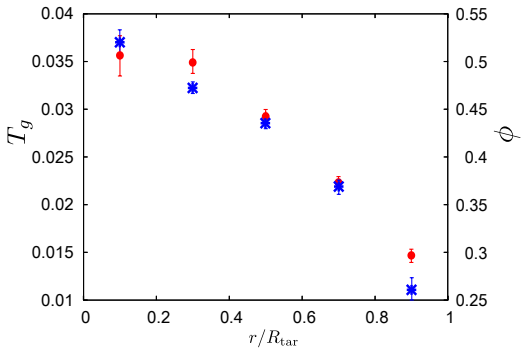

Figure D.2: The profile of the granular temperature and volume fraction. Red points and blue asterisks denote T_g and ϕ for the corresponding mesh, respectively.

Appendix E

On artificial burst-like flows in 2D

In this appendix, we comment the artificial burst-like flow in 2D, which appears in the case of large μ_p with softer grains than in the text. After the impact of jets composed of softer grains with large μ_p, because large tangential force can be accumulated before the slip of a grain, the burst occurs, when a grain slips. In Fig.E.1, we show the time evolutions of T_g at $-\Delta y < y < 0$ in (a) layer for frictionless and $\mu_p = 0.2$ case (i) and $\mu_p = 1.0$ case for several stiffness (ii), where T_g for the frictionless case and $\mu_p = 0.2$ case reaches the small steady values, while T_g raise many times after the impact for $\mu_p = 1.0$ with large t_c cases, due to the slip events. As t_c becomes smaller, the burst-like flows are suppressed. Thus, we use harder grains for large μ_p case. Though there are a few small raises of T_g for the frictionless case, they are out of our averaging time.

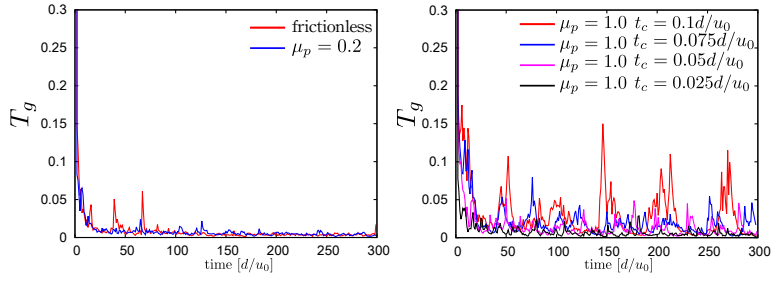

Figure E.1: The time evolution of T_g at $-\Delta y < y < 0$ in (a) layer for frictionless and $\mu_p = 0.2$ case (i) and $\mu_p = 1.0$ case for several stiffness (ii). As t_c becomes smaller, the burst-like flows are suppressed.

Bibliography

[1] K. H. Ackermann *et al.* (STAR Collaboration), Phys. Rev. Lett. **86** 402 (2001).

[2] J-Y. Ollitrault, Phys. Rev. D **46** 229 (1992).

[3] T. Hirano, and Y. Nara, Phys. Rev. C **79**, 064904 (2009).

[4] T. Hirano and Y. Nara, Prog. Theor. Exp. Phys. (2012), 1A203.

[5] K. Yagi, T. Hatsuda, and Y. Miake, Quark Gluon Plasma: From Big Bang to Little Bang (Cambridge, UK, 2005).

[6] P. K. Kovtun, D. T. Son, and A. O. Starinets, Phys. Rev. Lett. **94** 111601 (2005).

[7] A. Ono, H. Horiuchi, T. Maruyama, and A. Ohnishi, Phys. Rev. Lett. **68**, 2898 (1992).

[8] Y. Kanada- En'yo, M. Kimura and A. Ono Prog. Theor. Exp. Phys. (2012), 01A202.

[9] J. Weiner, V. S. Bagnato, S. Zilio and P. S. Julienne, Rev. Mod. Phys. **71**, 1 (1999)

[10] S. Osnaghi, P. Bertet, A. Auffeves, P. Maioli, M. Brune, J. M. Raimond, and S. Haroche, Phys. Rev. Lett. **87**, 037902 (2001).

[11] M. Kalweit and D. Drikakis, Phys. Rev. B **74**, 235415 (2006).

[12] N. V. Brilliantov, N. Albers, F. Spahn, and T. Pöschel, Phys. Rev. E **76**, 051302 (2007).

[13] S. Kim, Phys. Rev. E **83**, 041302 (2011).

[14] H. Kuninaka and H. Hayakawa, Phys. Rev. E **86**, 051302 (2012).

[15] L.B. Han, Q. An, S.N. Luo, and W.A. Goddard, Mater. Lett. **64**, 2230 (2010).

[16] H. Kuninaka and H. Hayakawa, Phys. Rev. E **79**, 031309 (2009).

[17] L. Xu, W. W. Zhang, and S. R. Nagel, Phys. Rev. Lett. **94** 184505 (2005).

[18] M. M. Driscoll and S. R. Nagel, Phys. Rev. Lett. 107, 154502 (2011).

[19] F. Savart, Ann. De Chim. **53**, 337-386 (1833).

[20] F. Savart, Ann. De Chim. **54**, 56-87 (1833).

[21] F. Savart, Ann. De Chim. **54**, 113-145 (1833).

[22] F. Savart, Ann. De Chim. **55**, 257-310 (1833).

[23] N. Dombrowski and P. C. Hooper, J. Fluid Mech. **18** 392-400 (1964).

[24] M. F. Heidmann, R. J. Priem and J. C. Humphrey, NACA TN **3835**. 10:752-54 (1957).

[25] C. Clanet, Phys. Rev. Lett. **85**, 5106 (2000).

[26] C. Clanet, J. Fluid Mech. **430**, 111 (2001).

[27] C. Clanet, Ann. Rev. Fluid Mech. **39**, 469 (2007).

[28] F. H. Bark, Hans-Peter Wallin, M. G. Gällstedt and L. P. Kristiansson, J. Fluid Mech. **90** 625-639 (1979).

[29] G. J. Jameson, C. E. Jenkins, E. C. Button, and J. E. Sader, J. Fluid Mech. **649**, 19 (2010).

[30] E. C. Button, J. F. Davidson, G. J. Jameson and J. E. Sader, J. Fluid Mech. **649**, 45 (2010).

[31] X. Cheng, G. Varas, D. Citron, H. M. Jaeger, and S. R. Nagel, Phys. Rev. Lett. **99** 188001 (2007).

[32] E. C. Rericha, C. Bizon, M. D. Shattuck, H. L. Swinney, Phys. Rev. Lett. **88** 014302 (2001).

[33] C. R. Wassgren, J. A. Cordova, R. Zenit, A. Karion, Physics of Fluids **15**, 3318 (2003).

[34] J. F. Boudet, J. Cassagne, and H. Kellay, Phys. Rev. Lett. **103**, 224501 (2009).

[35] J. S. Uehara, M. A. Ambroso, R. P. Ojha, and D. J. Durian, Phys. Rev. Lett. **90**, 194301 (2003).

[36] H. Katsuragi, Phys. Rev. Lett. **104**, 218001 (2010).

[37] D. Lohse, R. Rauhé, R. Bergmann, and D. van der Meer, Nature (London) **432**, 689 (2004).

[38] J. Ellowitz, N. Guttenberg and W. W. Zhang, arXiv:1201.5562 (2012).

[39] N. Guttenberg, Phys. Rev. E **85**, 051303 (2012).

[40] Y. J. Huang, C. K. Chan, and P. Zamankhan, Phys. Rev. E **82**, 031307 (2010).

[41] H. Sirringhaus, *et al.*, Science **290**, 5499, 2123-2126, (2000).

[42] G. X. Chen, T. J. Kwee, K. P. Tan, Y. S. Choo and M. H. Hong, Appl. Phys. A **101**, 249 (2010).

[43] E. Azanza, F. Chevoir and P. Moucheront, J. Fluid Mech, **400**, 199 (1999).

[44] N. Guttenberg, Phys. Rev. E **83** 051306 (2011).

[45] P. A. Cundall and O. D. L. Strack, Geotechnique, **29**, 47 (1979).

[46] S. Yuu, T. Abe, T. Saitoh and T. Umekage, Adv. Powder. Technol. **6** 259 (1995).

[47] T. G. Sano and H. Hayakawa, Phys Rev. E. **86**, 041308 (2012).

[48] T. G. Sano and H. Hayakawa, arXiv:1211.3533 (2012).

[49] T. G. Sano and H. Hayakawa, in preparation.

[50] J. T. Jenkins and S. B. Savege, J. Fluid. Mech. **130** 187 (1983).

[51] J. T. Jenkins and M. W. Richman, Phys. Fluids. **28**, 3485 (1985).

[52] V. Garzó and J. W. Dufty Phys. Rev. E **59** 5895 (1999).

[53] J. F. Lutsko, Phys. Rev. E **72** 021306 (2005).

[54] K. Kanatani, Trans. Jpn. Soc. Mech. Eng. B **45**, 507 (1979);ibid.**45**, 515 (1979); J. Kano, A. Shimosaka, and J. Hidaka, J. Soc. Powder Techol. Jpn. **33**, 95 (1996).

[55] N. Mitarai, H. Hayakawa and H. Nakanishi, Phys. Rev. Lett. **88**, 174301 (2002).

[56] A. Goldstein and M. Shapiro, J. Fluid Mech. **282**, 75 (1995).

[57] I. Goldhirsch, S. H. Noskowicz, and O. Bar-Lev, Phys. Rev. Lett. **95**, 068002 (2005).

[58] B. Gayen and M. Alam, J. Fluid Mech. **567**, 195 (2006).

[59] N. V. Brilliantov, T. Pöschel, W. T. Kranz, and A. Zippelius, Phys. Rev. Lett. **98**, 128001 (2007).

[60] W. T. Kranz, N. V. Brilliantov, T. Pöeschell and A. Zippelius, Eur. Phys. J. Special Topics, **179**, 91 (2009).

[61] B. Gayen and M. Alam, Phys. Rev. Lett. **100**, 068002 (2008).

[62] B. Gayen and M. Alam, Phys. Rev. E **84**, 021304 (2011).

[63] J. T. Jenkins and C. Zhang, Phys. Fluids **14** 1228 (2002).

[64] D. K. Yoon and J. T. Jenkins, Phys. Fluids **17** 083301 (2005).

[65] H. Xu, M. Y. Louge, and A. P. Reeves, Continuum Mech. Thermodyn. **15**, 321 (2003).

[66] C. K. K. Lun and A. A. Bent, J. Fluid Mech. **258**, 335 (1994).

[67] K. Saitoh and H. Hayakawa, Phys. Rev. E **75** 021302 (2007).

[68] Kuniyasu Saitoh, *Master Thesis, Kyoto University* (*Written in Japanese*).

[69] V. Garzó, J. W. Dufty and C. M. Hrenya, Phys. Rev. E **76**, 031303 (2007).

[70] V. Garzó, J. W. Dufty and C. M. Hrenya, Phys. Rev. E **76**, 031304 (2007).

[71] V. Garzó, J. W. Dufty and C. M. Hrenya, Powder Tech. **220** 24 (2012).

[72] N. Sela and I. Goldhirsh, J. Fluid. Mech. **361** 41 (1998).

[73] N. V. Brilliantov and T. Pöschel, "Kinetic Theory of Granular Gases," Oxford Graduate Texts, 2004.

[74] T. P. C. van Noije and M. H. Ernst, Granular Matter **1**, 57 (1998).

[75] J. Javier Brey, M. J. Ruiz-Montero, and D. Cubero, Phys. Rev. E **54**, 3664 (1996).

[76] Y. Du, H. Li and L. P. Kadanoff, Phys. Rev. Lett. **74**, 1268 (1995).

[77] S. Chapman and T. G. Cowling, "The Mathematical Theory of Non-uniform Gases (Third Edition)," Cambridge University Press, 1970.

[78] J. A. MacLennan, "An Introduction to Nonequilibrium Statistical Mechanics," Prentice Hall, 1989.

[79] R. Balescu, "Equilibrium and Nonequilibrium Statistical Mechanics," John Wiley & Sons, 1975.

[80] P. Rèsibois and M. de Leener, "Classical Kinetic Theory of Fluids," John Wiley & Sons, 1977.

[81] L. E. Reichel, "A Modern Course in Statistical Physics," University Texas Press, 1980.

[82] E. M. Lifshitz and L. P. Pitaevski, "Physical Kinetics," Butterworth-Heinemann, 1981.

[83] J.-P. Hansen and I. R. McDonald, "Theory of Simple Liquids, " *the third edition*, 2006.

[84] S. G. Brush, Kinetic Theory, Vol. 3 (Pergamon Press, New York, 1972).

[85] I. P. Shkarofsky, T. W. Johnston, and M. P. Bachynski, "The Particle Kinetics of Plasmas (Addison-Wesley, Reading, MA)," 1966.

[86] C. Busch and U. Kortshagen, Phys. Rev. E **51**, 280 (1995).

[87] G. A. Bird, Phys. Fluids, **6**, 1518 (1963).

[88] G. A. Bird, J. Fluid Mech. **30**, 479 (1967).

[89] W. Wagner, J. Stat. Phys., **66** 1011 (1976).

[90] Y. Sone and K. Aoki, "Molecular Aerodynamics," (Asakura Publishing, Co., Ltd.), 1994.

[91] S. Chapman, Proc. R. Soc. Lond. A 93:1 (1916-1917); D. Enskog, Thesis, Uppsala (1917) [Both reprinted in [84]].

[92] D. Enskog, K. Sven Vetenskaps Akad. Handl., 63 (no. 4) (1922) English translation appears in: [84].

[93] S.T. Choh and G.E. Uhlenbeck, The kinetic theory of phenomena in dense gases, Ph.D. dissertation, University of Michigan, 1958.

[94] J. A. McLennan, Phys. Lett. **7**, 332 (1963).

[95] K. Kawasaki and I. Oppenheim, Phys. Rev. A **139**, 1763 (1965).

[96] van Beijeren and the M. H. Ernst, Physica **68** 437 (1973).

[97] van Beijeren and the M. H. Ernst, Physica **70** 225 (1973).

[98] van Beijeren and the M. H. Ernst, Phys. Rev. **43 A**, 167 (1973).

[99] J.M. Kincaid, Phys. Lett. A, **64**, 429 (1978).

[100] van Beijeren and the M. H. Ernst, J. Stat. Phys. **21** 2, (1979).

[101] M. López de Haro and V. Garzó, Physica A **197** 98, (1993).

[102] M. H. Ernst, arXiv:cond-mat/9707146 (1997).

[103] S. Torquato, Phys. Rev. E **51**, 3170 (1995).

[104] V. Kumaran, Phys. Rev. Lett. **96**, 258002 (2006).

[105] A. V. Orpe, and A. Kudrolli, Phys. Rev. Lett. **98**, 238001 (2007).

[106] M. Otsuki, H. Hayakawa, Eur. Phys. J. Special Topics 179 179-195 (2009).

[107] M. Otsuki, and H. Hayakawa, Phys. Rev. E **79**, 021502 (2009).

[108] H. Hayawawa, Song-Ho. Chong and M. Otsuki, IUTAM-ISIMM Symposium on Mathematical Modeling and Physical Instances of Granular Flow, pp.19-30 edited by J. D. Goddard, J. T. Jenkins and P. Govine (AIP vol.1227, New York, 2010).

[109] K. Suzuki and H. Hayakawa, arXiv:1301.0866.

[110] R. A. Bagnold, Proc. Roy. Soc. London A, **225**, 49, (1954).

[111] O. Pouliquen, Phys. Fluids, **11**, 542, (1999).

[112] L. E. Silbert, D. Ertas, G. S. Grest, T. C. Halsey, D. Levine and S. J. Plimton, Phys. Rev. E, **64**, 053102, (2001).

[113] N. Mitarai and H. Nakanishi, Phys. Rev. Lett. **94**, 128001 (2005).

[114] G. Lois, A. Lemâitre, and J. M. Carlson, Phys. Rev. E **72**, 051303 (2005).

[115] R. Delannay, M. Louge, P. Richard, N. Taberlet and A. Valance, Nature Materials **6**, 99 (2007).

[116] V. Kumaran, J. Fluid Mech, **599**, 121 (2008).

[117] C-H. Lee and C-J. Huang, Phys. Fluids **24**, 073303 (2012).

[118] K. M. Hill and B. Yohannes, Phys. Rev. Lett. **106**, 058302 (2011).

[119] S. B. Savage, J. Fluid Mech. **241**, 109 (1992).

[120] M. Alam and P. R. Nott, J. Fluid Mech. **377**, 99 (1998).

[121] P. R. Nott, M. Alam, K. Agrawal, R. Jackson and S. Sundaresan, J. Fluid Mech, **397** 203 (1999).

[122] V. Garzó, Phys. Rev. E **73**, 021304 (2006).

[123] A. W. Lees and S. F. Edwards, J. Phys. C: Solid State Phys. **5** (1972).

[124] K. Saitoh and H. Hayakawa, Granular Matter **13**, 697 (2011).

[125] K. Saitoh and H. Hayakawa, AIP. Conf. Proc. **1501**, 1001 (2012).

[126] GDR MiDi, Eur. Phys. J. E **14**, 341 (2004).

[127] O. Pouliquen, Phys. Fluids **11** 542 (1999).

[128] P. Jop, Y. Forterre, and O. Pouliquen, Nature (London) **441**, 727 (2006).

[129] Y. Forterre and O. Pouliquen, Annu. Rev. Fluid. Mech **40**, 1-24 (2008).

[130] B. Yohannes and K. M. Hill, Phys. Rev. E **82**, 061301 (2010).

[131] F. da Cruz *et al*, Phys. Rev. E **72**, 021309 (2005).

[132] N. Xu, and C. S. O'Hern, Phys. Rev. E **73**, 061303 (2006).

[133] T. Hatano, Phys. Rev. E **75**, 060301(R) (2007).

[134] T. Hatano, M. Otsuki, and S.-I. Sasa, J. Phys. Soc. Jpn. **76**, 023001 (2007).

[135] H. Kawamura, T. Hatano, N. Kato, S. Biswas, and B. K. Chakrabarti, Rev. Mod. Phys. **84**, 839 (2012).

[136] A. J. Liu and S. R. Nagel, Nature **396**, 21 (1998).

[137] M. Otsuki and H. Hayakawa, Phys. Rev. E **83**, 051301 (2011).

[138] P. Olsson and S. Teitel, Phys. Rev. Lett. **99** 178001 (2007).

[139] P. Olsson and S. Teitel, Phys. Rev. E **83**, 030302 (2011).

[140] B. P. Tighe, E. Woldhuis, J. J. C. Remmers, W. van Saarloos and M. van Hecke, Phys. Rev. Lett. **105** 088303 (2010).

[141] K. Nordstrom, E. Verneuil, P. Arratia, A. Basu, Z. Zhang, A. Yodh, J. Gollub and D. Durian, Phys. Rev. Lett. **105** 175701 (2010).

[142] M. Otsuki, H. Hayakawa, and S. Luding, Prog. Theor. Phys. Suppl. **184**, 110 (2010).

[143] T. Hatano, Prog. Theor. Phys. Suppl. **184**, 143 (2010).

[144] M. Otsuki, and H. Hayakawa, Phys. Rev. E **80**, 011308 (2009).

[145] M. Otsuki, and H. Hayakawa, Prog. Theor. Phys. **121**, 647 (2009).

[146] T. Hatano, J. Phys. Soc. Jpn. **77** 123002 (2008).

[147] R. Garcia-Rojo, S. Luding and J. J. Brey, Phys. Rev. E **74**, 061305 (2006).

[148] W. Losert, L. Bocquet, T. C. Lubensky and J. P. Gollub, Phys. Rev. Lett. **85** 1428 (2000).

[149] M. Otsuki and H. Hayakawa, Prog. Theor. Phys. Suppl. **195**, 129 (2012).

[150] B. J. Alder, and T. E. Wainwright, Phys. Rev. **127**, 359(1962).

[151] N. D. Mermin, Phys. Rev. **176** 250 (1968).

[152] B. I. Halperin and D. R.Nelson, Phys. Rev. Lett. **41**, 121 (1978).

[153] B. I. Halperin, and David R. Nelson, Phys. Rev. B, **19**, 2457 (1979).

[154] A. P. Young, Phys. Rev. B **19**, 1855 (1979).

[155] S. T. Chui, Phys. Rev. Lett. 48, 933 (1982).

[156] K. J. Strandburg, Rev. Mod. Phys. 60, 161 (1988).

[157] K. N. Nordstrom, E. Verneuil, P. E. Arratia, A. Basu, and Z. Zhang, Phys. Rev. Lett. **105** 175701 (2010).

[158] R. Lespiat, S. Cohen-Addad, and R. Höhler, Phys. Rev. Lett. **106** 148302 (2011).

[159] H. Mori, Prog. Theor. Phys. **33**, 423 (1965).

[160] R. Zwanzig, "Non-equilibrium statistical mechanics", Oxford, 2001.

[161] A. Kawarada and H. Hayakawa, J. Phys. Soc. Jpn. **73**, (2004).

[162] O. R. Walton and R. L. Braun, J. Rheol. **30**, 949 (1986).

[163] M. Otsuki and H. Hayakawa, Phys. Rev. E. **83**, 051301(2011).

[164] D. Goldman, M. D. Shattuck, C. Bizon, W. D. McCormick, J. B. Swift, and H. L. Swinney, Phys. Rev. E. **57**, 4831 (1998).

[165] L. Labous, A. D. Rosato and R. N. Dave, Phys. Rev. E. **56**, 5717 (1997).

[166] T. Sano and H. Hayakawa, *in Procedings of ICTAM 23rd Int. Congress of theoretical and applied mechanics.*

[167] R. Goetz and R. Lipowsky, J. Chem. Phys. **108**, 7397 (1998).

[168] http://apollon.issp.u-tokyo.ac.jp/ watanabe/pdf/pnote.pdf "The microscopic definition of the pressure for particle-systems " (*Written in Japanese*).

[169] W. H. Press, S. A. Teukolsky, W. T. Vetterling, and B. P. Flannery, Numerical Recipes, 3rd ed. (Cambridge University Press, Cambridge, UK, 2007).